University of Massachusetts Amherst
ScholarWorks@UMass Amherst

Doctoral Dissertations | Dissertations and Theses

March 2020

Engineered Nanoparticles for Site-Specific Bioorthogonal Catalysis: Imaging and Therapy

Riddha Das

Follow this and additional works at: https://scholarworks.umass.edu/dissertations_2

 Part of the Animal Sciences Commons, Bacteriology Commons, Biology and Biomimetic Materials Commons, Catalysis and Reaction Engineering Commons, Nanomedicine Commons, Nanoscience and Nanotechnology Commons, Organic Chemicals Commons, Other Materials Science and Engineering Commons, and the Other Microbiology Commons

Recommended Citation

Das, Riddha, "Engineered Nanoparticles for Site-Specific Bioorthogonal Catalysis: Imaging and Therapy" (2020). *Doctoral Dissertations*. 1819.
https://doi.org/10.7275/151n-xc54 https://scholarworks.umass.edu/dissertations_2/1819

This Open Access Dissertation is brought to you for free and open access by the Dissertations and Theses at ScholarWorks@UMass Amherst. It has been accepted for inclusion in Doctoral Dissertations by an authorized administrator of ScholarWorks@UMass Amherst. For more information, please contact scholarworks@library.umass.edu.

ENGINEERED NANOPARTICLES FOR SITE-SPECIFIC BIOORTHOGONAL CATALYSIS: IMAGING AND THERAPY

A Dissertation Presented

By

RIDDHA DAS

Submitted to the Graduate School of the
University of Massachusetts Amherst in partial fulfillment
of the requirements for the degree of

DOCTOR OF PHILOSOPHY

February 2020

Chemistry

@ Copyright by Riddha Das 2020

All Rights Reserved

ENGINEERED NANOPARTICLES FOR SITE-SPECIFIC BIOORTHOGONAL CATALYSIS: IMAGING AND THERAPY

A Dissertation Presented

By

RIDDHA DAS

Approved as to style and content by:

Vincent M. Rotello, Chair

Michael J. Maroney, Member

Dhandapani Venkataraman, Member

Lisa M. Minter, Member

Ricardo B. Metz, Department Head

Department of Chemistry

To my brother Siddhartha (Sid) Das

ACKNOWLEDGMENTS

I would like to begin by thanking my advisor Vincent Rotello for his patience and constant encouragement during my graduate studies. He helped me focus on the big picture and gave me the opportunity to develop a broader scientific viewpoint by allowing me to work on many interesting research projects. Coming from an entirely different background, this dissertation work would not be possible without his guidance and enthusiasm to do exciting science.

I would like to thank my dissertation committee Dhandapani Venkataraman, Michael Maroney and Lisa Minter for their valuable comments on my research. I enjoyed the insightful conversations with each of them on multiple occasions.

I would like to thank past and present Rotello lab members whose contribution made this dissertation possible. I thank Youngdo for teaching me the techniques to fabricate the bioorthogonal toolkit 'nanozymes', which I happened to use in all of my projects. I am thankful to Bo for teaching me mass spectrometry techniques, he was extremely patient in taking out the time to help me during his busy graduation time. I acknowledge Gulen for being an excellent mentor during my initial years in Rotello lab, her suggestions were immensely helpful to me in both: organic synthesis and cell-culture. I appreciate Ryan for his enthusiasm in synthesizing substrates used in Chapter 2 of this dissertation. I am grateful to Akash for helping me explore the application of nanozymes in the field of bacteria and biofilms, demonstrated in chapters 4 and 5. His technical critique and detailed experimental planning made a significant impact to my scientific approach. I would also like to acknowledge the contributions of Joe, Xianzhi, Rui, Lucy, Saya, Olivia and Madi in this dissertation.

I acknowledge the help from our collaborator Michelle Farkas, her expertise in macrophages helped us perform the work presented in chapter 3. I am thankful to Bishnu from the Farkas lab for performing macrophage migration studies.

During PhD in a new place away from my family, staying focused is always difficult without great friends. I would specially like to mention Akash, who made my days during PhD quite memorable. I am thankful to him for being an excellent lab mate and a great friend outside the lab.

I would like to thank my mother and father for their moral support and remaining optimistic during my graduate studies. Finally, I would like to express my gratitude for my brother. He inspired me to dream and taught me to diligently work towards that dream. I am grateful for his constant encouragement to nurture my scientific curiosity, since the time we both were kids. This work is dedicated to him.

ABSTRACT

ENGINEERED NANOPARTICLES FOR SITE-SPECIFIC BIOORTHOGONAL CATALYSIS: IMAGING AND THERAPY

FEBRUARY 2020

RIDDHA DAS, B.TECH., UNIVERSITY OF CALCUTTA

M.TECH., IIT KHARAGPUR

Ph.D., UNIVERSITY OF MASSACHUSETTS AMHERST

Directed by: Professor Vincent M. Rotello

Bioorthogonal catalysis offers a strategy for chemical transformations complementary to bioprocesses and has proven to be a powerful tool in biochemistry and medical sciences. Transition metal catalysts (TMCs) have emerged as a powerful tool to execute selective chemical transformations, however, lack of biocompatibility and stability limits their use in biological applications. Incorporation of TMCs into nanoparticle monolayers provides a versatile strategy for the generation of bioorthogonal nanocatalysts known as "nanozymes". We have fabricated a family of nanozymes using gold nanoparticles (AuNPs) as scaffolds featuring diverse chemical functional groups for controlled localization of nanozymes in biological environments, providing unique strategies for bioorthogonal imaging and therapeutic applications.

My research is focused on modulating nanozyme surface chemistry for controlled localization of nanozymes at the site of interest for controlled bioorthogonal catalysis in mammalian and bacterial cells. In the intial studies, I have demonstrated controlled localization of nanozymes inside and outside the mammalian cell membrane. Nanozymes bearing cationic charge were used for activation of substrates inside the cells, owing to their high cellular internalization, whereas relatively impermeable zwitterionic nanozymes were used for extracellular activation of substrate molecules. Next, these cell-penetrating nanozymes were loaded inside the macrophages to develop a toolkit for targeting tumor site. With the inherent ability of macrophages to home in on tumor site, I demonstrated that nanozymes can generate chemotherapeutic drugs to selectively

kill the cancer cells. This strategy has potential to reduce the off-target toxicity of the chemotherapy drugs.

In subsequent studies, I utilized engineered bioorthogonal nanozymes to target bacterial biofilm infections. Functionalization of nanozyme surface with pH-responsive ligands enabled us to selectively image bacterial biofilms by targeting the acidic microenvironment of biofilms. In another strategy, nanozymes were non-covalently adsorbed on the surface of Red Blood Cells (RBCs) for selective killing of pathogenic bacteria. RBCs being highly susceptible to bacterial exotoxins were hemolyzed, resulting in selective accumulation of nanozymes at site of infection. These nanozymes in-turn activated pro-antibiotics at the site of bacterial infection to eradicate biofilms. Overall, these studies show strong potential of engineered nanozymes toolkit to generate imaging and therapeutic agents at targeted sites utilizing bioorthogonal chemistry.

TABLE OF CONTENTS

Page

LIST OF TABLES

LIST OF FIGURES

Figure Page

CHAPTER 1

INTRODUCTION

1.1 Bioorthogonal chemistry

Bioorthogonal chemistry introduced the idea of carrying out selective chemical reactions with high efficiency in a complex biological environment with minimal interference to native biochemical processes.[1-6] Chemical functional groups present in biological systems can act as reducing agents, nucleophiles, electrophiles and oxidants, however, bioorthogonal reactions are capable to proceed efficiently in presence of all these functional groups without interfering the native bioprocesses (Figure 1.1). The term "bioorthogonal chemistry" was first coined by Carolyn R. Bertozzi in 2003 to demonstrate Staudinger ligation reaction between an azide- containing unnatural sugar and a modified triphenylphosphine-fluorophore conjugate.[7] Since then, synthetic chemists have explored new strategies to perform traditional organic reactions in accordance with biological systems. The reactions that were conventionally performed in a round bottom flask and test tubes in organic solvents, can now be performed in *in vitro* and *in vivo* biological environments.

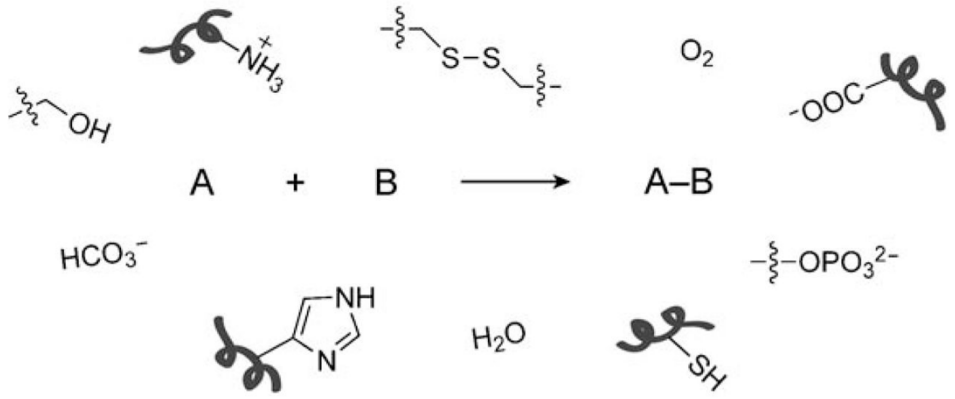

Figure 1.1. Scheme of a bioorthogonal chemical reaction, where the reaction between compounds A and B proceeds in presence of numerous functional groups present in a living system. Adapted with permission from reference 3.

Amongst multiple bioorthogonal chemical reactions, ligation reaction between two inert, stable and biocompatible components has been explored on numerous instances. Copper catalyzed

"click chemistry" for azide-alkyne cycloaddition (CuAAC) exhibits fast kinetics and excellent bioorthogonality.[8-12] However, high cytotoxicity of copper has resulted in scientists searching for alternative biocompatible ligation reactions. One approach utilizes biocompatible copper-free strain-driven azide-alkyne cycloaddition (SPAAC) between an azide and a strained alkyne (Figure 1.2).[12-15] In another approach, scientists have designed a series of ligands that can stabilize and decrease the toxicity of Cu(I).[16] Alternatively, other transition metals such as palladium (Pd) and ruthenium (Ru) have been explored for catalyzing cross-coupling and olefin-metathesis reactions respectively.[5]

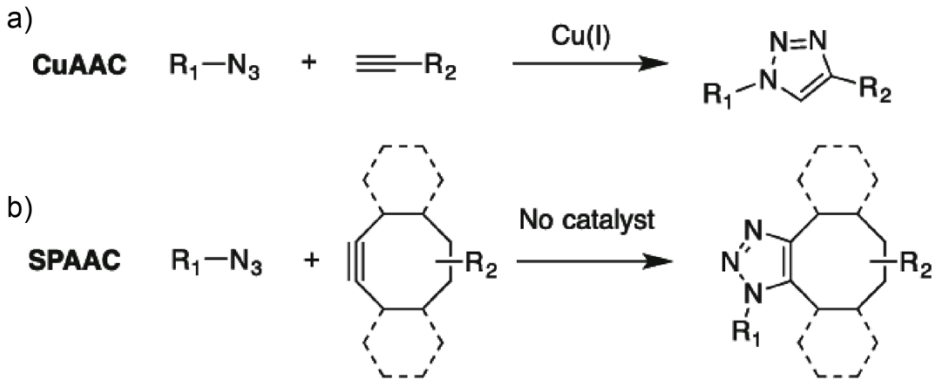

Figure 1.2. a) The copper-catalyzed azide-alkyne cycloaddition (CuAAC). b) The Cu free click reaction of azides and alkyne (SPAAC). Adapted with permission from reference 12.

Besides ligation reactions, bond-cleavage chemical reactions have been extensively used for providing bioorthogonal reactivity to the biological entities. In these chemical reactions, functional groups on substrates undergo bond cleavage to generate final product through bioorthogonal reactions (Figure 1.3). For example, o-nitrobenzyl (ONB) ether derivatives undergo UV-induced photo-decaging.[17] Although, photo-cleavage reactions have demonstrated multiple applications, these strategies have a few major drawbacks such as photo-toxicity, low tissue penetration and need of specialized equipment.[18] Additionally, the widely used ONB group may be decaged by nitroreductase present in hypoxic mammalian cells and bacterial cells, hence compromising the bioorthogonality.[19,20] Due to potential drawbacks of photo-uncaging techniques,

alternative strategies using small molecules and transition metal catalysts have been developed. The latter strategy (described in following section 1.2) is specifically more advantageous for carrying out bioorthogonal cleavage reactions in a precisely tunable, sustainable and minimally invasive manner.

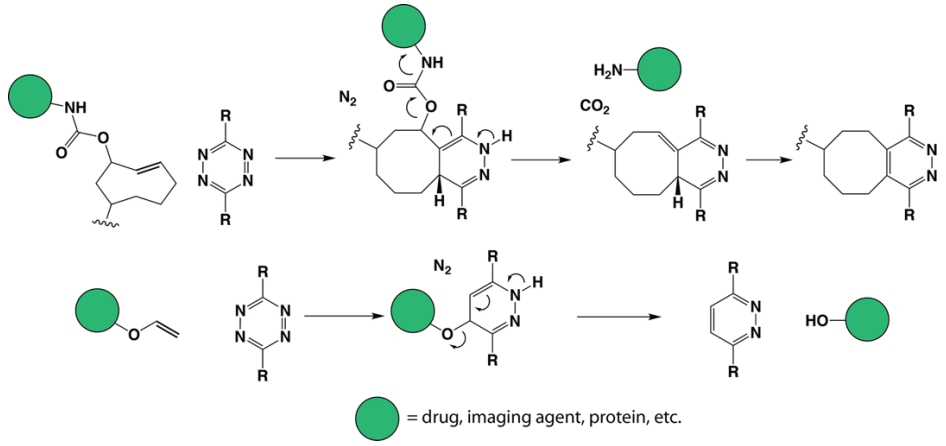

Figure 1.3. Representatives of bioorthogonal cleavage reactions. Typically, a masked drug, imaging agent or an enzyme is deprotected by UV light, small molecules or transition metal catalysts to their active state by bioorthogonal cleavage reactions. Adapted with permission from reference 4.

1.2 Transition metal mediated bioorthogonal catalysis

Transition metal catalysts (TMCs) have potential to overcome the drawbacks of photo-uncaging and other similar bioorthogonal reactions. TMCs possess unique electro-chemical properties, enabling them to remove multiple protecting groups in a complex biological medium using a specific mechanism for each reaction. TMC-mediated reactivity provides the ability to chemically control the bond cleavage in a living environment without being dependent on location of the tissue and source intensity (Figure 1.4). These characteristics make TMCs an excellent candidate for bioorthogonal catalysis,[21-24] however, stability of TMCs is reduced in complex biological settings restricting their widespread applications.

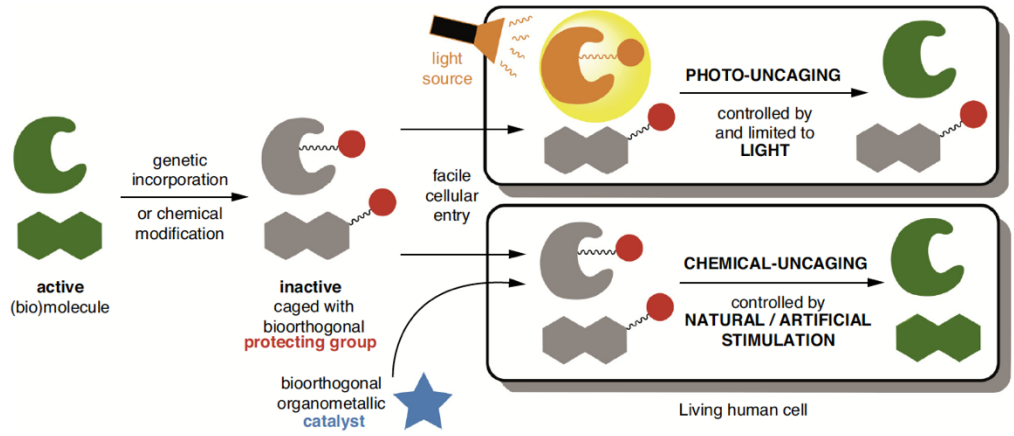

Figure 1.4. Schematic diagram showing the comparison between a photo-uncaging and an organometallic catalyst mediated cleavage reaction. Organometallic catalysts can perform uncaging triggered by natural or light independent external stimulations, while, photo-uncaging relies on the light source and the operator. Adapted with permission from reference 21.

Researchers have developed multiple strategies for using TMCs in mammalian, bacterial cells and even more complex organisms such as zebra fish and mice. The pioneering study utilizing TMCs for uncaging reactions in living mammalian cells was performed by Streu and Meggers in 2006. [25] They demonstrated that Ru based TMC [Cp*Ru(cod)Cl] (Ru1; Cp* = h5-pentamethylcyclopentadienyl, cod = h4-1,5-cyclooctadiene) activated fluorescent molecules inside a living mammalian cells under biologically relevant conditions (Figure 1.5). They chose N,N-bis-allyloxycarbonyl protected rhodamine 110 as the cellular probe. HeLa cells were incubated with substrates for 0.5 h, followed by washing with phosphate buffered saline (PBS). Upon addition of Ru-catalyst and thiophenol, rapid increase in fluorescence was observed due to cleavage of the allylcarbamate protecting group. Since then, numerous other Ru based catalysts were screened for faster kinetics and improved biocompatibility.[26,27] In another work, Meggers and co-workers investigated aromatic azide as a masking group and pioneered uncaging azide protected amines in mammalian cells by using a combination of [Fe(TPP)Cl] (Fe1; TPP = 5,10,15,20-tetraphenyl-21H,23H-porphin) and a thiol.[28] HeLa cells incubated with azide-rhodamine and Fe(TPP)Cl catalyst exhibited 28-fold fluorescence increase in the cytoplasm after 10 minutes. They further demonstrated *in vivo* application of the TMC-mediated catalysis in zebra fish and nematode models.

Although free TMCs successfully activated substrates in the short duration of these experiments, it became important to develop alternative strategies for minimizing the toxicity caused by these TMCs for long-term biological applications. Recently, there has been considerable progress in developing heterogeneous catalyst systems for bioorthogonal uncaging reactions in living environment.

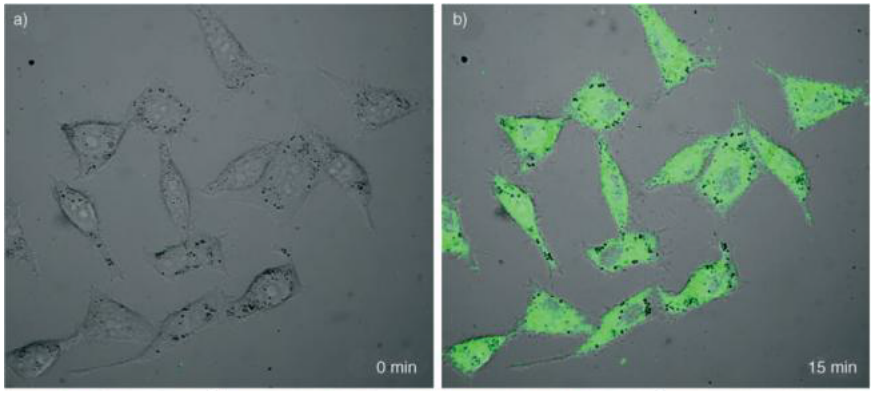

Figure 1.5. Fluorescence microscopy images of uncaging process of allylcarbamate-protected rhodamine 110 (pro-fluorophore) inside HeLa cells using ruthenium nanocatalyst. a) Right after catalyst addition and b) after 15 min. Adapted with permission from reference 25.

Unciti Broceta and Bradley et al. developed a biocompatible cell-internalizable Pd^0 based heterogeneous catalyst system to minimize the toxicity caused by free metal ions.[29] They combined two techniques: an amino functionalized polystyrene microsphere as a delivery vehicle and entrapment of Pd nanoparticles (PdNP1) within cross-linked resin beads. These PdNPs were upaken by the cells, then these NPs activated alloc-rhodamine substrate and performed Suzuki-Miyaura cross-coupling reaction within the cytoplasm (Figure 1.6). This was the first example utilizing a bioorthogonal heterogeneous palladium catalyst to perform non-natural chemistry in the cytoplasm of human cells. Subsequently, Unciti Broceta and Bradley *et al.* developed palladium macroscpheres (PdNP2), for extracellular activation of propargyl protected 5-Fluorouracil (5-FU).[30] In further studies, they used palladium-mediated bioorthogonal chemistry to activate other cytotoxic drugs such as gemcitabine and floxuridine.[31-34] These studies highlight the enormous potential of TMCs to execute bioorthogonal reaction for multiple biomedical applications.

Moreover, synthetic carriers play a critical role in enhancing the catalyst stability and controlling their selectivity for increased efficacy of the bioorthogonal strategies.

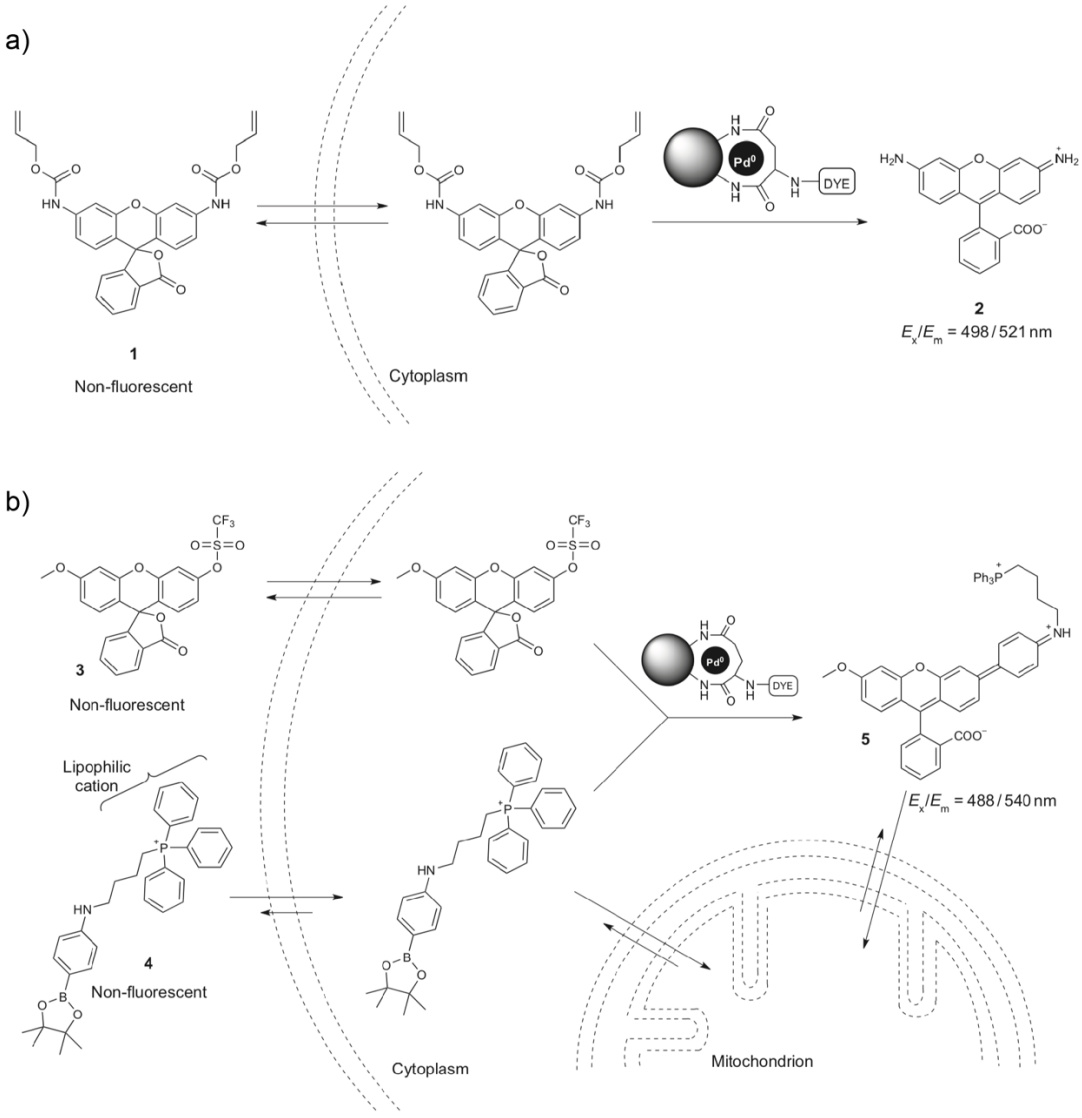

Figure 1.6. Pd^0-mediated allylcarbamate cleavage within HeLa cells. a) Pd^0-catalysed intracellular deprotection of reagent 1 generates fluorescent compound 2 b) Pd^0-mediated Suzuki–Miyaura cross-coupling within HeLa cells: cross-coupling of reagents 3 and 4 generates the mitochondria-localized fluorescent compound 5. Adapted with permission from reference 29.

1.3 Fabrication of gold nanoparticles

Delivery of therapeutic molecules to specific physiological targets is a key challenge. In the past few decades, multiple nanocarriers have been developed for different biological

applications including metal nanoparticles, dendrimers and polymeric micelles.[35-43] Among all these nanocarriers, gold nanoparticles (AuNPs) are particularly promising owing to a number of desirable characteristics.[44-49] Firstly, gold core is relatively non-toxic and inert. Secondly, AuNPs can be easily functionalized with surface structures for modulating interaction with biological entities. Finally, AuNPs can be easily tracked and quantified by mass spectrometry. A popular approach to synthesize the Au core is reducing gold salt ($HAuCl_4$) by Commonly, thiol-protected AuNP core is synthesized following biphasic strategy pioneered by Brust-Schiffrin.[50] In this method, Au salt ($HAuCl_4$) is transferred to organic phase by a surfactant tetraoctylammonium bromide (TOAB) followed by reduction of Au salt by sodium borohydride ($NaBH_4$) in presence of alkanethiols. Next, AuNPs are coated with monolayer of appropriate ligands following Murray place exchange reaction taking advantage of strong gold-thiol affinity.[51] After ligand functionalization, AuNPs are characterized for size, surface charge and ligand density.

The AuNPs described in this dissertation were developed by several generation in Rotello group.[46,47] Briefly, it has a 2 nm gold core and ligands are attached to the core through a thiol anchor. The ligand monolayer consists of three crucial components (Figure 1.7): a) a long aliphatic chain composed of 11 carbons to provide particle stability[52] b) a spacer of four ethylene glycol units to provide biocompatibility, the length of the spacer was optimized to minimize aggregation in biological fluids[53,54] and c) a functional group to modulate the interaction with biological entities. Using this methodology NPs can be functionalized with distinct headgroups allowing us to ascertain the interactions of these functional groups with biosystems in a quantitative fashion. Specific design of surface structure can dictate enhanced uptake by specific cell type, payload binding capacity and non-interacting stealth properties.

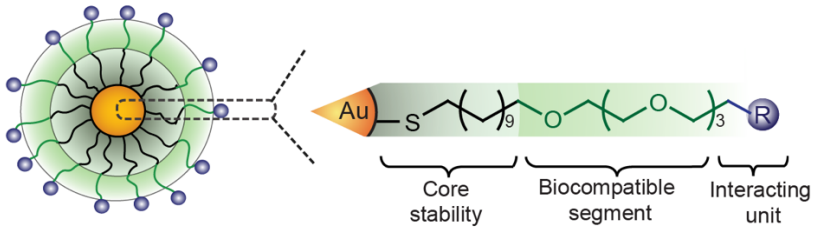

Figure 1.7. Schematic representation of engineered nanoparticles used in this dissertation.

1.4 Engineered gold nanoparticles for drug delivery

Engineered AuNPs represent an excellent candidate for drug delivery due to high surface area and tunability. For example, therapeutic molecules attached to the monolayers can provide controlled and sustained drug release. Therapeutic molecules can be attached to AuNPs either by covalent coupling or non-covalent adsorption. Mirkin *et al.* demonstrated conjugation of paclitaxel (a potent chemotherapeutic drug) to AuNPs via DNA linkers, thereby enhancing the solubility and overall effectiveness of the drug.[55] Similarly, Zubarev *et al.* attached the same drug to phenol-terminated AuNPs through a flexible hexaethylene glycol linker.[56] Mirkin, Lippard and coworkers developed a strategy to covalently conjugate Pt(IV) prodrugs to oligonucleotide AuNPs, exhibiting enzyme mediated intracellular activation of the prodrug into active form of Pt(II), resulting in enhanced cytotoxicity relative to free drugs. [57] Moreover, Intracellular prodrug activation reduced the side effect of drug, attributing to delivery in an inert form.

Alternatively, prodrugs can also be activated/released intracellulary by glutathione (GSH) mediated activation/cleavage, provides a non-enzymatic stimuli-based strategy. Rotello *et al.* demonstrated GSH mediated intracellular release of a hydrophobic dye (Bodipy) from monolayer functionalized AuNPs.[58] They used a cationic AuNP for enhanced cellular uptake and the dye release was observed attributing to fluorescence quenching ability of AuNPs. Alternatively, the drugs can be attached non-covalently to the NPs, providing a strategy for direct release at the targeted site. Rotello *et al.* developed a strategy for non-covalent drug attachment by utilizing the

hydrophobic pocket present in the monolayer structure (Figure 1.8). The radial arrangement of the ligands creates a hydrophobic interior inside the monolayer of the AuNPs that can used to load hydrophobic drugs in the cavity. Whereas, outer surface chemistry can be used to regulate the interactions of the AuNPs with cell membranes. Rotello *et al.* used a zwitterionic functionalized AuNPs for minimizing non-specific binding with biomacromolecules and preventing cellular uptake.[59] The hydrophobic dye/drug molecules were encapsulated in the hydrophobic pocket by using solvent displacement method. The payload was released by membrane-mediated diffusion to MCF-7 cells. The AuNPs were found to be excellently biocompatible causing minimal toxicity to the cells.

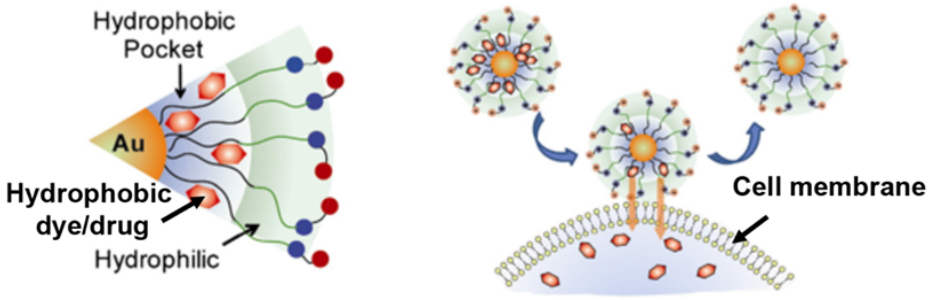

Figure 1.8. Schematic representation of AuNP containing monolayer entrapped drugs and their delivery into cells through monolayer membrane interaction. Adapted with permission from reference 59.

1.5 Engineered nanoparticles for bioorthogonal catalysis: Nanozymes

Building on the previous work encapsulating hydrophobic dye/drug in the surface monolayer, Rotello and co-workers used the same strategy to encapsulate hydrophobic TMCs into the monolayer of water soluble ~ 2 nm core gold nanoparticles (AuNPs) providing the TMCs biocompatibility and stability (Figure 1.9).[60-65] The long aliphatic chain in the AuNPs were used to encapsulate hydrophobic TMCs. This strategy provides a general platform that solubilizes hydrophobic catalyst preserving their activity and stability. These AuNP-catalyst complexes were termed as "nanozymes", due to their nanometric particle dimensions and catalytic activity reminiscent to that of enzymes. The encapsulation was performed by the solvent displacement

method used in the previous study.[59] Briefly, water soluble AuNPs were mixed with organic solution of TMCs. The organic layer was slowly evaporated, and the excess catalyst was removed by multiple filtration cycles including molecular cut-off filter and dialysis. The catalytic activity of the nanozymes were assessed by activation imaging and therapeutic agents in solution and in *in-vitro* models.

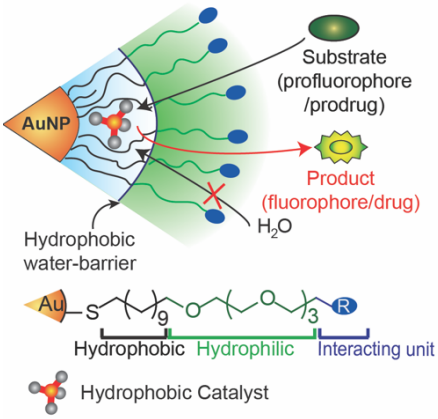

Figure 1.9. Schematic representation of nanozymes used in this dissertation. Adapted with permission from reference 60.

After establishing the nanozyme toolkit, Rotello and coworkers developed a strategy to regulate the catalysis of nanozymes using host-guest supramolecular interactions.[61] The catalytic activity of nanozymes was reversibly controlled by using cucurbit[7]uril as a "gate-keeper", attributing to supramolecular interactions between cucurbit[7]uril and ligand terminal group. This "gate-keeper" turns the nanozymes catalytically inactive until a guest molecule 1-adamantylamine (ADA) is added to displace the cucurbit[7]uril molecules. The efficacy of this supramolecular gated-activation system was demonstrated by the activation of allylcarbamate-caged pro-rhodamine and propargyl-masked 5-FU in HeLa cells. The substrates could be activated only in absence of "gate-keeper" or after the addition of the competing guest ADA when cucurbituril was present (Figure 1.10).

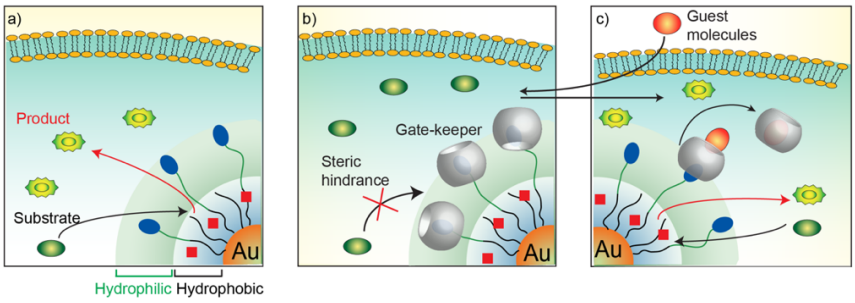

Figure 1.10. Schematic diagram of supramolecular regulation of intracellular catalysis a) substrate activation by bioorthogonal nanozyme in mammalian cell b) a gate-keeper molecule forms a complex with the ligand headgroup and inhibits catalytic activity c) catalysis is restored by addition of a guest molecule which replaced the gate-keeper. Adapted with permission from reference 61.

1.6 Dissertation overview

Site-specific localization of nanozymes is crucial for generating imaging and therapeutic molecules at the desired site for targeted imaging and drug delivery. The surface engineering of nanomaterials dictates their interaction with biological cellular systems and plays a pivotal role in determining the spatiotemporal localization of the nanozymes. In this thesis, I have focused on tuning the surface chemistry of nanozymes for controlling their localization and bioorthogonal catalysis inside-outside of cell membrane, targeting tumor site and bacterial biofilms.

In the Chapter 2 of this thesis, I have demonstrated intra and extracellular localization of nanozymes in mammalian cells. I have utilized a cell membrane penetrating cationic nanozyme for intracellular localization and a stealth zwitterionic nanozyme for extracellular localization. The spatial localization was demonstrated by activating two pro-fluorophores of different wavelengths and polarity inside and outside the cell membrane. We next compared therapeutic efficacy of intra vs extracellular activation of pro-chemotherapeutic drug. By exploiting the ability to regulate nanozyme-cell interaction through appropriate surface functionalization, I designed a highly modular system for in-situ generation of diagnostic and therapeutic agents at both inside and outside the cell membrane. This strategy provides a novel toolkit to regulate important cellular processes using bio-orthogonal chemistry and creates a platform for wide-variety of medical applications.

Building on these studies, In Chapter 3, I further explored the ability of these engineered nanozymes to target tumor sites. Targeting the tumor microenvironment has emerged as a prominent strategy in cancer therapy to overcome the lack of specificity of conventional chemotherapy techniques. Macrophages have demonstrated ability to migrate across chemoattractant gradients and are actively recruited to tumor regions. This characteristic makes macrophages particularly attractive as a delivery vehicle to access solid tumors, which is normally difficult to reach by conventional targeting strategies. This immune cell-based delivery strategy has prolonged circulation time and excellent biocompatibility. I have created a strategy to engineer macrophages with the catalytic ability to activate prodrugs, that can trigger unlimited payload release with controlled kinetics and excellent targeting efficacy. In this study, I engineered macrophages as a delivery vehicle for nanozymes. These nanozymes can activate a prodrug by a bioorthogonal cleavage reaction in the cellular environment. By virtue of selective bioorthogonal chemical activation, I facilitated controlled release of drug molecules selectively at the targeted site reducing the systemic toxicity of the conventional therapy. The efficacy of engineered macrophages was tested in a coculture model with cancer cells. Significant cell toxicity was achieved even at the lowest concentration of the prodrug administered. This strategy combines targeting ability of cell-based drug delivery with bio-orthogonal activation of chemotherapeutic prodrug, providing an approach for next generation drug delivery systems.

In Chapter 4, I engineered nanozymes to target bacterial biofilms. Early detection of biofilms is crucial for limiting infection-based damage. Imaging these biofilms is challenging: conventional imaging agents are unable to penetrate the dense matrix of the biofilm, and many imaging agents are susceptible to false positive/negative responses due to phenotypical mutations of the constituent microbes. I developed a pH-responsive nanozyme, that are selectively uptaken by the acidic microenvironment of biofilm. These nanozymes generate imaging agents through bioorthogonal activation of profluorophores inside biofilms demonstrating potential for early

detection of biofilm-associated infections. The specificity of these nanozymes for imaging biofilms in complex biosystems was demonstrated using co-culture experiments.

In Chapter 5, I have used an alternative strategy to improve the selectivity of the nanozymes to target bacterial biofilms. Controlled localization of bio-orthogonal catalysts at the diseased site is central to the potency of the therapy. Notably, Red Blood Cells (RBCs) have been utilized to transport cargo to the targeted site with high efficacy. Moreover, these RBC carriers are susceptible to hemolysis by bacterial toxins providing them intrinsic targeting ability to bacterial infections. Here, I have developed a versatile strategy by hitch-hiking bioorthogonal nanozymes on RBCs to combat bacterial infections. I used a library of nanoparticles embedded with TMCs (nanozymes) featuring diverse functional groups with different binding ability to RBCs. These nanozymes were electrostatically adsorbed on carrier Red Blood Cells, enabling them to selectively accumulate at the site of bacterial infection while avoiding non-specific uptake in macrophages. The RBC-nanozymes could activate moxifloxacin antibiotics to eradicate pathogenic biofilms without harming non-virulent bacterial species. This study shows that interactions at nano-bio interface can play a crucial role in integration of synthetic materials with naturally occurring systems, resulting in novel antimicrobial therapies.

1.7 References

1. Boyce, M.; Bertozzi, C. R. Bringing Chemistry to Life. *Nat. Methods* **2011**, *8*, 638-642.

2. Bertozzi, C. R. A Decade of Bioorthogonal Chemistry. *Acc. Chem. Res.* **2011,** *44*, 651–653.

3. Sletten, E. M.; Bertozzi, C. R. Bioorthogonal Chemistry: Fishing for Selectivity in a Sea of Functionality. *Angew. Chemie - Int. Ed.* **2009**, *48*, 6974–6998.

4. Devaraj, N. K. The Future of Bioorthogonal Chemistry. *ACS Cent. Sci.* **2018**, *4*, 952–959.

5. Li, J.; Chen, P. R. Reactions in Bioorthogonal Chemistry. *Nat. Publ. Gr.* **2016**, *12*, 129–137.

6. Yang, M.; Li, J.; Chen, P. R. Transition Metal-Mediated Bioorthogonal Protein Chemistry in Living Cells. *Chem. Soc. Rev.* **2014**, *43*, 6511–6526.

7. Hang, H. C.; Yu, C.; Kato, D. L.; Bertozzi, C. R. A Metabolic Labeling Approach toward Proteomic Analysis of Mucin-Type O-Linked Glycosylation. *Proc. Natl. Acad. Sci.* **2003**, *100*, 14846–14851.

8. Hein, J. E.; Fokin, V. V. Copper-Catalyzed Azide–Alkyne Cycloaddition (CuAAC) and beyond: New Reactivity of Copper(I) Acetylides. *Chem. Soc. Rev.* **2010**, *39*, 1302–1315.

9. Thirumurugan, P.; Matosiuk, D.; Jozwiak, K. Click Chemistry for Drug Development and Diverse Chemical–Biology Applications. *Chem. Rev.* **2013**, *113*, 4905–4979.

10. Liang, L.; Astruc, D. The Copper(I)-Catalyzed Alkyne-Azide Cycloaddition (CuAAC) "Click" Reaction and Its Applications. An Overview. *Coord. Chem. Rev.* **2011**, *255*, 2933–2945.

11. Kolb, H. C.; Finn, M. G.; Sharpless, K. B. Click Chemistry: Diverse Chemical Function from a Few Good Reactions. *Angew. Chemie Int. Ed.* **2001**, *40*, 2004–2021.

12. Kang, K.; Park, J.; Kim, E. Tetrazine Ligation for Chemical Proteomics. *Proteome Sci.* **2017**, *15*, 15-20.

13. Becer, C. R.; Hoogenboom, R.; Schubert, U. S. Click Chemistry beyond Metal-Catalyzed Cycloaddition. *Angew. Chemie Int. Ed.* **2009**, *48*, 4900–4908.

14. Debets, M. F.; van Berkel, S. S.; Dommerholt, J.; Dirks, A. (Ton) J.; Rutjes, F. P. J. T.; van Delft, F. L. Bioconjugation with Strained Alkenes and Alkynes. *Acc. Chem. Res.* **2011**, *44*, 805–815.

15. Sletten, E. M.; Bertozzi, C. R. From Mechanism to Mouse: A Tale of Two Bioorthogonal Reactions. *Acc. Chem. Res.* **2011**, *44*, 666–676.

16 .McKay, C. S.; Finn, M. G. Click Chemistry in Complex Mixtures: Bioorthogonal Bioconjugation. *Chem. Biol.* **2014,** *21*, 1075–1101.

17. Klán, P.; Šolomek, T.; Bochet, C. G.; Blanc, A.; Givens, R.; Rubina, M.; Popik, V.; Kostikov, A.; Wirz, J. Photoremovable Protecting Groups in Chemistry and Biology: Reaction Mechanisms and Efficacy. *Chem. Rev.* **2013**, *113*, 119–191.

18. Rakhit, R.; Navarro, R.; Wandless, T. J. Chemical Biology Strategies for Posttranslational Control of Protein Function. *Chem. Biol.* **2014**, *21*, 1238–1252.

19. Xu, J.; Sun, S.; Li, Q.; Yue, Y.; Li, Y.; Shao, S. A Rapid Response "Turn-On" Fluorescent Probe for Nitroreductase Detection and Its Application in Hypoxic Tumor Cell Imaging. *Analyst* **2015**, *140*, 574–581.

20. Bae, J.; McNamara, L. E.; Nael, M. A.; Mahdi, F.; Doerksen, R. J.; Bidwell, G. L.; Hammer, N. I.; Jo, S. Nitroreductase-Triggered Activation of a Novel Caged Fluorescent Probe Obtained from Methylene Blue. *Chem. Commun.* **2015**, *51*, 12787–12790.

21. Völker, T.; Meggers, E. Transition-Metal-Mediated Uncaging in Living Human Cells-an Emerging Alternative to Photolabile Protecting Groups. *Curr. Opin. Chem. Biol.* **2015**, *25*, 48–54.

22. Sasmal, P. K.; Streu, C. N.; Meggers, E. Metal Complex Catalysis in Living Biological Systems. *Chem. Commun.* **2013**, *49*, 1581–1587.

23. Li, J.; Chen, P. R. Development and Application of Bond Cleavage Reactions in Bioorthogonal Chemistry. *Nat. Chem. Biol.* **2016**, *12*, 129-137.

24. Bai, Y.; Chen, J.; Zimmerman, S. C. Designed Transition Metal Catalysts for Intracellular Organic Synthesis. *Chem. Soc. Rev.* **2018**, *47*, 1811–1821.

25. Streu, C.; Meggers, E. Ruthenium-Induced Allylcarbamate Cleavage in Living Cells. *Angew. Chemie - Int. Ed.* **2006**, *45*, 5645–5648.

26. Völker, T.; Dempwolff, F.; Graumann, P. L.; Meggers, E. Progress towards Bioorthogonal Catalysis with Organometallic Compounds. *Angew. Chem. Int. Ed. Engl.* **2014**, *53*, 10536–10540.

27. Vçlker, T.; Meggers, E. Chemical Activation in Blood Serum and Human Cell Culture : Improved Ruthenium Complex for Catalytic Uncaging of Alloc-Protected Amines. **2017**, *24,* 1083–1086.

28. Sasmal, P. K.; Carregal-Romero, S.; Han, A. A.; Streu, C. N.; Lin, Z.; Namikawa, K.; Elliott, S. L.; Köster, R. W.; Parak, W. J.; Meggers, E. Catalytic Azide Reduction in Biological Environments. *ChemBioChem* **2012**, *13*, 1116–1120.

29. Yusop, R. M.; Unciti-broceta, A.; Johansson, E. M. V; Sa, R. M.; Bradley, M. Palladium-Mediated Intracellular Chemistry. **2011**, *3*, 239–243.

30. Weiss, J. T.; Dawson, J. C.; Macleod, K. G.; Rybski, W.; Fraser, C.; Torres-Sánchez, C.; Patton, E. E.; Bradley, M.; Carragher, N. O.; Unciti-Broceta, A. Extracellular Palladium-Catalysed Dealkylation of 5-Fluoro-1-Propargyl-Uracil as a Bioorthogonally Activated Prodrug Approach. *Nat. Commun.* **2014**, *5*, 3277-3285.

31. Weiss, J. T.; Dawson, J. C.; Fraser, C.; Rybski, W.; Torres-Sánchez, C.; Bradley, M.; Patton, E. E.; Carragher, N. O.; Unciti-Broceta, A. Development and Bioorthogonal Activation of Palladium-Labile Prodrugs of Gemcitabine. *J. Med. Chem.* **2014,** *57*, 5395–5404.

32. Bray, T. L.; Salji, M.; Brombin, A.; Pérez-López, A. M.; Rubio-Ruiz, B.; Galbraith, L. C. A.; Patton, E. E.; Leung, H. Y.; Unciti-Broceta, A. Bright Insights into Palladium-Triggered Local Chemotherapy. *Chem. Sci.* **2018**, *9*, 7354–7361.

33. Clavadetscher, J.; Indrigo, E.; Chankeshwara, S. V; Lilienkampf, A.; Bradley, M. In-Cell Dual Drug Synthesis by Cancer-Targeting Palladium Catalysts. *Angew. Chemie* **2017**, *129*, 6968–6972.

34. Weiss, J. T.; Carragher, N. O.; Unciti-Broceta, A. Palladium-Mediated Dealkylation of N-Propargyl-Floxuridine as a Bioorthogonal Oxygen-Independent Prodrug Strategy. *Sci. Rep.* **2015**, *5*, 9329-9333.

35. Torchilin, V. P. Recent Advances with Liposomes as Pharmaceutical Carriers. *Nat. Rev. Drug Discov.* **2005**, *4*, 145–160.

36. Lee, Y. W.; Luther, D. C.; Kretzmann, J. A.; Burden, A.; Jeon, T.; Zhai, S.; Rotello, V. M. Protein Delivery into the Cell Cytosol Using Non-Viral Nanocarriers. *Theranostics* **2019**, *9*, 3280–3292.

37. Gupta, A.; Mumtaz, S.; Li, C.-H.; Hussain, I.; Rotello, V. M. Combatting Antibiotic-Resistant Bacteria Using Nanomaterials. *Chem. Soc. Rev.* **2019**, *48*, 415–427.

38. Jiang, Y.; Hardie, J.; Liu, Y.; Ray, M.; Luo, X.; Das, R.; Landis, R. F.; Farkas, M. E.; Rotello, V. M. Nanocapsule-Mediated Cytosolic SiRNA Delivery for Anti-Inflammatory Treatment. *J. Control. Release* **2018**, *283*, 235–240.

39. Gupta, A.; Landis, R. F.; Li, C.-H.; Schnurr, M.; Das, R.; Lee, Y.-W.; Yazdani, M.; Liu, Y.; Kozlova, A.; Rotello, V. M. Engineered Polymer Nanoparticles with Unprecedented Antimicrobial Efficacy and Therapeutic Indices against Multidrug-Resistant Bacteria and Biofilms. *J. Am. Chem. Soc.* **2018**, *140*, 12137–12143.

40. Davis, M. E.; Chen, Z.; Shin, D. M. Nanoparticle Therapeutics: An Emerging Treatment Modality for Cancer. *Nat. Rev. Drug Discov.* **2008**, *7*, 771.

41. Brannon-Peppas, L.; Blanchette, J. O. Corrigendum to "Nanoparticle and Targeted Systems for Cancer Therapy" *Adv. Drug Deliv. Rev.* **2009**, *61*, 364-371.

42. van Dongen, S. F. M.; de Hoog, H.-P. M.; Peters, R. J. R. W.; Nallani, M.; Nolte, R. J. M.; van Hest, J. C. M. Biohybrid Polymer Capsules. *Chem. Rev.* **2009**, *109*, 6212–6274.

43. Navya, P. N.; Kaphle, A.; Srinivas, S. P.; Bhargava, S. K.; Rotello, V. M.; Daima, H. K. Current Trends and Challenges in Cancer Management and Therapy Using Designer Nanomaterials. *Nano Converg.* **2019**, *6*, 23-30.

44. Rana, S.; Bajaj, A.; Mout, R.; Rotello, V. M. Monolayer Coated Gold Nanoparticles for Delivery Applications. *Adv. Drug Deliv. Rev.* **2012,** *64*, 200–216.

45. Yesilbag Tonga, G.; Mizuhara, T.; Saha, K.; Jiang, Z.; Hou, S.; Das, R.; Rotello, V. M. Binding Studies of Cucurbit[7]Uril with Gold Nanoparticles Bearing Different Surface Functionalities. *Tetrahedron Lett.* **2015**, *56*, 3653–3657.

46. Ghosh, P.; Han, G.; De, M.; Kim, C. K.; Rotello, V. M. Gold Nanoparticles in Delivery Applications. *Adv. Drug Deliv. Rev.* **2008,** *60*, 1307–1315.

47. Moyano, D. M.; Rotello, V. M.; Preparation of 2 Nm Gold Nanoparticles for in Vitro and in Vivo Applications. *Methods Mol. Biol.* **2013,** *1025*, 3-6.

48. Gupta, A.; Moyano, D. F.; Parnsubsakul, A.; Papadopoulos, A.; Wang, L.-S.; Landis, R. F.; Das, R.; Rotello, V. M. Ultrastable and Biofunctionalizable Gold Nanoparticles. *ACS Appl. Mater. Interfaces* **2016,** *8*, 14096–14101.

49. Saha, K.; Agasti, S. S.; Kim, C.; Li, X.; Rotello, V. M. Gold Nanoparticles in Chemical and Biological Sensing. *Chem. Rev.* **2012**, *112*, 2739–2779.

50. Brust, M.; Walker, M.; Bethell, D.; Schiffrin, D. J.; Whyman, R. Synthesis of Thiol-Derivatised Gold Nanoparticles in a Two-Phase Liquid-Liquid System. *J. Chem. Soc. Chem. Commun.* **1994**, 801–802.

51. Hostetler, M. J.; Templeton, A. C.; Murray, R. W. Dynamics of Place-Exchange Reactions on Monolayer-Protected Gold Cluster Molecules. *Langmuir* **1999**, *15*, 3782–3789.

52. Hong, R.; Fischer, N. O.; Verma, A.; Goodman, C. M.; Emrick, T.; Rotello, V. M. Control of Protein Structure and Function through Surface Recognition by Tailored Nanoparticle Scaffolds. *J. Am. Chem. Soc.* **2004**, *126*, 739–743.

53. Jordan, B. J.; Hong, R.; Han, G.; Rana, S.; Rotello, V. M. Modulation of Enzyme–Substrate Selectivity Using Tetraethylene Glycol Functionalized Gold Nanoparticles. *Nanotechnology* **2009**, *20*, 434004-434011.

54. You, C.-C.; De, M.; Rotello, V. M. Contrasting Effects of Exterior and Interior Hydrophobic Moieties in the Complexation of Amino Acid Functionalized Gold Clusters with α-Chymotrypsin. *Org. Lett.* **2005**, *7*, 5685–5688.

55. Zhang, X.-Q.; Xu, X.; Lam, R.; Giljohann, D.; Ho, D.; Mirkin, C. A. Strategy for Increasing Drug Solubility and Efficacy through Covalent Attachment to Polyvalent DNA–Nanoparticle Conjugates. *ACS Nano* **2011**, *5*, 6962–6970.

56. Gibson, J. D.; Khanal, B. P.; Zubarev, E. R. Paclitaxel-Functionalized Gold Nanoparticles. *J. Am. Chem. Soc.* **2007**, *129*, 11653–11661.

57. Dhar, S.; Daniel, W. L.; Giljohann, D. A.; Mirkin, C. A.; Lippard, S. J. Polyvalent Oligonucleotide Gold Nanoparticle Conjugates as Delivery Vehicles for Platinum(IV) Warheads. *J. Am. Chem. Soc.* **2009**, *131*, 14652–14653.

58. Hong, R.; Han, G.; Fernández, J. M.; Kim, B.; Forbes, N. S.; Rotello, V. M. Glutathione-Mediated Delivery and Release Using Monolayer Protected Nanoparticle Carriers. *J. Am. Chem. Soc.* **2006**, *128*, 1078–1079.

59. Kim, C. K.; Ghosh, P.; Pagliuca, C.; Zhu, Z. J.; Menichetti, S.; Rotello, V. M. Entrapment of Hydrophobic Drugs in Nanoparticle Monolayers with Efficient Release into Cancer Cells. *J. Am. Chem. Soc.* **2009**, *131*, 1360–1361.

60. Jeong, Y.; Tonga, G. Y.; Duncan, B.; Yan, B.; Das, R.; Sahub, C.; Rotello, V. M. Solubilization of Hydrophobic Catalysts Using Nanoparticle Hosts. *Small* **2018**, *14*, 1702198-1702210.

61. Tonga, G. Y.; Jeong, Y.; Duncan, B.; Mizuhara, T.; Mout, R.; Das, R.; Kim, S. T.; Yeh, Y.-C.; Yan, B.; Hou, S.; *et al.* Supramolecular Regulation of Bioorthogonal Catalysis in Cells Using Nanoparticle-Embedded Transition Metal Catalysts. *Nat. Chem.* **2015**, *7*, 597–603.

62. Cao-Milán, R.; He, L. D.; Shorkey, S.; Tonga, G. Y.; Wang, L.-S.; Zhang, X.; Uddin, I.; Das, R.; Sulak, M.; Rotello, V. M. Modulating the Catalytic Activity of Enzyme-like Nanoparticles through Their Surface Functionalization. *Mol. Syst. Des. Eng.* **2017**, *2*, 624–628.

63. Zhang, X.; Huang, R.; Gopalakrishnan, S.; Cao-milán, R.; Rotello, V. M. Bioorthogonal Nanozymes : Progress towards Therapeutic Applications. *Trends. Chem.* **2019**, *1,* 90-98.

64. Gupta, A.; Das, R.; Yesilbag Tonga, G.; Mizuhara, T.; Rotello, V. M. Charge-Switchable Nanozymes for Bioorthogonal Imaging of Biofilm-Associated Infections. *ACS Nano* **2018**, *12*, 89–94.

65. Das, R.; Landis, R. F.; Tonga, G. Y.; Cao-Milán, R.; Luther, D. C.; Rotello, V. M. Control of Intra- versus Extracellular Bioorthogonal Catalysis Using Surface-Engineered Nanozymes. *ACS Nano* **2019,** *13,* 229-235.

CHAPTER 2

CONTROL OF INTRA- VERSUS EXTRACELLULAR BIOORTHOGONAL CATALYSIS USING SURFACE-ENGINEERED NANOZYMES

2.1 Introduction

Bioorthogonal chemistry is an emerging tool for interrogating and modulating cellular bioprocesses, harnessing the toolkit of synthetic chemistry to perform transformations outside the capabilities of biological systems.[1-5] Bioorthogonal catalysis extends this capability, providing a platform for the transformation of substrates that mimics the catalytic amplification provided by enzymes in biological reactions. Transition metal catalysts (TMCs) are highly efficient systems for bioorthogonal activation of prodrugs and profluorophores.[6-11] However, maintaining activity while controlling the localization of these systems remains an important issue.[12]

Spatial localization of therapeutics and imaging agents is central to their utility in biomedicine, with different applications requiring either intra- or extracellular localization. Intracellular activation of prodrugs provides direct access to intracellular machinery for therapeutic intervention.[12- 18] In contrast, extracellular targeting is important for regulating cell-surface signaling pathways,[19,20] as well as when using cell-impermeable substrates as prodrugs[21,22] or when targeting necrotic areas in tumors.[23-25]

Incorporation of TMCs into nanoparticle monolayers provides a versatile strategy for creation of bioorthogonal nanocatalyst 'nanozymes'. In recent studies we have shown that the use of 2 nm AuNPs provides stabilization of the catalysts in a package of similar size to many enzymes (~8 nm),[17,26] featuring high catalytic activity in complex cellular media. We hypothesized that surface engineering of these nanozymes could be used to dictate either extra- or intracellular catalysis, expanding the utility of this platform for biomedical applications. We report here the use of surface functionalization to provide effective localization of nanozymes and their catalytic activity,[27] using cell-penetrating cationic nanoparticles for intracellular catalysis[28,29] and 'stealth'

zwitterionic particles to limit catalysis to extracellular space.[28,30] Specific localization of nanozyme activity was demonstrated through profluorophore activation and therapeutic activation was demonstrated through intra- and extracellular activation of a prodrug. We observed that cationic nanozymes demonstrate significantly higher therapeutic efficacy as compared to their zwitterionic counterparts. The enhanced therapeutic efficacy exhibited by cationic nanozymes can be attributed to the stronger impact of intracellular drug activation coupled with somewhat higher catalytic rate of cationic nanozymes. These findings provide us with a modular approach to control the therapeutic efficacy of the drug through controlled bio-orthogonal activation. Taken together, these studies demonstrate enhanced spatial control for TMC-mediated bioorthogonal catalysis.

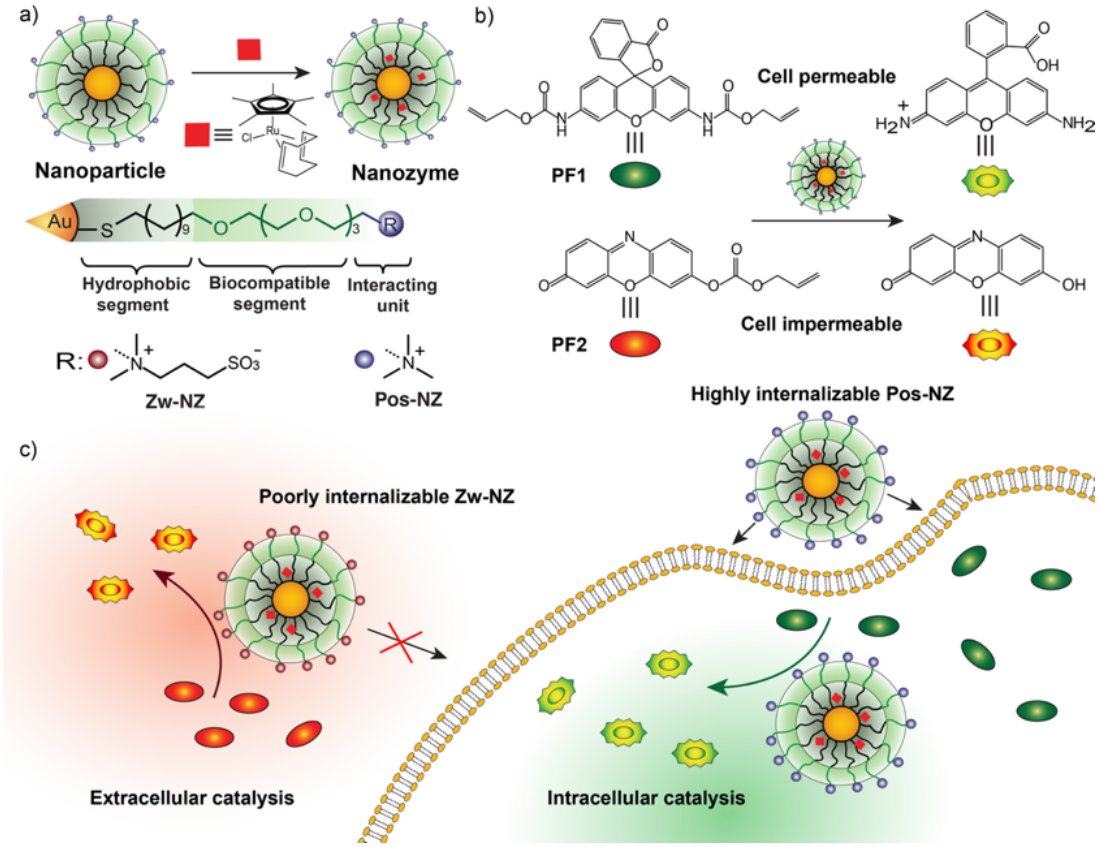

Figure 2.1. a) Schematic representation of nanoparticles, nanozymes, and chemical structures of ligands of cationic nanozymes (Pos-NZ) and zwitterionic nanozymes (Zw-NZ) b) Structures of the pro-fluorescent substrates rhodamine 110 derivative (PF1) and resorufin derivative (PF2) and fluorescent products (rhodamine 110 and resorufin) after allylcarbamate/carbonate cleavage by TMC c) Schematic representation of specific localization of nanozymes using surface functionality; activation of PF1 in intracellular region and PF2 in extracellular region.

2.2 Results and Discussions

AuNP (2 nm core) scaffolds were functionalized with ligands featuring three crucial components: (1) a hydrophobic interior segment that encapsulates the lipophilic TMCs, (2) a tetraethylene glycol spacer to provide biocompatibility, and (3) a terminal interacting unit that dictates intra/extracellular nanozyme localization (Figure 1). Positively charged quaternary ammonium ligands were used to generate Pos-NPs that were used for intracellular localization due to their high level of cellular uptake.[31,32] Zw-NPs scaffolds functionalized with zwitterionic sulfobetaine moieties were used for extracellular localization based on their minimal cellular uptake.[33] (Figure 2.1). Both particles were synthesized from pentanethiol capped 2 nm core AuNPs scaffolds using place-exchange reaction (synthesis and characterization of nanoparticles are described in supporting information, Figures 2.S1, 2.S2, 2.S4 and 2.S5).

Nanozymes were generated by catalyst encapsulation in AuNP monolayer of Pos-NPs[28] and Zw-NPs,[30] to generate cationic Pos-NZ and zwitterionic (neutral) Zw-NZ nanozymes, respectively (Figure 1a). In this procedure the catalyst [Cp*Ru(cod)Cl] (Cp*= pentamethylcyclopentadienyl, cod=1,5-cyclooctadiene)[34] was dissolved in acetone and added into an aqueous solution of the corresponding AuNPs in 1:1 volumetric ratio. Slow evaporation of acetone followed by purification to remove excess catalyst (details are in materials and methods section) provided the desired nanozymes.

Transmission electron microscopy (TEM) and dynamic light scattering (DLS) indicate no aggregation of nanozymes after encapsulation of TMCs (Table 2.S1 and Figures 2.S2-2.S4). The quantification of ruthenium catalysts encapsulated in the corresponding nanozymes was obtained using inductively coupled plasma mass spectrometry (ICP-MS, Table 2.S2), with similar encapsulation efficiency observed with the two particles: Pos-NZ (29 catalysts per AuNP) and Zw-NZ (24 catalysts per AuNP).

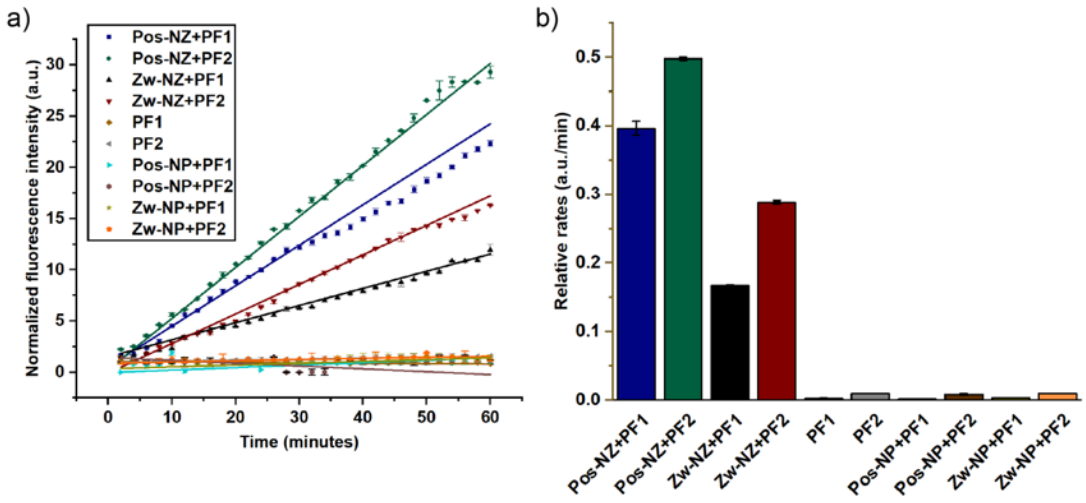

Figure 2.2. a) Normalized fluorescence intensity (fluorescence at time t divided by the initial fluorescence intensity) of pro-fluorophores PF1 and PF2 (1 μM) by nanozymes (400 nM), b) relative rates of activation of PF1 and PF2 by nanozymes. Activity of Pos-NZ (blue and green) and Zw-NZ (black and red) were determined in sodium phosphate buffer (5 mM, pH 7.4) for 1 h. Potential activation of PF1 and PF2 by nanoparticles (Pos-NPs and Zw-NPs) was probed as negative controls. The data are average of triplicates and the error bars indicate standard deviations.

The catalytic activity of nanozymes Pos-NZ and Zw-NZ was quantified by monitoring the deallylation-mediated fluorogenesis of two pro-fluorophores; alloc-protected rhodamine 110 (PF1) and alloc-protected resorufin (PF2) (Figure 2.1). A linear increase of fluorescence was observed after introducing the nanozymes into the pro-fluorophore solutions (Figure 2.2a), indicating that the Ru catalysts maintain their catalytic activity after encapsulation. The relative rate of increase in fluorescence intensity was measured from the slopes of the normalized intensities (Figure 2.2b). In the presence of Pos-NZ and Zw-NZ, the slope for PF1 activation was increased by 177- and 75-fold respectively, and for PF2 activation was increased by 51- and 30-fold respectively (Figure 2.2b) relative to PF1 and PF2 alone. AuNPs (Pos-NP and Zw-NP) incubated with dyes (PF1 and PF2) were used as negative controls, exhibiting no increase in the fluorescence intensity. Next, we further assessed the catalytic activity of nanozymes over longer timeframes. Nanozymes (Pos-NZ and Zw-NZ) retained their catalytic activity even after 72 hours of incubation with the substrate, as

evidenced in the fluorophore activation studies (Figure 2.S6). Fluorophore conversion rates for PF1 and PF2 with nanozymes were calculated and are reported in supporting information (Table 2.S3).

We next investigated the selective cellular uptake of Zw-NZs and Pos-NZs in HeLa (Figure 2.3a) and RAW 264.7 macrophage cells (Figure 2.3b) using ICP-MS. We observed that cells treated with Pos-NZs showed high content of Au, whereas cells treated with Zw-NZs showed minimal uptake of Au.[30] The amount of Ru catalysts found inside the cells was also quantified with consistent results (Figure 2.3). We further assessed the nanozyme uptake in the cells for extended duration of 72 h and the results mirrored the trend for 24 h incubation of nanozymes (Figure 2.S7). Next, the catalytic activity of these nanozymes after 72 h *in vitro* incubation was assessed through pro-fluorophore activation using confocal microscopy (Figure 2.S8). The activation of pro-fluorophores inside the cells after extended period of cell incubation indicates the long-term stability of nanozymes.

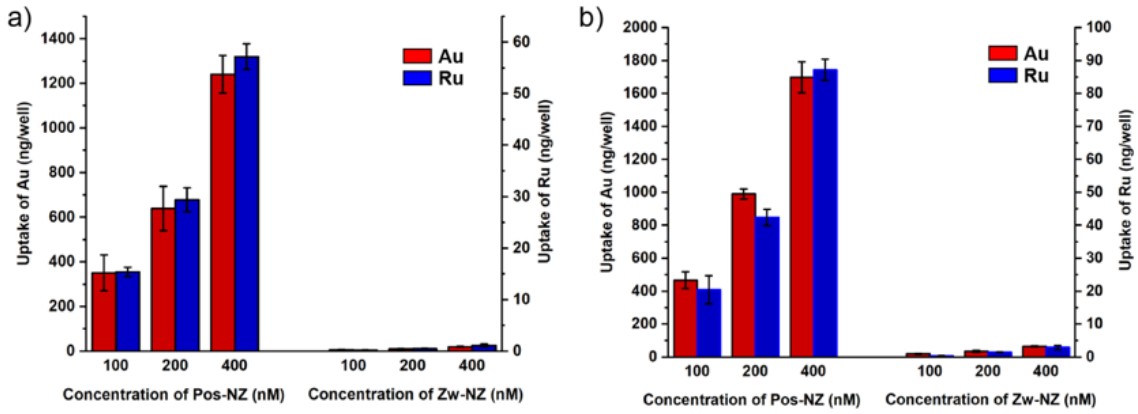

Figure 2.3. Cellular uptake of nanoparticle and TMC in a) HeLa (20,000 cells/well) b) RAW 264.7 (20,000 cells/well) after overnight incubation with Pos-NZ and Zw-NZ with increasing concentration. The data are average of triplicates and the error bars indicate standard deviations.

After establishing the differential uptake of the nanozymes in cell lines, we next investigated the ability of nanozymes to activate profluorophores inside and outside the cells. We chose two fluorophores with different emission wavelengths and different molecular polarities for better visualization of catalysis in extra- and intracellular environments (Figure 2.1c). Rhodamine derivative PF1 (green emitter) was used to visualize intracellular catalysis due to its high

permeability across the cell membrane.[12,35] Less cell-permeable resorufin derivative PF2 (red emitter) was chosen to visualize extracellular catalysis.[36,37] Cells were treated with PF1 overnight, followed by multiple washings to remove non-absorbed PF1 molecules (Figures 2.4a, b, d). Fresh media containing Pos-NZ was added to the cells for 0.5 h (Figures 2.4b, d). Non-adhered Pos-NZs were washed away followed by addition of Zw-NZ and PF2 into the cells (Figure 2.4d). After incubation with nanozymes and substrates, the cells were observed under a confocal microscope. As expected, substrates PF1 and PF2 did not exhibit any fluorescence in absence of nanozymes (Figure 2.4a). Cells treated with only Pos-NZ and PF1 showed intracellular fluorescence (Figure 2.4b), while only Zw-NZ and PF2 showed extracellular fluorescence (Figure 2.4c). In presence of both the nanozymes and profluorophores, the cells exhibited green fluorescence inside the cells and a bright red fluorescence outside the cells demonstrating the ability of the nanozyme-based bioorthogonal system to activate different profluorophores with controlled spatial localization (Figures 2.4d and 2.S9). Intra-extracellular activation of pro-fluorophore was further investigated by altering the incubation order of cells with reagents *i.e.*, the cells were treated with Pos-NZ, followed by PF1, Zw-NZ and PF2. No difference was observed upon changing the order of incubation of the reactive components, indicating strong spatial control of the nanozymes (Figure 2.S10a). As additional controls, cells treated with Pos-NZ and PF2 (Figure 2.S10b) and Zw-NZ and PF1 (Figure 2.S10c) were visualized under confocal microscope. No fluorescence was observed, demonstrating controlled activation of the pro-fluorophores.

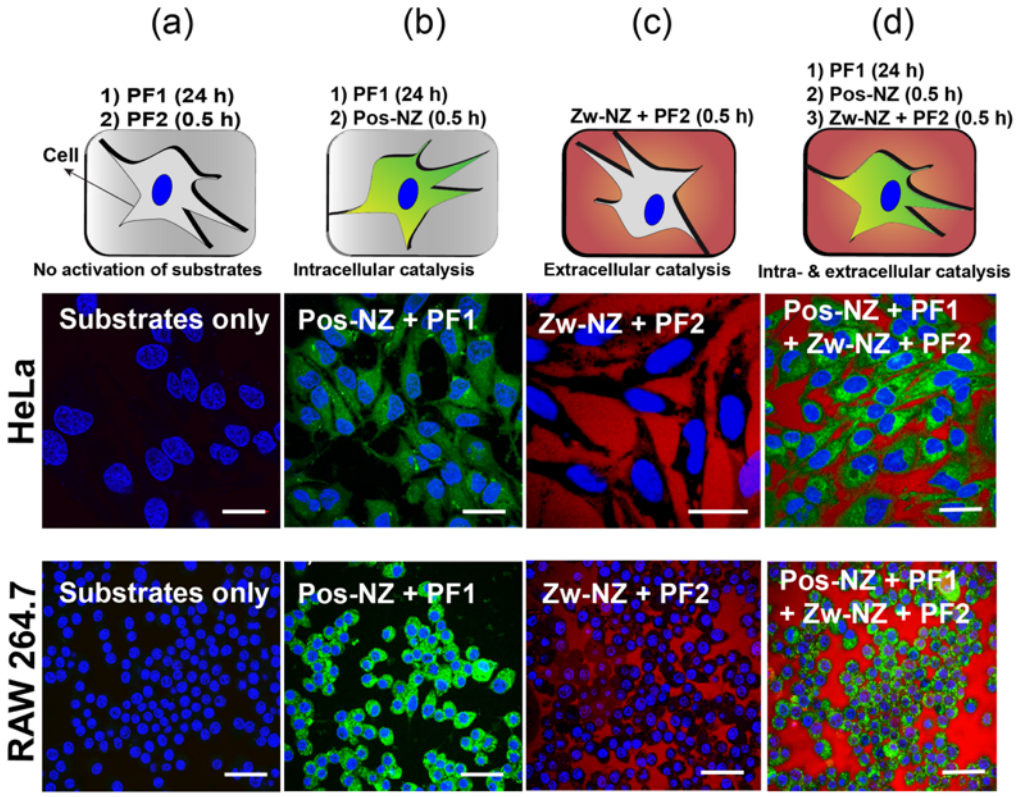

Figure 2.4. Schematic representation and confocal imaging of controlled spatial activation of PF1 and PF2 by treatment with bioorthogonal nanozymes Pos-NZ and Zw-NZ, respectively in HeLa and macrophages (RAW 264.7) observing a) no activation of substrates in absence of nanozymes b) intracellular catalysis in presence of only Pos-NZ and PF1 c) extracellular catalysis in presence of only Zw-NZ and PF2 d) intra- and extracellular catalysis in presence of both the nanozymes and profluorophores. Nuclei were stained by Hoechst 33342. Scale bars, 25 μm.

We next assessed the ability of nanozymes to selectively activate prodrugs inside and outside the cells as a measure for relevant therapeutic applications. For this study, allylcarbamate protected doxorubicin (pro-Dox) was chosen as a model prodrug due to the high clinical relevance of its counterpart drug in cancer chemotherapy (Figure 2.5a).[38-41] The caged amine group blocks the pharmacophore, preventing cytotoxicity prior to activation (Figure 2.S11). Cell viability studies were performed on HeLa cells using nanozymes and prodrugs to assess activation capacity of nanozymes for prodrugs in physiologically relevant conditions (Figure 2.5).

For cell viability studies, HeLa cells were incubated with nanozymes (50 and 100 nM) and different concentrations of pro-Dox for 24 h (detailed description is provided in materials and

methods section). Cells incubated with only pro-Dox and free Dox were used as negative and positive controls, respectively. Figure 2.5b shows that pro-Dox does not show toxicity to cells. The viability of prodrug-treated cells is substantially reduced in the presence of our nanozymes however, indicating the successful catalytic activation of the prodrug. Cells co-incubated with pro-Dox and Pos-NZ (100 nM) displayed significantly lower viability than cells co-incubated with pro-Dox and Zw-NZ (100 nM). As a control, cell-viability studies were also done after altering the order of intracellular nanozyme and prodrug and no significant difference was observed (Figure 2.S12), illustrating the modular nature of our approach. Notably, Pos-NZ dominates the therapeutic effect when used in combination with Zw-NZ. This phenomenon can be attributed to stronger toxicity of intracellularly activated drug molecules as compared to the drugs activated outside the cells. Additionally, Pos-NZ exhibits higher catalytic activity as compared to Zw-NZ (Figure 2.2), which further amplifies the difference in their therapeutic impact. However, the combined therapeutic effect of mixture of Pos-NZ and Zw-NZ is higher than their individual components owing to the simultaneous activation of the prodrug by both nanozymes, increasing the total amount of drug molecules activated. These results indicating, as one might expect, that the intracellular activation of pro-Dox provides higher therapeutic efficacy than does extracellular activation, demonstrating the role of intracellular nanozyme localization in dictating desired therapeutic activity.

2.3 Conclusions

In summary, we have demonstrated the use of engineered nanozymes to predictably localize bioorthogonal catalysis to either extra- or intracellular space. The nanozymes were fabricated by encapsulating TMCs in the hydrophobic core of these surface functionalized AuNPs. A cell penetrating cationic AuNP scaffold was used for intracellular catalysis and a ‘stealth’ zwitterionic scaffold was used to limit catalysis to outside the cells. The ability of these engineered nanozymes to spatially localize catalysis heralds their use for therapeutic applications such as site-specific activation of prodrugs for regulated therapeutic dosing and facilitating penetration of

membrane-impermeable drugs. Additionally, this strategy provides a means for activation of imaging agents in intra- and extracellular domains for diagnostic applications, with amplification arising from the catalytic capabilities of the nanozyme platform. Notably, TMCs must exhibit long-term stability in the hydrophobic monolayer of nanoparticles to provide a stable catalytic machinery, while the substrates must easily transition to a hydrophilic analogue upon activation to generate an effective pair with the nanozymes for efficient catalysis. Taken together, these studies provide a promising strategy for spatially controlling TMC mediated bioorthogonal catalysis for diagnosis and therapeutic applications.

2.4 Experimental methods

2.4.1 Synthesis of AuNPs. 2 nm diameter gold nanoparticles were synthetized by the Brust-Schiffrin two-phase methodology using pentanethiol as the stabilizer; these clusters were purified with successive extractions with ethanol and acetone. A Murray place exchange reaction was carried out in dry DCM to functionalize the nanoparticles with each ligand.[42,43] The monolayer-protected nanoparticles were redispersed in water and the excesses of ligand/pentanethiol were removed by dialysis using a 10,000 MWCO snake-skin membrane. The final concentration was measured by UV spectroscopy on a Molecular Devices SpectraMax M2 at 506 nm according to the reported methodology.

2.4.2 Catalyst encapsulation in AuNP monolayer: 1 mL acetone was used to dissolve 2 mg of the catalyst [Cp*Ru(cod)Cl] and mixed with 1 mL aqueous solution of the corresponding AuNPs (20 μM). The organic phase was slowly evaporated from the mixture using a rotary evaporator. Excess catalysts were removed from solution by filtration (Millex-GP filter; 25 mm PES, pore Size: 0.22 μm). Further purifications were done by centrifugal filters (five times, Amicon® ultra 4, 10K). The amount of encapsulated catalysts in each AuNPs was measured by ICP-MS by tracking ^{101}Ru relative to ^{197}Au.

2.4.3 Nanozyme kinetics in Solution: Allylcarbamate protected rhodamine 110 (PF1, green) and allylcarbonate protected resorufin (PF2, red) were used as substrates to test the catalytic activity of Pos-NZ and Zw-NZ. A solution containing 400 nM nanozyme and 1 μM substrate was prepared in a 96-well plate. 1 μM substrate solutions alone were used as negative controls. The kinetic study was done by tracking the fluorescence intensity of PF1 (λ_{ex} = 488 nm, λ_{em} = 521 nm) and PF2 (λ_{ex} = 543 nm, λ_{em} = 590 nm) using a Molecular Devices SpectraMax M2 microplate reader.

2.4.4 Cellular uptake of the nanozymes: 20k HeLa and RAW 264.7 cells/well were plated in a 24-well plate prior to the experiment. Next day, the cells were washed with PBS and incubated with Pos-NZ and Zw-NZ (100, 200 and 400 nM) in 10% serum-containing media for 24 h, 48 h and 72 h at 37 °C. Subsequently, the cells were washed with PBS to remove any excess nanozymes and then subjected to lysis buffer. The lysed cells were then further processed for ICP-MS analysis. Each experiment was comprised of 3 replicates.

2.4.5 Confocal imaging of catalysis inside and outside the cells: HeLa cells and RAW 264.7 cells were grown in cell culture flasks using Dulbecco's modified Eagle medium with 10% fetal bovine serum, at 37 °C in a humidified atmosphere of 5% CO_2. For confocal analysis, HeLa and RAW 264.7 cells were seeded at 200k in 2 mL 10% serum-containing media in the confocal dish 24 h before the experiment. During the experiment, cells were washed by PBS buffer three times and old media was replaced by substrate PF1 (100 μM) in serum-containing media, and the cells were incubated for 24 h and washed with PBS buffer three times. The Pos-NZs (200 nM) were then added to the cells and incubated for 0.5 h. The cells were washed with PBS three times to remove excess Pos-NZ. Then a serum-containing media with a freshly prepared mixture of Zw-NZs (200 nM) and PF2 (100 μM) was added to the washed cells. Confocal microscopy images were obtained after 0.5 h on a Nikon A1 spectral detector confocal microscope (A1SP) using a 60x objective. The settings of the confocal microscope were as follows (unless otherwise specified):

green channel, λ_{ex} = 488 nm and λ_{em} = BP 505-530 nm; red channel, λ_{ex} = 561 nm and λ_{em} = LP 590 nm. Emission filters: BP, band pass; LP, high pass.

2.4.6 Prodrug activation: HeLa cells were seeded at 10k in 0.2 mL per well in 96-well plates 24 h before the experiment. Cells were washed off and incubated with Pos-NZ (50 nM) in 10% serum-containing media. After 24 h, cells were washed with PBS buffer three times and treated with Zw-NZ (50 nM) and pro-Dox at a concentration of 0.5, 1, 2, and 4 μM for 24 h. The cells were then completely washed off and 10% alamar blue in serum-containing media was added to each well (220 μL) and incubated further at 37°C for 2 h. Cell viability was then determined by measuring the fluorescence intensity at 570 nm using a SpectraMax M5 microplate spectrophotometer. Absorbance spectra of free DOX was studied indicating no signal at 570 nm (Figure 2.S13).

2.5 Supplementary information

2.5.1 Mass spectrometric characterization of ligand on NPs. Matrix assisted laser desorption/ionization mass spectroscopy (MALDI-MS) was performed to characterize the surface ligand on the Pos-NP and Zw-NP. A matrix stock solution of α-Cyano-4-hydroxycinnamic acid (α-CHCA) was prepared in 70% acetonitrile, 30% deionized (DI) water. A mixture of 1 μM AuNPs solution and the matrix was prepared in 1:1 volume ratio. 2 μL of this mixture was spotted to the sample carrier and was allowed to stand for a few minutes to evaporate the solvent. MALDI-MS analysis was performed on a Bruker Autoflex III mass spectrometer. The peaks at m/z 422 and 530 were detected for Pos-NP and Zw-NP respectively.

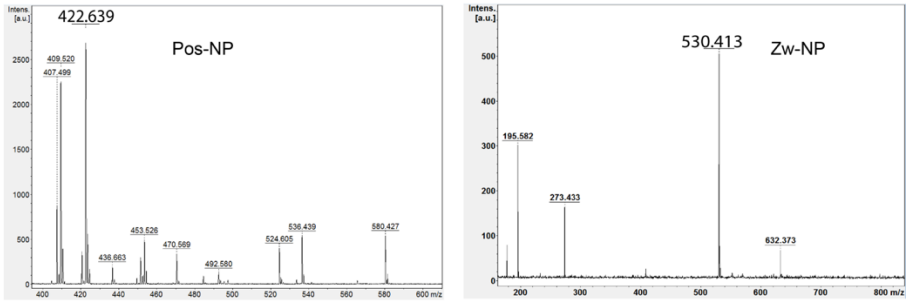

Figure 2.5. MALDI-MS for Pos-NP and Zw-NP.

2.5.2 DLS and TEM characterization of nanoparticles and nanozymes. Hydrodynamic diameter of the nanoparticles and nanozymes were measured by dynamic light scattering (DLS) in DI water using a Malvern Zetasizer Nano ZS instrument by using the measurement angle of 173° (backscatter). Data were analyzed by the "multiple narrow modes" (high resolution) based on non-negative-least-squares (NNLS).

Table 2.1. The size of nanoparticles (Pos-NP and Zw-NP) and nanozymes (Pos-NZ and Zw-NZ) obtained from DLS

Sample	Size (nm)	Sample	Size (nm)
Pos-NP	8.2 ± 2.1	Pos-NZ	9.1 ± 2.1
Zw-NP	8.1 ± 2.0	Zw-NZ	8.1 ± 1.7

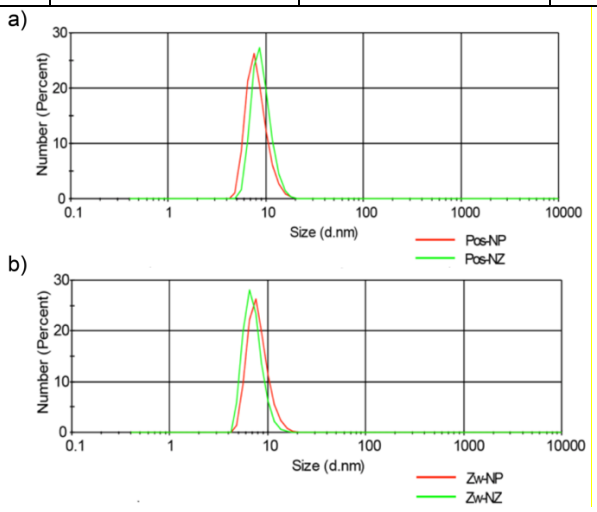

Figure 2.6. DLS measurements of a) Pos-NP and Pos-NZ and b) Zw-NP and Zw-NZ, depicting that the size of nanoparticles stays the same. NP and NZ represent before and after catalyst encapsulation respectively.

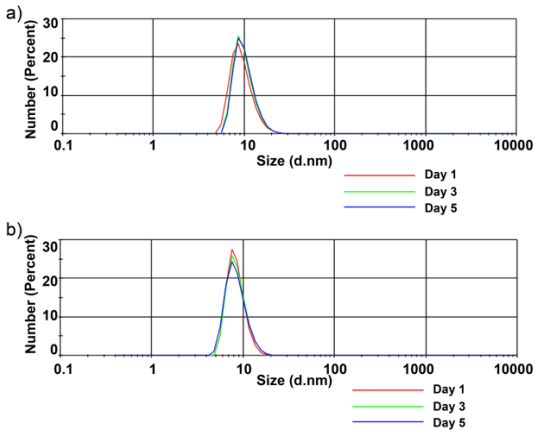

Figure 2.7. DLS measurements of a) Pos-NZ and b) Zw-NZ upto 5 days after catalyst encapsulation showing no evidence of aggregation.

2.5.3 Transmission Electron Microscopy (TEM). Images of samples were taken before (Pos-NP and Zw-NP) and after catalyst encapsulation (Pos-NZ and Zw-NZ). Samples were prepared by placing one drop of the desired solution (1 μM) onto a 300-mesh Cu grid-coated with carbon film. Then the samples were analyzed and photographed using JEOL CX-100 electron microscopy. DLS and TEM images showed that there is no aggregation or change of morphology before and after catalyst encapsulation.

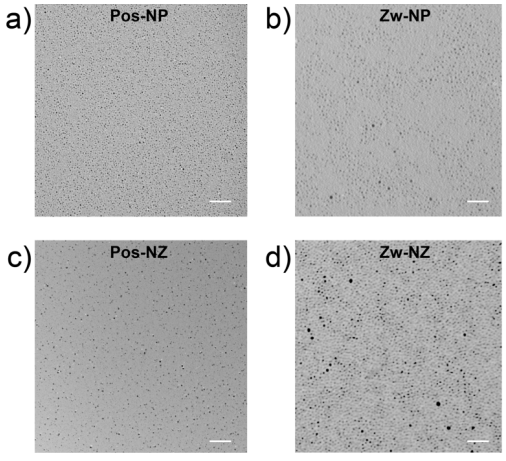

Figure 2.8. TEM images of nanoparticles before (Pos-NP and Zw-NP) and after (Pos-NZ and Zw-NZ) encapsulation of TMCs. Scale bar = 20 nm

2.5.4 Zeta Potential characterization of nanoparticles and nanozymes. Zeta potential was measured in 5 mM Phosphate buffer (pH 7.4) using a Malvern Zetasizer Nano ZS instrument.

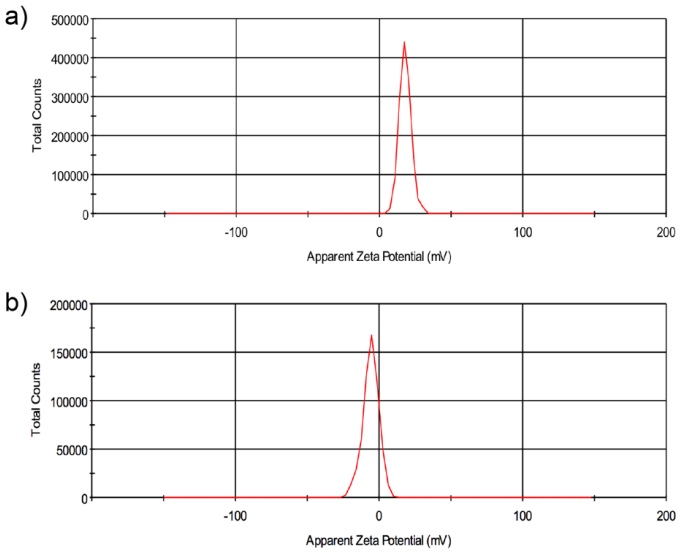

Figure 2.9. Zeta potential of a) Pos-Np (17.8 ± 4.2) and b) Zw-NP (-5.7 ± 5.6)

2.5.5 Synthesis of allyl carbamate/carbonate protected substrates. Allyl carbamate/carbonate protected substrates (PF1, PF2 and Pro-Dox) were prepared with slight variations of earlier reports:44,45

2.5.5.1 PF1. To a 10 ml pear-shaped flask equipped with a magnetic stir bar, was added Rhodamine 110 (100 mg, 0.27 mmol, 1.00 eq) and pyridine (65 µL, 0.80 mmol, 3.00 eq, ρ = 0.98 g/mL) in dry DMF (0.5 mL) and was cooled down at 0 oC. Then, the flask was purged with nitrogen. Finally, allyl chloroformate (57 µL, 0.53 mmol, 2.00 eq, ρ = 1.13 g/mL) was added dropwise to the reaction solution. The reaction was allowed to warm to room temperature and stirred overnight. Afterwards, the reaction mixture was diluted with ethyl acetate (20 mL) and the mixture was washed with aqueous hydrochloric acid (5%, 10 mL) and with aqueous sodium bicarbonate solution (saturated, 2×10 mL). The organic phase was then dried with Na_2SO_4, filtered, and concentrated to yield a yellow residue. Flash chromatography using 1:1 Hexanes/Ethyl Acetate was done to yield solid PF1 (40% yield). 1H NMR (400 MHz, DMSO-d6) 10.05 (s, 2H), 8.0 (d, 1H), 7.77 (t, 1H) 7.7 (t, 1H), 7.55 (s, 2H), 7.24 (d, 1H), 7.14 (d, 2H), 6.69 (d, 2H), 5.8 (m, 2H), 5.35 (d, 2H), 5.22 (d, 2H), 4.61 (d, 4H).

2.5.5.2 PF2. To a 100 mL round bottom flask equipped with a magnetic stir bar, was added Resorufin sodium salt (1.0 g, 4.25 mmol, 1.00 eq) and pyridine (0.69 ml, 8.50 mmol, 2.00 eq, ρ = 0.98 g/mL) and were dissolved in dry DMF (5 mL) and cooled down at 0 ^{o}C. Then, the flask was purged with nitrogen. Finally, allyl chloroformate (0.48 ml, 4.46 mmol, 1.05 eq, ρ = 1.13 g/mL) was added dropwise to the reaction solution. Afterwards, the reaction was allowed to warm to room temperature and stirred overnight. Afterwards, the reaction was diluted with ethyl acetate (50 mL) and the mixture was washed with aqueous hydrochloric acid (5%, 25 mL), aqueous sodium bicarbonate solution (saturated, 2×25 mL), and brine. The organic layer was dried with Na2SO4, filtered, and concentrated. Flash chromatography using 4:1 Hexanes/Ethyl Acetate gave solid PF2 (70% yield). 1H NMR (400 MHz, $CDCl_3$) 7.71 (d, 1H), 7.39 (d, 1H), 7.17 (d, 1H), 7.15 (d, 1H), 7.13 (d, 1H), 6.79 (d, 1H), 6.25 (d, 1H), 5.95 (m, 1H), 5.4 (d, 1H), 5.3 (d, 1H), 4.7 (d, 2H).

2.5.5.3 Pro-Dox. Doxorubicin (10 mg, 18.1 μmol, 1.00 eq) and triethylamine (5.75 μL, 40.9 μmol, 4.00 eq) were dissolved in dry DMF (1 mL) and cooled down at 0^{o} C. Then allyl chloroformate (19.2 μL, 18.1 μmol, 1.00 eq, ρ = 1.13 g/mL) was dropwise mixed with previous solution. The resulting mixture was allowed to warm to room temperature overnight. After 14 h it was diluted with ethyl acetate (25 mL) and the mixture was washed with aqueous hydrochloric acid (5%, 10 mL) and with aqueous sodium bicarbonate solution (saturated, 2×10 mL). The organic layer was dried with Na_2SO_4, filtered, and concentrated to yield a dark residue. Flash chromatography using 1:1 Hexanes/Ethyl Acetate gave Pro-Dox as a dark solid (69 % yield). 1H NMR (400 MHz, $CDCl_3$) δ = 13.96 (s, 1H), 13.22 (s, 1H), 8.02 (d, 1H), 7.77 (t, 1H), 7.37 (d, 1H), 5.71 (m, 1H), 5.49 (d, 3.9, 1H), 5.28 (s, 1H), 5.16 (d, 1H), 4.94 (m, 2H), 4.74 (m, 2H), 4.50 (s, 1H), 4.12 (q, 1H), 4.06 (s, 3H), 3.76 (d, 2H), 3.65 (d, 1H), 3.26 (m, 1H), 3.02 - 2.96 (m, 2H), 2.41 (s, 1H), 2.31 (d, 1H), 2.15 (m, 1H), 1.87 (m, 2H), 1.75 (m, 1H), 1.27 (d, 3H).

2.5.5.4 Quantification of catalyst per AuNP using ICP-MS characterization. ICP-MS analyses were performed on a Perkin-Elmer NexION 300X ICP mass spectrometer to quantify

197Au and 101Ru. Operating conditions were as follows: nebulizer flow rate: 0.95 L/min; rf power: 1600 W; plasma Ar flow rate: 18 L/min; dwell time: 50 ms. A series of solutions with gold and ruthenium (concentration: 0, 0.2, 0.5, 1, 2, 5, 10, and 20 ppb) were prepared for drawing the calibration curve. Nanozyme solutions were diluted in water to 200 nM. 10 μL sample solution was transferred to 15 mL centrifuge tubes. 0.5 mL of fresh aqua regia was added to each sample including the standard samples and was diluted to 10 mL with DI water.

Table 2.2. Gold (Au) and ruthenium (Ru) amount in the nanozymes using ICP-MS measurement. The Ru/AuNP represents number of catalysts encapsulated per AuNP.

	Au(ng)	Ru(ng)	Ru(ng)/AuNP(pmol)	Ru/AuNP
Pos-NZ	228.5	10.0	2.3	28.9
	232.6	9.9	2.7	
	231.0	11.1	2.4	
Zw-NZ	229.5	10.8	2.2	24.2
	231.3	11.7	2.5	
	231.8	12.2	2.7	

2.5.6 Nanozyme kinetics in solution. Allylcarbamate protected rhodamine 110 (PF1, green) and allylcarbonate protected resorufin (PF2, red) were used as substrates to test the catalytic activity of Pos-NZ and Zw-NZ. A solution containing 400 nM nanozyme and 1 μM substrate was prepared in a 96-well plate. 1 μM substrate solutions alone were used as negative controls. The kinetic study was done by tracking the fluorescence intensity of PF1 (λ_{ex} = 488 nm, λ_{em} = 521 nm) and PF2 (λ_{ex} = 543 nm, λ_{em} = 590 nm) using a Molecular Devices SpectraMax M2 microplate reader for 72 h.

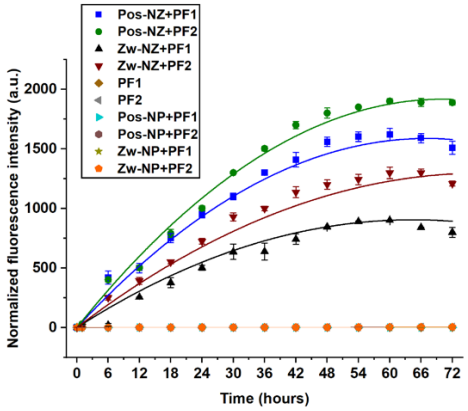

Figure 2.10. Normalized fluorescence intensity (fluorescence at time t divided by the initial fluorescence intensity) of pro-fluorophores PF1 and PF2 (1 μM) by nanozymes (400 nM). Activity of Pos-NZ (blue and green) and Zw-NZ (black and red) were determined in sodium phosphate buffer (5 mM, pH 7.4) for 72 h. Activation of PF1 and PF2 by nanoparticles (Pos-NPs and Zw-NPs) were used as controls. The data are average of triplicates and the error bars indicate standard deviations.

Fluorophore conversion rate was calculated using the calibration curve slope of Rhodamine 110 (1900 a.u./μM) for PF1 and Resorufin (4125 a.u./μM) for PF2.

Table 2.3. Fluorophore conversion rate per μM of nanozyme for PF1 and PF2.

Nanozyme	**PF1 conversion rate x 10^{-3} (μM.S^{-1})**
Pos-NZ	2.5 ± 0.2
Zw-NZ	0.9 ± 0.2
Nanozyme	**PF2 conversion rate x 10^{-3} (μM.S^{-1})**
Pos-NZ	2.2 ± 0.2
Zw-NZ	0.9 ± 0.2

2.5.7 *In-vitro* stability of nanozymes in serum containing media. HeLa cells were seeded at 20,000 in 0.2 ml per well in 96-well plates 24 h before the experiment. Next day, the cells were washed with PBS and incubated with Pos-NZ and Zw-NZ (100, 200 and 400 nM) in 10% serum-containing media for 24 h, 48 h and 72 h at 37 °C. Subsequently, the cells were washed with PBS

(3 times) and then subjected to lysis buffer. The lysed cells were then further processed for ICP-MS analysis. Each experiment was comprised of 3 replicates.

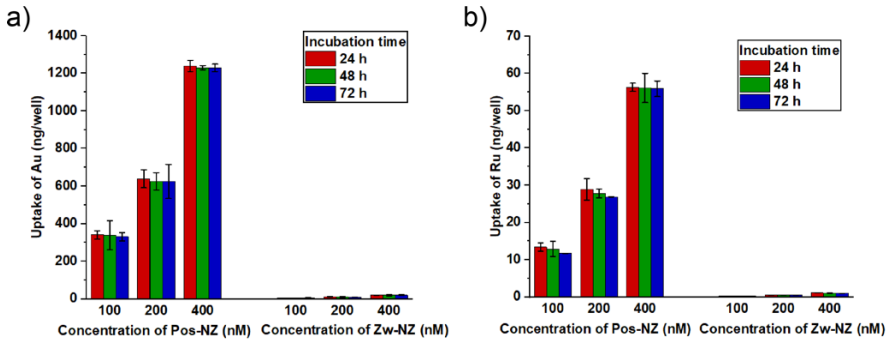

Figure 2.11. Cellular uptake of a) Au (ng/well) and b) Ru (ng/well) in HeLa (20,000 cells/well) after 24 h, 48 h and 72 h incubation with Pos-NZ and Zw-NZ with increasing concentration. The data are average of triplicates and the error bars indicate standard deviations.

Next, the catalytic activity of the nanozymes through profluorophore activation was assessed using confocal microscopy upto 72 h (3 days). HeLa cells were seeded at 200k in 2 mL 10% serum-containing media in the confocal dish and treated with Pos-NZ (200 nM). After 24 h, 48 h and 72 h incubation with Pos-NZ, cells were washed by PBS buffer three times and old media was replaced by PF1 (100 μM). After 24 h incubation with PF1, confocal imaging was obtained on Nikon A1 spectral detector confocal microscope (A1SP) using 60x objective. The settings of the confocal microscope were as follows (unless otherwise specified): green channel, λ_{ex} = 488 nm and λ_{em} = BP 505-530 nm. Emission filters: BP, band pass; LP, high pass.

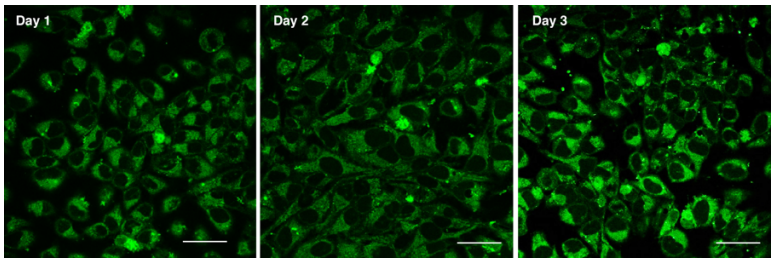

Figure 2.12. Confocal images of activation of PF1 in HeLa cells after 24, 48 and 72 h incubation of Pos-NZ. The scale bars are 25 μm.

2.5.8 Confocal imaging experiments to visualize intra-extracellular catalysis on mammalian cells. HeLa and RAW 264.7 cells were grown in cell culture flasks using Dulbecco's

modified Eagle medium with 10% fetal bovine serum, at 37 °C in a humidified atmosphere of 5% CO_2. For confocal analysis, HeLa and RAW 264.7 cells were seeded at 200k in 2 mL 10% serum-containing media in the confocal dish 24 h before the experiment. During the experiment, cells were washed by PBS buffer three times and old media was replaced by substrate PF1 (100 μM) in serum-containing media, and the cells were incubated for 24 h followed by washing with PBS buffer three times. The Pos-NZs (200 nM) and Hoechst nuclear stain were then added to the cells and incubated for 0.5 h. The cells were washed with PBS three times to remove excess Pos-NZ. Then PBS with a mixture of Zw-NZs (200 nM) and PF2 (100 □M) was added to the washed cells. Confocal microscopy images were obtained after 0.5 h on Nikon A1 spectral detector confocal microscope (A1SP) using 60x objective. The settings of the confocal microscope were as follows (unless otherwise specified): green channel, λ_{ex} = 488 nm and λ_{em} = BP 505-530 nm; red channel, λ_{ex} = 543 nm and λ_{em} = LP 590 nm. Emission filters: BP, band pass; LP, high pass.

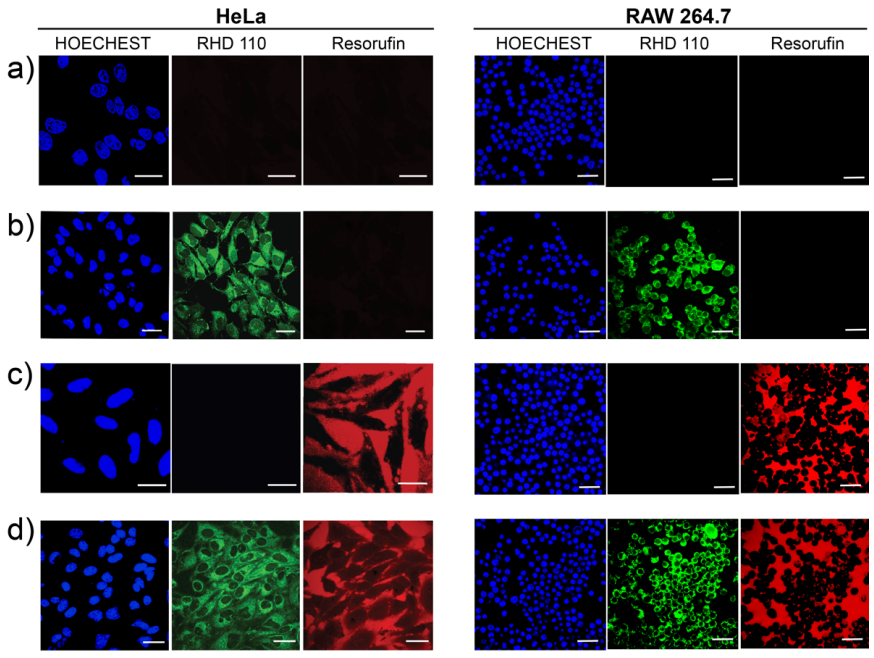

Figure 2.13. Confocal images of HeLa cells and macrophage cells (RAW 264.7) a) incubated with PF1 and PF2 in absence of nanozymes indicating that no fluorescence is observed in presence of the pro-fluorophore alone, b) intracellular activation of rhodamine derivative (RHD 110) by Pos-NZ, c) extracellular activation of resorufin derivative by Zw-NZ, d) simultaneous intra and extracellular activation in presence of Pos-NZ and Zw-NZ respectively. Nuclei were stained by Hoechst 33342. The scale bars are 25 μm.

2.5.9 Intra-extracellular imaging independent of the order of incubation of nanozyme and profluorophore. HeLa cells were seeded at 200k in 2 mL 10% serum-containing media in the confocal dish 24 h before the experiment. During the experiment, old media was replaced by Pos-NZ (200 nM) in serum-containing media, and the cells were incubated for 0.5 h followed by washing with PBS buffer three times to remove the excess Pos-NZ. The PF1 (100 μM) was then added to the cells and incubated for 24 h. The cells were washed with PBS three times. Then, a mixture of Zw-NZs (200 nM) and PF2 (100 μM) in PBS and Hoechst nuclear stain was added to the cells. Confocal microscopy images were obtained after 0.5 h on Nikon A1 spectral detector confocal microscope (A1SP) using 60x objective. The settings of the confocal microscope were as follows (unless otherwise specified): green channel, λ_{ex} = 488 nm and λ_{em} = BP 505-530 nm; red channel, λ_{ex} = 561 nm and λ_{em} = LP 590 nm. Emission filters: BP, band pass; LP, high pass.

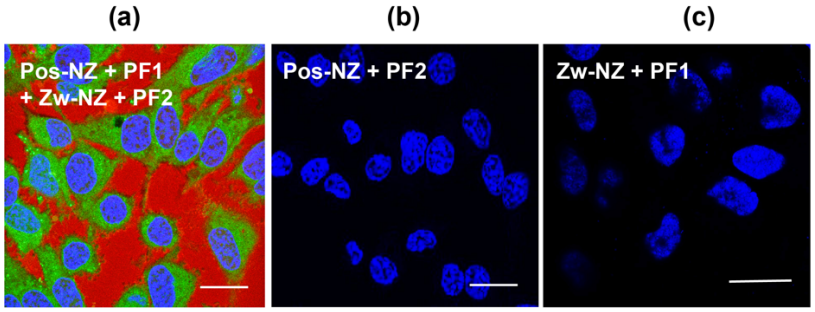

Figure 2.14. Confocal images of HeLa cells a) intra-extracellular fluorescence after altering the order of incubation, as additional controls HeLa cells were b) incubated with Pos-NZ followed by PF2, and c) incubated with Zw-NZ and PF1. Nuclei were stained by Hoechst 33342. The scale bars are 25 μm.

2.5.10 Cytotoxicity measurements of Pro-Dox and free Dox. HeLa cells were seeded at 10,000 in 0.2 mL per well in 96-well plates 24 h before the experiment. Cells were washed with PBS buffer and then treated with 10 different concentrations ranging from 10 nM to 20 μM of free Dox and pro-Dox in triplicate. After 24 h of incubation, the cells were then completely washed off with PBS buffer three times, and 10% alamar Blue in serum-containing media was added to each well (220 μl) and further incubated at 37 °C for 2.5 h. Cell viability was then determined by

measuring the fluorescence intensity at 570 nm using a SpectraMax M5 microplate spectrophotometer.

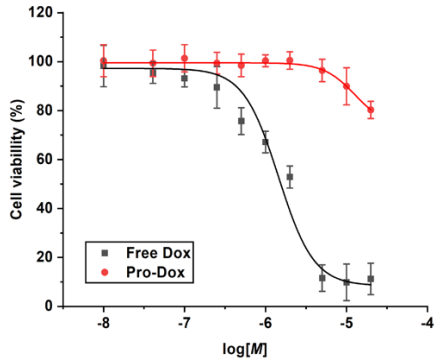

Figure 2.15. Viability of cells treated with free-Dox and pro-Dox at various concentrations, showing a nice therapeutic window between the two.

2.5.11 Intracellular therapeutic activation independent of the order of incubation of nanozyme and prodrug. HeLa cells were seeded at 10k in 0.2 mL per well in 96-well plates 24 h before the experiment. Cells were washed off and incubated with Pro-Dox at a concentration of 0.5, 1, 2, and 4 μM. After 24 h, cells were washed with PBS buffer three times and treated with Pos-NZ (100 nM) and Pos-NP (100 nM) in 10% serum-containing media for 24 h. The cells were then completely washed off and 10% alamar blue in serum-containing media was added to each well (220 μL) and incubated further at 37°C for 2 h. Cell viability was then determined by measuring the fluorescence intensity at 570 nm using a SpectraMax M5 microplate spectrophotometer.

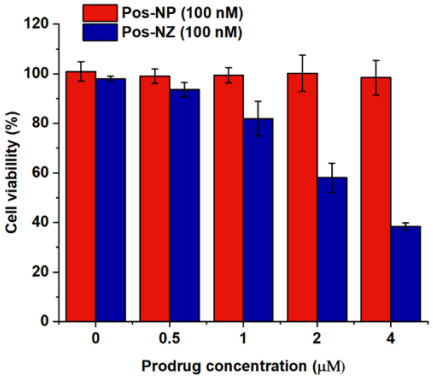

Figure 2.16. Cell viability after altering the order of incubation of Pos-NZ and pro-Dox. Cells treated with Pos-NPs and pro-Dox was used as an additional control. The data are average of triplicates and the error bars indicate standard deviations.

2.5.12 Absorbance spectra of free Dox. We studied the absorbance spectra of Dox at the maximum concentration used in the experiment (4 μM) using a UV-VIS reader. We observed maximum absorbance at 490 nm, but no signal was observed at 570 nm.[46]

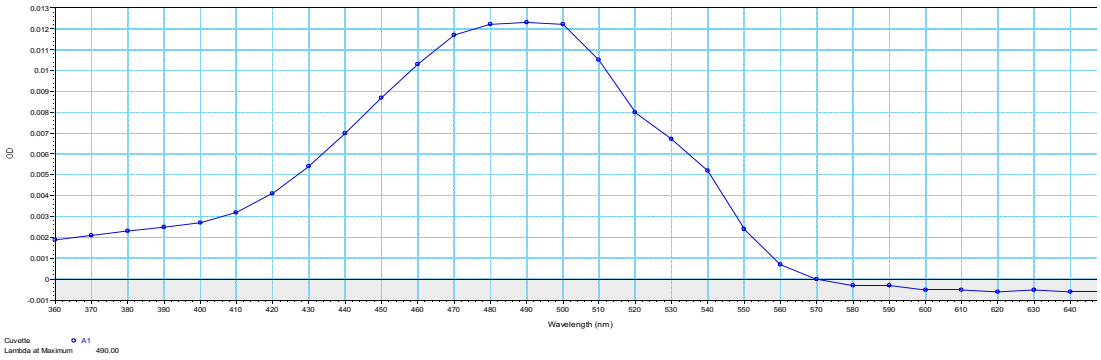

Figure 2.17. Absorbance spectrum of Dox (4 μM) in sodium phosphate buffer (5 mM, pH 7.4).

2.6 References

1. Ngo, J. T.; Adams, S. R.; Deerinck, T. J.; Boassa, D.; Rodriguez-Rivera, F.; Palida, S. F.; Bertozzi, C. R.; Ellisman, M. H.; Tsien, R. Y. Click-EM for Imaging Metabolically Tagged Nonprotein Biomolecules. *Nat. Chem. Biol.* **2016**, *12*, 1–10.

2. Bertozzi, C. R. A Decade of Bioorthogonal Chemistry. *Acc. Chem. Res*. **2011**, *44,* 651–653.

3. Sletten, E. M.; Bertozzi, C. R. Bioorthogonal Chemistry: Fishing for Selectivity in a Sea of Functionality. *Angew. Chem. Int. Ed.* **2009**, *48*, 6974–6998.

4 .Agarwal, P.; Bertozzi, C. R. Site-Specific Antibody–Drug Conjugates: The Nexus of Bioorthogonal Chemistry, Protein Engineering, and Drug Development. *Bioconjug. Chem.* **2015**, *26*, 176–192.

5. Matikonda, S. S.; Fairhall, J. M.; Fiedler, F.; Sanhajariya, S.; Tucker, R. A. J.; Hook, S.; Garden, A. L.; Gamble, A. B. Mechanistic Evaluation of Bioorthogonal Decaging with Trans-Cyclooctene: the Effect of Fluorine Substituents on Aryl Azide Reactivity and Decaging from the 1,2,3-Triazoline. *Bioconjug. Chem.* **2018,** *29,* 324-334.

6. Völker, T.; Meggers, E. Transition-Metal-Mediated Uncaging in Living Human Cells-an Emerging Alternative to Photolabile Protecting Groups. *Curr. Opin. Chem. Biol.* **2015,** *25*, 48–54.

7. Völker, T.; Dempwolff, F.; Graumann, P. L.; Meggers, E. Progress Towards Bioorthogonal Catalysis with Organometallic Compounds. *Angew. Chem. Int. Ed. Engl.* **2014**, *53*, 10536–10540.

8. Völker, T.; Meggers, E. Chemical Activation in Blood Serum and Human Cell Culture: Improved Ruthenium Complex for Catalytic Uncaging of Alloc-Protected Amines. *ChemBioChem.* **2017**, *18,* 1083–1086.

9. Zheng, Y.; Tan, Y.; Harms, K.; Marsch, M.; Riedel, R.; Zhang, L.; Meggers, E. Octahedral Ruthenium Complex with Exclusive Metal-Centered Chirality for Highly Effective Asymmetric Catalysis. *J. Am. Chem. Soc.* **2017**, *139*, 4322-4325.

10. Li, J.; Yu, J.; Zhao, J.; Wang, J.; Zheng, S.; Lin, S.; Chen, L.; Yang, M.; Jia, S.; Zhang, X.; Chen, P. Palladium-Triggered Deprotection Chemistry for Protein Activation in Living Cells. *Nat. Chem.* **2014,** *6*, 352-361.

11. Yang, M.; Li, J.; Chen, P. R. Transition Metal-Mediated Bioorthogonal Protein Chemistry in Living Cells. *Chem. Soc. Rev*. **2014**, *43*, 6511–6526.

12. Jeschek, M.; Reuter, R.; Heinisch, T.; Trindler, C.; Klehr, J.; Panke, S.; Ward, T. R. Directed Evolution of Artificial Metalloenzymes for *In Vivo* Metathesis. *Nature* **2016,** *537*, 661–665.

13. Han, H. K.; Amidon, G. L. Targeted Prodrug Design to Optimize Drug Delivery. *AAPS PharmSci.* **2000**, *2*, 48-58.

14. Clavadetscher, J.; Indrigo, E.; Chankeshwara, S. V; Lilienkampf, A.; Bradley, M. In-Cell Dual Drug Synthesis by Cancer-Targeting Palladium Catalysts. *Angew. Chem.* **2017**, *129*, 6968–6972.

15. Kim, C. S.; Duncan, B.; Creran, B.; Rotello, V. M. Triggered Nanoparticles as Therapeutics. *Nano Today*, **2013**, *8*, 439–447.

16. Yusop, R. M.; Unciti-Broceta, A.; Johansson, E. M.; Sanchez-Martin, R. M.; Bradley, M. Palladium-Mediated Intracellular Chemistry. *Nat. Chem.* **2011**, *3*, 239–243.

17. Tonga, G. Y.; Jeong, Y.; Duncan, B.; Mizuhara, T.; Mout, R.; Das, R.; Kim, S. T.; Yeh, Y.-C.; Yan, B.; Hou, S.; Rotello, V. M. Supramolecular Regulation of Bioorthogonal Catalysis in Cells Using Nanoparticle-Embedded Transition Metal Catalysts. *Nat. Chem.* **2015**, *7*, 597–603.

18. Okamoto, Y.; Kojima, R.; Schwizer, F.; Bartolami, E.; Heinisch, T.; Matile, S.; Fussenegger, M.; Ward, T. R. A Cell-Penetrating Artificial Metalloenzyme Regulates a Gene Switch in a Designer Mammalian Cell. *Nat. Commun.* **2018**, *9*, 1–7.

19. Hu, Z.; Jiang, X.; Albright, C. F.; Graciani, N.; Yue, E.; Zhang, M.; Zhang, S. Y.; Bruckner, R.; Diamond, M.; Dowling, R.; Rafalski, M.; Yeleswaram, S.; Trainor, G. L.; Seitz, S. P.; Han, W. Discovery of Matrix Metalloproteases Selective and Activated Peptide-Doxorubicin Prodrugs as Anti-Tumor Agents. *Bioorganic Med. Chem. Lett.* **2010**, *20*, 853–856.

20. Miyawaki, A.; Sawano, A.; Kogure, T. Lighting Up Cells: Labelling Proteins with Fluorophores. *Nat. Cell. Biol.* **2003**, *5,* 1–7.

21. Albright, C. F.; Graciani, N.; Han, W.; Yue, E.; Stein, R.; Lai, Z.; Diamond, M.; Dowling, R.; Grimminger, L.; Zhang, S.-Y.; Behrens, D.; Musselman, A, Bruckner, R.; Zhang, M.; Jiang, X.; Hu, D.; Higley, A.; Dimeo, S.; Rafalski, M.; Mandlekar, S.; *et al.* Matrix Metalloproteinase-Activated Doxorubicin Prodrugs Inhibit HT1080 Xenograft Growth Better than Doxorubicin with Less Toxicity. *Mol. Cancer Ther.* **2005,** *4*, 751–760.

22. de Graaf, M.; Boven, E.; Scheeren, H. W.; Haisma, H. J.; Pinedo, H. M. Beta-Glucuronidase-Mediated Drug Release. *Curr. Pharm. Des.* **2002**, *8*, 1391–1403.

23. Lang, K.; Davis, L.; Wallace, S.; Mahesh, M.; Cox, D. J.; Blackman, M. L.; Fox, J. M.; Chin, J. W. Genetic Encoding of Bicyclononynes and Trans-Cyclooctenes for Site-Specific Protein Labeling *In Vitro* and in Live Mammalian Cells *via* Rapid Fluorogenic Diels-Alder Reactions. *J. Am. Chem. Soc.* **2012**, *134*, 10317–10320.

24. Denmeade, S. R.; Mhaka, A. M.; Rosen, D. M.; Brennen, W. N.; Dalrymple, S.; Dach, I.; Olesen, C.; Gurel, B.; DeMarzo, A. M.; Wilding, G.; Carducci, M. A.; Dionne, C. A.; Møller, J. V.; Nissen, P.; Christensen, S. B.; Isaacs, J. T. Engineering a Prostate-Specific Membrane Antigen–Activated Tumor Endothelial Cell Prodrug for Cancer Therapy. *Sci. Transl. Med.* **2012**, *4*, 1-14.

25. Weiss, J. T.; Dawson, J. C.; Macleod, K. G.; Rybski, W.; Fraser, C.; Torres-Sánchez, C.; Patton, E. E.; Bradley, M.; Carragher, N. O.; Unciti-Broceta, A. Extracellular Palladium-Catalysed Dealkylation of 5-Fluoro-1-Propargyl-Uracil as a Bioorthogonally Activated Prodrug Approach. *Nat. Commun.* **2014**, *5*, 3277-3285.

26. Jeong, Y.; Tonga, G. Y.; Duncan, B.; Yan, B.; Das, R.; Sahub, C.; Rotello, V. M. Solubilization of Hydrophobic Catalysts Using Nanoparticle Hosts. *Small* **2018**, *14*, 1-5.

27. Slowing I, Trewyn BG, Lin VSY. Effect of Surface Functionalization of MCM-41-type Mesoporous Silica Nanoparticles on the Endocytosis by Human Cancer Cells. *J. Am. Chem. Soc.* **2006**, *128*, 14792–93.

28. Jiang, Y.; Huo, S.; Mizuhara, T.; Das, R.; Lee, Y.-W.; Hou, S.; Moyano, D. F.; Duncan, B.; Liang, X. J.; Rotello V. M. The Interplay of Size and Surface Functionality on the Cellular Uptake of Sub-10 nm Gold Nanoparticles. *ACS Nano*. **2015**, *9*, 9986–9993.

29. Verma, A.; Stellacci, F. Effect of Surface Properties on Nanoparticle-Cell Interactions. *Small* **2010**, *6*, 12–21.

30. Gupta, A.; Das, R.; Yesilbag Tonga, G.; Mizuhara, T.; Rotello, V. M. Charge-Switchable Nanozymes for Bioorthogonal Imaging of Biofilm-Associated Infections. *ACS Nano.* **2017**, *12*, 89-94.

31. Albanese, A.; Tang, P. S.; Chan, W. C. W. The Effect of Nanoparticle Size, Shape, and Surface Chemistry on Biological Systems. *Annu. Rev. Biomed. Eng.* **2012**, *14*, 1–16.

32. Hong, R.; Fischer, N. O.; Verma, A.; Goodman, C. M.; Emrick, T.; Rotello, V. M. Control of Protein Structure and Function Through Surface Recognition by Tailored Nanoparticle Scaffolds. *J. Am. Chem. Soc.* **2004**, *126*, 734–735.

33. Ghosh, P.; Han, G.; De, M.; Kim, C. K.; Rotello, V. M. Gold Nanoparticles in Delivery Applications. *Adv. Drug Deliv. Rev.* **2008**, *60*, 1307–1315.

34. Streu, C.; Meggers, E. Ruthenium Induced Allylcarbamate Cleavage in Living Cells. *Angew. Chem.* **2006**, *118*, 5773-5776.

35. Kubin, R. F.; Fletcher, A. N. Fluorescence Quantum Yields of Some Rhodamine Dyes. *J. Lumin.* **1982**, *27*, 455–462.

36. Liu, D. S.; Nivón, L. G.; Richter, F.; Goldman, P. J.; Deerinck, T. J.; Yao, J. Z.; Richardson, D.; Phipps, W. S.; Ye, A. Z.; Ellisman, M. H.; Drennan, C. L.; Baker, D.; Ting, A. Y. Computational

Design of a Red Fluorophore Ligase for Site-Specific Protein Labeling in Living Cells. *PNAS,* **2014**, *111,* E4551-E4559.

37. Xu, W.; Kong, J. S.; Yeh, Y.-T. E.; Chen, P. Single-Molecule Nanocatalysis Reveals Heterogeneous Reaction Pathways and Catalytic Dynamics. *Nat. Mater.* **2008**, *7*, 992–996.

38. Topete, A.; Alatorre-Meda, M.; Villar-Alvarez, E. M.; Carregal-Romero, S.; Barbosa, S.; Parak, W. J.; Taboada, P.; Mosquera, V. Polymeric-Gold Nanohybrids for Combined Imaging and Cancer Therapy. *Adv. Healthc. Mater.* **2014**, *3*, 1309–1325.

39. Liao, W.-C.; Sohn, Y. S.; Riutin, M.; Cecconello, A.; Parak, W. J.; Nechushtai, R.; Willner, I. Drug Delivery: The Application of Stimuli-Responsive VEGF- and ATP-Aptamer-Based Microcapsules for the Controlled Release of an Anticancer Drug, and the Selective Targeted Cytotoxicity toward Cancer Cells. *Adv. Funct. Mater.* **2016**, *26*, 4423-4432.

40. Tacar, O.; Sriamornsak, P.; Dass, C. R. Doxorubicin: An Update on Anticancer Molecular Action. *J. Pharm. Pharmacol*. **2013**, *65,* 157–170.

41. Liao, L.; Liu, J.; Dreaden, E. C.; Morton, S. W.; Shopsowitz, K. E.; Hammond, P. T.; Johnson, J. A. A Convergent Synthetic Platform for Single-Nanoparticle Combination Cancer Therapy: Ratiometric Loading and Controlled Release of Cisplatin, Doxorubicin, and Camptothecin. *J. Am. Chem. Soc*. **2014**, *136,* 11–14.

42. M. Brust, M. Walker, D. Bethell, D. J. Schiffrin, R. Whyman, *J. Chem. Soc. Chem. Commun.* **1994**, 801.

43. M. J. Hostetler, A. C. Templeton, R. W. Murray, *Langmuir* **1999**, *15*, 3782.

44. Völker, T.; Dempwolff, F.; Graumann, P. L.; Meggers, E. Progress Towards Bioorthogonal Catalysis with Organometallic Compounds. *Angew. Chem. Int. Ed. Engl.* **2014**, *53*, 10536–10540.

45. Liu, D. S.; Nivón, L. G.; Richter, F.; Goldman, P. J.; Deerinck, T. J.; Yao, J. Z.; Richardson, D.; Phipps, W. S.; Ye, A. Z.; Ellisman, M. H.; Drennan, C. L.; Baker, D.; Ting, A. Y. Computational Design of a Red Fluorophore Ligase for Site-Specific Protein Labeling in Living Cells. *PNAS,* **2014**, *111,* E4551-E4559.

46. Bray, T. L.; Salji, M.; Brombin, A.; Pérez-López, A. M.; Rubio-Ruiz, B.; Galbraith, L. C. A.; Patton, E. E.; Leung, H. Y.; Unciti-Broceta, A. Bright Insights into Palladium-Triggered Local Chemotherapy. *Chem. Sci.* **2018**, *10*, 1-8.

CHAPTER 3

MACROPHAGE-ENCAPSULATED BIOORTHOGONAL NANOZYMES: TOOLS FOR TARGETED CANCER THERAPY

3.1 Introduction

Targeted drug delivery has emerged as a prominent strategy for avoiding widespread toxicity typically associated with conventional cancer chemotherapies. The successful application of targeting has been shown to result in improved survival time and patient quality of life.[1-3] Macrophages are innate immune cells that are inherently attracted to specific tissue environments, including hypoxic, ischemic, and necrotic areas associated with tumors and their cores.[4-6] Concurrently, many cancers secrete macrophage chemoattractants, whose gradients the cells migrate across, resulting in active recruitment to cancerous regions.[7,8] This characteristic makes macrophages particularly attractive as cell-based delivery vehicles for accessing solid tumors, which are normally difficult to reach by using conventional targeting strategies.[9,10]

Previous approaches have utilized macrophages loaded with nanoparticle-drug conjugates or free drugs for anti-cancer therapeutic delivery.[11,12] In several cases, the cell-mediated delivery resulted in greater efficacy than free materials, and reduced off-target toxicity.[13,14] However, the direct loading approach is hindered by the ceiling for amount of loadable payload and lack of controlled release. Cells are limited in the amount of drug they can carry, and there are no means to regulate the rate, extent, and site of discharge. The loaded cytotoxic drugs can also affect or kill the carrier cell prior to reaching the desired target site. To a certain extent, these issues can be addressed by utilizing macrophages bearing stimuli-responsive nanoparticles, which control the release of therapeutics.[15,16] In these approaches, external stimuli such as thermal energy, light, or ultrasound can be used to trigger nanoparticles' release of drug molecules, specifically at the tumor site. While this type of strategy is promising, limited therapeutic loading remains a hurdle. Also, efficiency is affected by tissue penetration depth of stimuli, and localized damage to the

surrounding healthy tissues is a concern. Thus, an alternative means is needed to make macrophage-mediated drug delivery clinically successful.

Bioorthogonal catalysis[17,18] has the potential to overcome limitations associated with payload loading of and release from macrophages and other cell-based delivery agents. Internalized catalysts can be transported by cells to the desired tissue/organ, where they continuously generate active therapeutics from inactive prodrugs at the targeted location. Prodrugs are protected drug molecules that remain nontoxic until activated by a stimulus.[19,20] In our study, we engineered macrophages as a delivery vehicle for transition metal catalyst (TMC)-bearing gold nanoparticles (AuNPs), or nanozymes (NZs). These catalysts, which are embedded in the AuNPs, can activate a profluorophore/prodrug via bioorthogonal cleavage reaction in the cellular environment, as reported in previous studies.[21-24] Here, following encapsulation into macrophages, minimal nanozyme release from the cells was observed, even after a prolonged incubation period. We tested the efficacy of engineered macrophages (RAW_NZ) in a co-culture model with HeLa (human cervical cancer) cells. Significant cancer cell toxicity was achieved in the presence of nanozyme-bearing macrophages, even at the lowest concentration of the prodrug administered. In addition to cancer cell killing abilities, it is important to retain the macrophages' chemotactic properties following nanozyme internalization, which is critical for the engineered cells to reach the targeted tumor site. For this reason, we assessed the migratory behavior of engineered versus non-modified macrophages towards the Colony Stimulating Factor-1 (CSF) chemoattractant.[25] In chemotaxis assays, both cell populations exhibited similar behaviors. Our strategy here combines the targeting ability of cell-based drug delivery with bio-orthogonal activation of a chemotherapeutic prodrug, providing a new approach for next-generation drug delivery system.

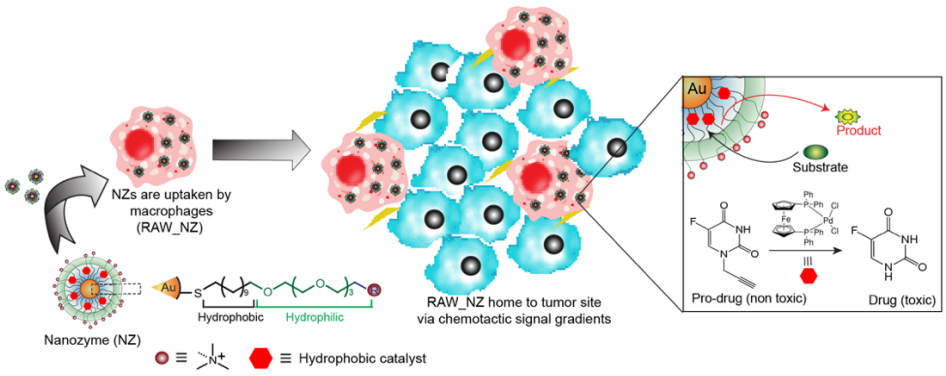

Figure 3.1. Schematic representation of macrophage mediated delivery of bioorthogonal nanozymes (NZs) for prodrug activation selectively at tumor cells.

3.2 Results and discussion

In this study, we designed 2 nm AuNPs functionalized with a ligand containing a cationic terminal group (TTMA) to facilitate a high degree of uptake by the negatively charged cell membrane.[26-29] The AuNP ligand monolayer contains a crucial hydrophobic alkane chain for catalyst encapsulation and a tetra(ethylene glycol) spacer to provide biocompatibility (Figure 3.1). These particles were synthesized from pentane-thiol capped 2 nm core AuNPs using a place exchange reaction (synthesis and characterization of NPs is described in supporting information, Figures 3.S1, 3.S2).[30] Nanozymes were generated by immobilizing hydrophobic palladium TMC (1,1′ bis(diphenylphosphino) ferrocene)palladium(II)dichloride[31-33] in the hydrophobic portion of AuNP monolayer.[21] The catalyst was dissolved in acetone and added into an aqueous solution of AuNPs in a 1:1 ratio by volume. Acetone was evaporated slowly and any excess catalyst was filtered away to provide the desired nanozyme (details of nanozyme preparation and characterization are in supporting information). There was no aggregation observed before or after encapsulation of TMCs, as confirmed by dynamic light scattering (DLS) (Table 3.S1 and Figure 3.S3) and transmission electron microscopy (TEM) (Figure 3.S4). Quantification by inductively coupled plasma mass spectrometry (ICP-MS) (Table 3.S2) indicated that on average, 37 ± 1 catalysts were present per AuNP in the NZs.

NZs were internalized by macrophages (RAW 264.7) *in vitro* to generate RAW_NZ (Figure 3.1) (details in supporting information). The quantification by ICP-MS showed that both Au (Figure 3.2a) and Pd (Figure 3.2b) content increased concommittantly with NZ concentration. We also assessed the amounts of Au and Pd in macrophages following prolonged incubation periods of 48 h and 72 h. These results were similar to the those observed for the 24 h incubation time (Figure 3.2), establishing the long term retention of NZs inside macrophages.

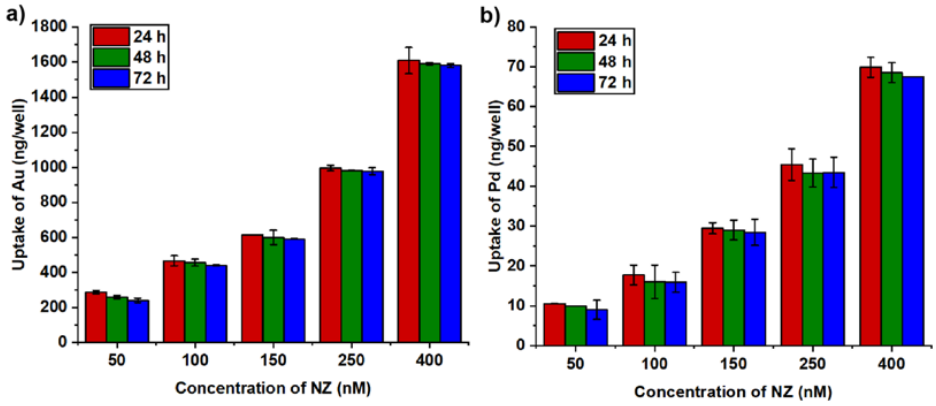

Figure 3.2. Cellular uptake of a) Au (ng/well) and b) Pd (ng/well) in macrophages (RAW 264.7 at 20,000 cells/well) after 24 h, 48 h and 72 h incubation with NZs with increasing concentration. The data shown are averages of triplicates; error bars indicate standard deviations.

We next investigated the effects of nanozyme internalization on macrophage responses to chemotactic signals, which are critical to their employment for tumor targeting.[9a] Colony Stimulating Factor-1 (CSF-1) was used as the chemoattractant, and migration was evaluated by transwell membrane assay (Figure 3.3). We compared the ability of macrophages with NZ (RAW_NZ) and without NZ (RAW 264.7) to traffick through a membrane in response to CSF-1. To visualize and quantify the migrated cells, macrophages were stained with crystal violet at the conclusion of the experiment (detailed procedure is described in supporting information). No significant difference was observed in the behaviour of macrophages with and without NZs as observed under wide-field fluorescence microscope (Figure 3.3a) and after quantification (Figure 3.3b). Both populations responded similarly to both presence and absence of CSF-1.

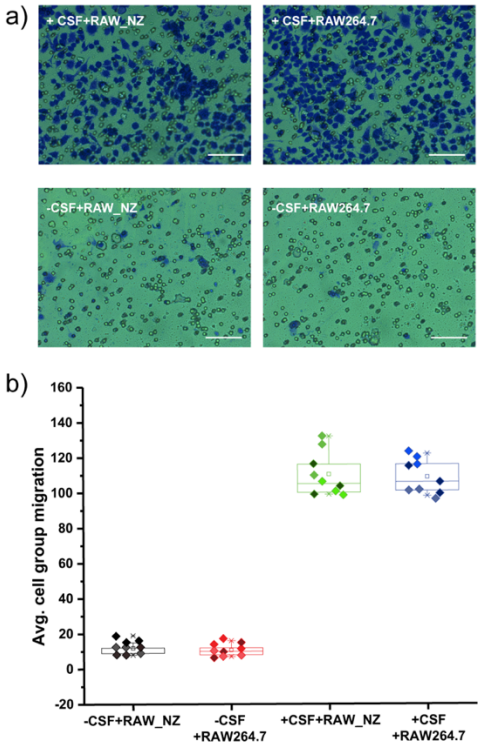

Figure 3.3. Chemotaxis capabilities are retained by RAW_NZ as determined by transwell membrane assay. a) Confocal imaging of migrated macrophages with NZs (RAW_NZ) and without NZs (RAW 264.7) in presence and absence of chemoattractant Colony-Stimulating Factor-1 (CSF-1). All cells were stained with crystal violet to facilitate detection. Scale bar = 100 μm. b) Quantification of migrated RAW 264.7 cells and RAW_NZ in presence and absence of CSF-1. Nine panels of cells were counted per treatment (n = 9, from three biological replicates, represented by differently colored diamonds). Box constitutes the interquartile range (25th to 75th percentile), the intersecting line designates the median, the small square in the center represents the mean, and the bottom and top whiskers specify the 5th and 95th percentiles, respectively.

After establishing the high stability of RAW_NZs and their ability to retain inherent chemotaxis capabilities of macrophages, we next investigated their therapeutic activation in a co-culture model with HeLa cells (Figure 3.4). For this study, propargyl protected 5-fluorouracil (pro-5FU) was chosen as a model prodrug (Figure 3.4a), due to the broad application of its active counterpart (5FU).[34,35] The caged propargyl group blocks the active site of 5FU, reducing its cytotoxicity before activation by the NZs (Figure 3.S5). For the co-culture experiment, RAW_NZ cells were seeded on a glass slide, which was then immersed in a well seeded with HeLa cells (Figure 3.4b). The co-incubated cell lines were incubated with prodrug at different concentrations, of up to 1 mM for 24 hours. In order to differentiate the viability of the cells by type, the glass

slide with RAW_NZ was removed before performing alamar blue assay separately on HeLa cells and macrophages (the detailed experimental procedure is provided in supporting information). In the presence of RAW_NZ, the viability of both HeLa (Figure 3.4c) and RAW 264.7 (Figure 3.S6) cells was substantially reduced with increasing concentrations of prodrug, indicating successful therapeutic activation by NZ. HeLa cells that received increasing concentrations of prodrug, but were not co-cultured with RAW_NZ did not show any reduction in cell viability, indicating successful protection of the active site of 5FU (Figure 3.4c). The same trend was mirrored in the case of RAW 264.7 cells that were not modified with NZs (Figure 3.S6). Our findings illustrate that the prodrug activation occurred only in the presence of NZs, not with macrophages alone. While diminished viability of RAW 264.7 cells was observed, this only occurred in treatments where NZ and prodrug were both present. In therapeutic settings, carrier cell death is not an issue so long as it occurs after the target tissue has been reached. Both HeLa (Figure 3.4) and RAW 264.7 (Figure 3.S6) cells were treated with 5FU as a positive control.

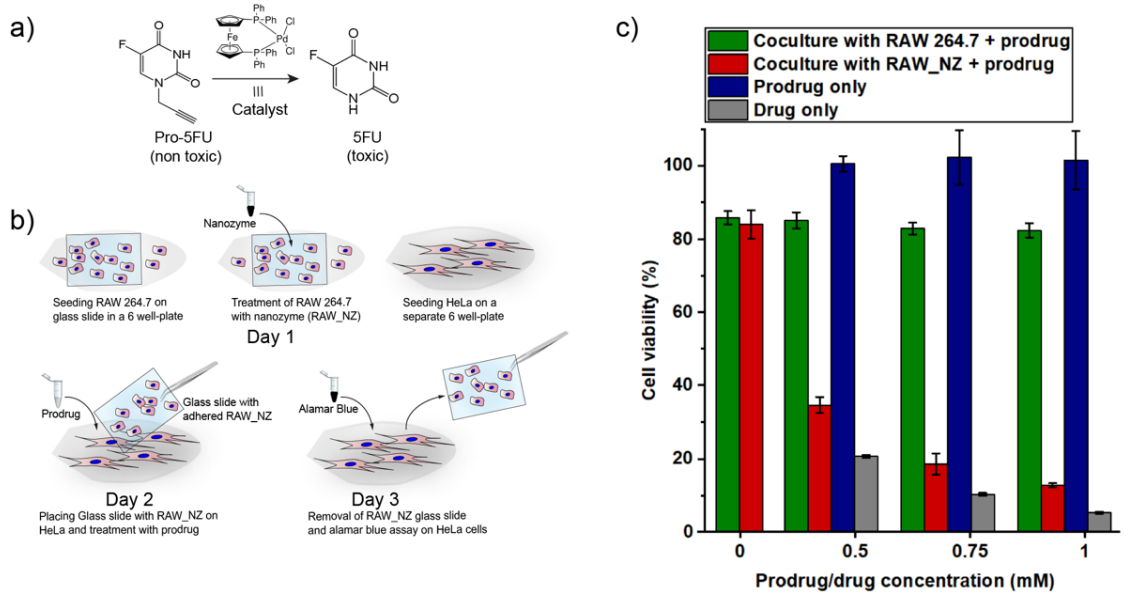

Figure 3.4. a) Pro-5FU activation by RAW_NZ. B) Graphical scheme of co-culture experiment to evaluate therapeutic efficacy of RAW_NZ in HeLa cells. c) Viability of HeLa cells after pro-5FU (prodrug) activation by RAW_NZ in the co-culture experiment. The data are average of triplicates and the error bars indicate standard deviations.

In order to expand upon these findings, we determined the effects of the RAW_NZ/Pro-5FU treatments *in situ*. Here, we co-cultured RAW_NZ with green fluorescent protein (GFP) expressing HeLa cells (GFP-HeLa) and separately, U2OS cells (GFP-U2OS). The green fluorescence of both GFP-HeLa cells and GFP-U2OS cells was greatly reduced with increasing concentration of prodrug (Figure 3.S7), due to increased cytotoxicity resulting from by active drug molecules, as observed by confocal microscopy.

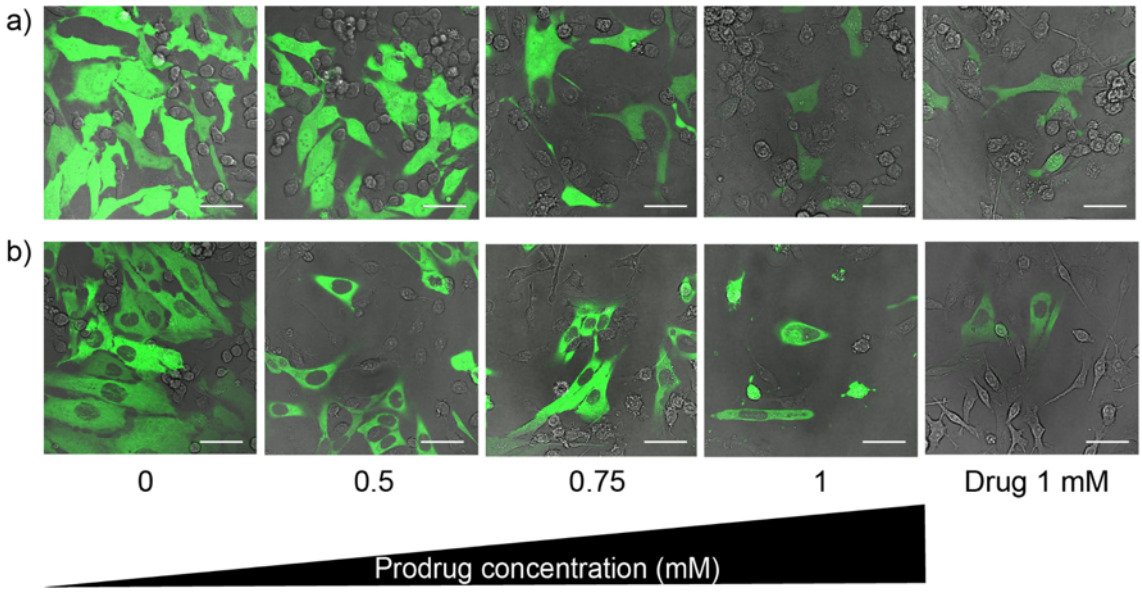

Figure 3.5. Co-culture experiment of RAW_NZ with a) GFP_HeLa cells and b) GFP_U2OS cells to demonstrate the reduction of GFP fluorescence as a result of pro-5FU activation by RAW_NZ. Scale bar = 15 μm.

3.3 Conclusions

In summary, we have developed a macrophage-mediated delivery platform for bioorthogonal nanozymes to generate therapeutic molecules at desired sites. Macrophages bearing internalized nanozymes demonstrated high therapeutic activation in a co-culture model with cancer cells. The macrophages retained the nanozymes for prolonged incubation periods and also demonstrated similar chemotactic behaviours to their non-modified counterparts, illustrating their potential for use in *in vivo* applications. By using nanozymes to activate pharmacological substrates, our system eliminates the dependence on and limitation of cellular loading.

Considering their enhanced ability for targeting, this platform holds a strong advantage against current chemotherapy and cell-based therapeutic delivery techniques. Future studies will explore the use of this platform for specific drug activation in *in vivo* models.

3.4 Experimental methods

3.4.1 Nanoparticles synthesis. 2 nm diameter gold nanoparticles were synthetized by the Brust-Schiffrin two-phase methodology[36] using pentanethiol as the stabilizer; these clusters were purified with successive extractions with ethanol and acetone. A Murray place exchange reaction[37] was carried out in dry DCM to functionalize the nanoparticles with each ligand.[38,39] The monolayer-protected nanoparticles were redispersed in water and the excesses of ligand/pentanethiol were removed by dialysis using a 10,000 MWCO snake-skin membrane. The final concentration was measured by UV spectroscopy on a Molecular Devices SpectraMax M2 at 506 nm.

3.4.2 Mammalian cell culture. All mammalian cells were grown in T75 cell culture flasks using standard growth media (DMEM supplemented with 10% FBS and 1% Pen-Strep) under physiological conditions (37 °C in a humidified atmosphere of 5% CO_2). Once the cells were at sufficient density, they were washed with phosphate-buffered saline (PBS) three times followed by 0.05% trypsinization. The trypsinized cells were centrifuged and resuspended in fresh culture media. 10 μL of cell solution was mixed with trypan blue in 1:1 volume ratio and was counted by a hemocytometer. The cell solutions were diluted in the same media to attain the desired cell concentration for subsequent experiments.

3.4.3 Preparation of engineered macrophages (RAW_NZ). Macrophages (RAW 264.7) were seeded at a concentration of 20,000 cells/well in a 24 well plate, and allowed to attach overnight. The following day, cells were washed three times with PBS to remove any dead cells. 100 nM NZ solution in macrophage growth media (described above) was added to the cells and

incubated for 24 h. After, the cells were thoroughly washed by PBS three times to remove any excess NZ to provide RAW_NZ. RAW_NZ was trypsinized depending on experiment to follow.

3.4.4 Chemotaxis/Boyden Chamber assay procedure. Cell migration towards Colony Stimulating Factor 1 (CSF-1) was investigated by a Boyden Chamber Assay following a previously described protocol.[40,41] Briefly, a transwell membrane with 8 μm pore size was coated with 10 μg/mL fibronectin. After 4 hours, the excess fibronectin was rinsed with PBS and left to dry for overnight. The next day, designated wells of a 24 well plate received 650 μL serum-free growth media supplemented with 40 ng/mL rCSF-1; control wells received serum-free growth media only. The fibronectin coated inserts were then placed onto the wells. 100 μL of RAW-NZ (100,000 cells/well) solution was added into each insert and incubated for 12 h at 37 °C and 5% CO_2. Non-migratory cells were removed with a Q-tip and migratory cells at the bottoms of the inserts were fixed in 4% formaldehyde and stained with a 0.1% crystal violet solution in 25% methanol. Membranes were removed precisely, mounted onto cover-glass, and visualized under a Zeiss Axio Observer Z1 with an Axio Cam 506 Color attachment under a 20× objective lens. The cells were counted from three random, non-overlapping fields of view per membrane, with three membranes per condition (n = 3*3 = 9). Box and whisker plots were generated using OriginPro 2017.

3.4.5 Co-culture experiment of RAW_NZ with HeLa cells. Glass slides were coated with poly-lysine solution followed by washing with PBS. The slides were dried overnight. Each of the dry glass slides was placed onto each well of 6-well plates. Macrophages (RAW 264.7) (100k/well) in standard growth media were seeded in designated wells with glass slides. 3 mL of this media was used for each well to ensure that the glass slides remained immersed fully in the solution. The cells were treated with 100 nM NZs for the wells designated as RAW_NZ. In parallel, HeLa cells (100,000/well) were seeded in separate 6 well plates. The plates were stored under physiological conditions for 24 h. HeLa cells were washed three times with PBS followed by

adding fresh standard growth media. The glass slides coated with RAW 264.7/ RAW_NZ were thoroughly washed with PBS to remove any non-adhered cells and/or excess NZ. The slides coated with RAW 264.7/RAW_NZ were then removed carefully with a tweezer from their designated wells and placed atop the HeLa cells for coculture, so that both HeLa cells and RAW 264.7/RAW_NZ remained in the same solution. For control experiments with only HeLa cells, blank glass slides were placed on top of the cells. For control experiments with only RAW 264.7 cells, the slides coated with RAW 264.7 cells were placed in wells with only media. The cells were incubated with prodrug/drug for 24 h followed by washing three times with PBS. The glass slides were removed and placed in separate 6-well plates. All wells (with cells now separated) were thoroughly washed with PBS three times. Alamar blue assay was performed separately for HeLa and RAW 264.7 cells.

3.4.6 Co-culture experiment of RAW_NZ with GFP expressing HeLa cells (GFP_HeLa) and U2OS cells (GFP_U2OS). RAW 264.7 cells were seeded at a concentration of 100,000 cells/2 mL in confocal dishes. The cells were incubated with 100 nM NZ solution for 24 h followed by washing three times with PBS. GFP_HeLa/GFP_U2OS cells were added to the dishes at a concentration of 100,000 cells/dish to perform coculture of RAW_NZ+GFP_HeLa and RAW_NZ+GFP_U2OS, respectively. After 24 hours, the co-cultured cells were washed three times with PBS and incubated with prodrug for 24 h. The media in the confocal dishes was replaced with PBS before imaging. Confocal microscopy images were obtained on Nikon A1 spectral detector confocal microscope (A1SP) using a 60x objective. The settings of the confocal microscope were as follows: green channel, l_{ex} = 488 nm and l_{em} = BP 505-530 nm; emission filters: BP, band pass; LP, high pass.

3.5 Supplementary information

3.5.1 Mass spectrometric characterization of ligand on NPs. The surface ligand was characterized by matrix assisted maser desorption/ionization mass spectrometry (MALDI-MS). A

stock solution of matrix α-Cyano-4-hydroxycinnamic acid (α-CHCA) was prepared in a mixture of 70% acetonitrile and 30% deionized water. AuNPs were diluted in deionized water to a final concentration of 1 µM followed by addition to the matrix solution in a 1:1 volume ratio. 2 µL of this mixture was spotted on the sample carrier and allowed to dry. MALDI-MS analysis was performed using a Bruker Autoflex III mass spectrometer. A peak at m/z 422.637 was detected for TTMA AuNPs.

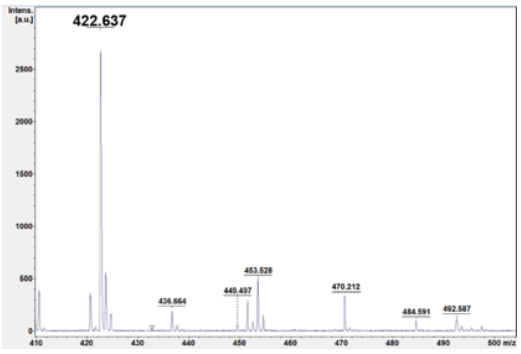

Figure 3.6. MALDI-MS for TTMA AuNPs.

3.5.2 Zeta Potential characterization of AuNPs. Hydrodynamic diameter of the nanoparticles and nanozymes were measured by dynamic light scattering (DLS) in DI water using a Malvern Zetasizer Nano ZS instrument by using the measurement angle of 173° (backscatter). Data were analyzed by the "multiple narrow modes" (high resolution) based on non-negative-least-squares (NNLS).

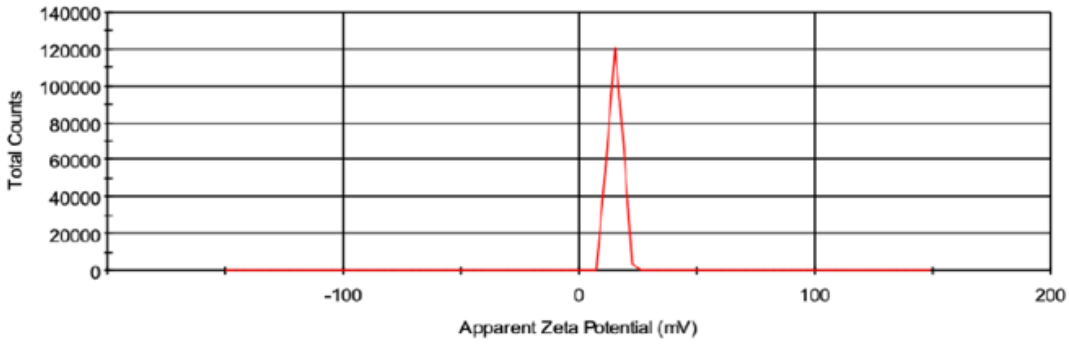

Figure 3.7. Zeta potential of TTMA AuNPs (potential found is 18 ± 2.9).

3.5.3 DLS and TEM characterization of AuNP and NZ. Hydrodynamic diameter of AuNPs and NZs were measured by dynamic light scattering (DLS) in DI water using a Malvern Zetasizer Nano ZS instrument by using a measurement angle of 173° (backscatter). Data were analyzed by the "multiple narrow modes" (high resolution) based on non-negative-least-squares (NNLS).

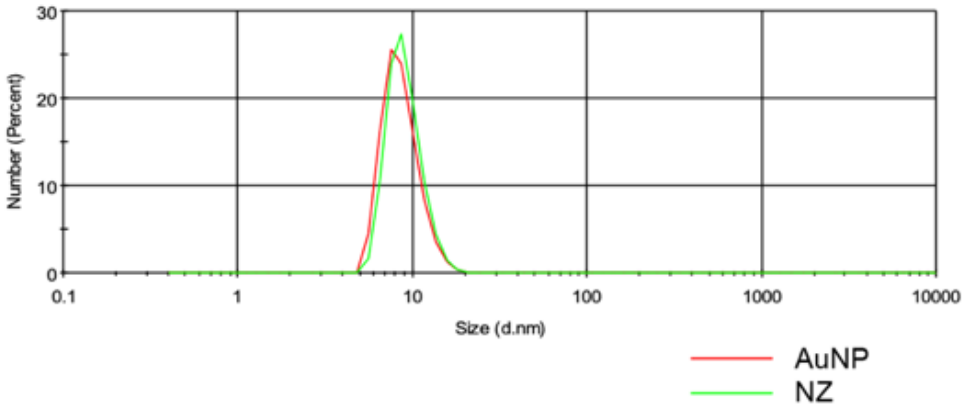

Figure 3.8. DLS measurements of AuNPs and NZs, indicating no aggregation before or after catalyst encapsulation.

Transmission Electron Microscopy (TEM) imaging samples were prepared by placing a droplet of AuNP and NZ solution of 1 μM onto a 300-mesh Cu-grid coated with carbon film. The samples were analyzed using a JEOL CX-100 electron microscope. These characterization data indicated that there was no aggregation before or after catalyst encapsulation.

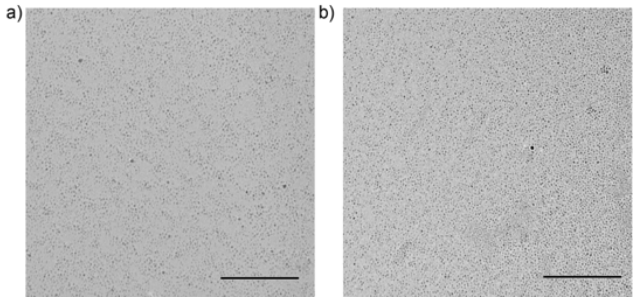

Figure 3.9. TEM images of a) AuNPs and b) NZs. Scale bar = 100 nm

3.5.4 Quantification of catalyst per AuNP using ICP-MS characterization. The ICP-MS analyses were performed on a Perkin-Elmer NexION 300X ICP mass spectrometer. ^{197}Au and

^{106}Pd were measured under the standard mode. Operating conditions were: nebulizer flow rate: 0.95 L/min; rf power: 1600 W; plasma Ar flow rate: 18 L/min; dwell time: 50 ms. Standard gold and palladium solutions were prepared via serial dilutions (0, 0.2, 0.5, 1, 2, 5, 10, and 20 ppb) for the calibration curve. It was found that 37 ± 1 catalysts were present per AuNP.

Table 3.1. Quantification of encapsulated catalysts in the 2 nm TTMA-AuNP

	Au(ng)	Pd(ng)	Pd(ng)/AuNP(pmol)	Pd/AuNP
NZ	62.3	5.3	3.9	37 ± 1
	65.9	5.5	4	
	63.2	5.5	4.1	

3.5.5 Cytotoxicity measurements of prodrug and drug. HeLa cells were seeded at a concentration of 10,000 cells/well in a 96 well plate overnight. The next day, the cells were treated with pro-5FU and 5FU at various concentrations for 24 h. After the incubation period, the cells were washed three times with PBS to remove dead cells and excess pro-5FU/5FU. 10% alamar blue in serum containing media was added to each well (220 μL) and incubated for 2 h further at 37 °C and 5% CO_2. Cell viability was then determined by measuring the fluorescence intensity at 570 nm using a SpectraMax M5 microplate spectrophotometer. The cell viability results indicated the presence of a therapeutic window between the prodrug and the drug.

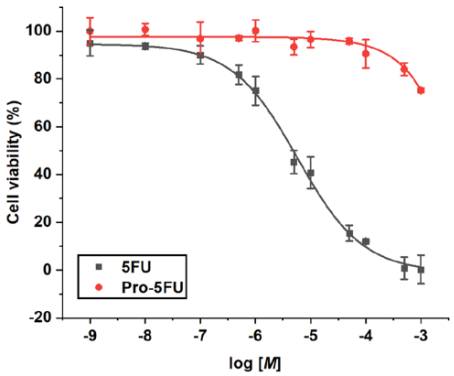

Figure 3.10. Viability of cells treated with pro-5FU and 5FU at various concentrations as determined by alamar blue assay.

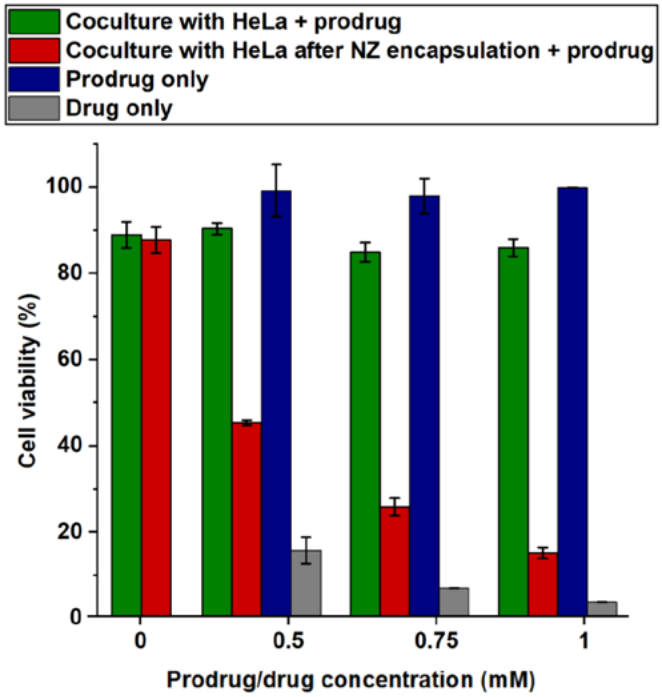

Figure 3.11. Viability of RAW 264.7 cells treated with pro-5FU and 5FU at various concentrations as determined by alamar blue assay.

3.6 References

1. Danhier, F.; Feron, O.; Préat, V. To Exploit the Tumor Microenvironment: Passive and Active Tumor Targeting of Nanocarriers for Anti-Cancer Drug Delivery. *J. Control. Release* **2010**, *148*, 135–146.

2. Byrne, J. D.; Betancourt, T.; Brannon-Peppas, L. Active Targeting Schemes for Nanoparticle Systems in Cancer Therapeutics. *Adv. Drug Deliv. Rev.* **2008**, *60*, 1615–1626.

3. Garzon, R.; Marcucci, G.; Croce, C. M. Targeting MicroRNAs in Cancer: Rationale, Strategies and Challenges. *Nat. Rev. Drug Discov.* **2010**, *9*, 775-782.

4. Murdoch, C.; Giannoudis, A.; Lewis, C. E. Mechanisms Regulating the Recruitment of Macrophages into Hypoxic Areas of Tumors and Other Ischemic Tissues. *Blood* **2004**, *104*, 2224–2234.

5. Brown, J. M.; Giaccia, A. J. The Unique Physiology of Solid Tumors: Opportunities (and Problems) for Cancer Therapy. *Cancer Res.* **1998**, *58*, 1408 LP – 1416.

6. Joshi, B. P.; Hardie, J.; Farkas, M. E. Harnessing Biology to Deliver Therapeutic and Imaging Entities via Cell-Based Methods. *Chem. Eur. J.* **2018**, *24,* 8717–8726.

7. Pollard, J. W. Tumour-Educated Macrophages Promote Tumour Progression and Metastasis. *Nat. Rev. Cancer* **2004**, *4*, 71–78.

8. Lewis, C. E.; Pollard, J. W. Distinct Role of Macrophages in Different Tumor Microenvironments. *Cancer Res.* **2006**, *66*, 605–612.

9. Joshi, B. P.; Hardie, J.; Mingroni, M. A.; Farkas, M. E. Surface-Modified Macrophages Facilitate Tracking of Breast Cancer-Immune Interactions. *ACS Chem. Biol.* **2018**, *9,* 509-516.

10. Pierigè, F.; Serafini, S.; Rossi, L.; Magnani, M. Cell-Based Drug Delivery. *Adv. Drug Deliv. Rev.* **2008**, *60*, 286–295.

11. Choi, M. R.; Stanton-Maxey, K. J.; Stanley, J. K.; Levin, C. S.; Bardhan, R.; Akin, D.; Badve, S.; Sturgis, J.; Robinson, J. P.; Bashir, R.; *et al.* A Cellular Trojan Horse for Delivery of Therapeutic Nanoparticles into Tumors. *Nano Lett.* **2007**, *7*, 3759–3765.

12. Doshi, N.; Swiston, A. J.; Gilbert, J. B.; Alcaraz, M. L.; Cohen, R. E.; Rubner, M. F.; Mitragotri, S. Cell-Based Drug Delivery Devices Using Phagocytosis- Resistant Backpacks. **2011**. *17,* 269-276.

13. Anselmo, A. C.; Mitragotri, S. Cell-Mediated Delivery of Nanoparticles: Taking Advantage of Circulatory Cells to Target Nanoparticles. *J. Control. Release* **2014**, *190*, 531–541.

14. Batrakova, E. V; Gendelman, H. E.; Kabanov, A. V. Cell-Mediated Drug Delivery. *Expert Opin. Drug Deliv.* **2011**, *8*, 415–433.

15. Mura, S.; Nicolas, J.; Couvreur, P. Stimuli-Responsive Nanocarriers for Drug Delivery. *Nat. Mater.* **2013**, *12*, 991–1003.

16. Ganta, S.; Devalapally, H.; Shahiwala, A.; Amiji, M. A Review of Stimuli-Responsive Nanocarriers for Drug and Gene Delivery. **2008**, *126*, 187–204.

17. Sletten, E. M.; Bertozzi, C. R. Bioorthogonal Chemistry: Fishing for Selectivity in a Sea of Functionality. *Angew. Chemie - Int. Ed.* **2009**, *48*, 6974–6998.

18. Völker, T.; Meggers, E. Transition-Metal-Mediated Uncaging in Living Human Cells-an Emerging Alternative to Photolabile Protecting Groups. *Curr. Opin. Chem. Biol.* **2015**, *25*, 48–54.

19. Springer, C. J.; Niculescu-Duvaz, I.; Marais, R.; Spooner, R.; Light, Y.; Martin, J.; Springer, C.; Bridgewater, J.; Huber, B.; Richards, C.; *et al.* Prodrug-Activating Systems in Suicide Gene Therapy. *J. Clin. Invest.* **2000**, *105*, 1161–1167.

20. Denmeade, S. R.; Mhaka, A. M.; Rosen, D. M.; Brennen, W. N.; Dalrymple, S.; Dach, I.; Olesen, C.; Gurel, B.; DeMarzo, A. M.; Wilding, G.; *et al.* Engineering a Prostate-Specific Membrane Antigen–Activated Tumor Endothelial Cell Prodrug for Cancer Therapy. *Sci. Transl. Med.* **2012**, *4*, 140ra86 LP-140ra86.

21. Das, R.; Landis, R. F.; Tonga, G. Y.; Cao-Milán, R.; Luther, D. C.; Rotello, V. M. Control of Intra- versus Extracellular Bioorthogonal Catalysis Using Surface-Engineered Nanozymes. *ACS Nano* **2019**, *13,* 229-235.

22. Gupta, A.; Das, R.; Yesilbag Tonga, G.; Mizuhara, T.; Rotello, V. M. Charge-Switchable Nanozymes for Bioorthogonal Imaging of Biofilm-Associated Infections. *ACS Nano* **2018**, *12*, 89–94.

23. Tonga, G. Y.; Jeong, Y.; Duncan, B.; Mizuhara, T.; Mout, R.; Das, R.; Kim, S. T.; Yeh, Y.-C.; Yan, B.; Hou, S.; *et al.* Supramolecular Regulation of Bioorthogonal Catalysis in Cells Using Nanoparticle-Embedded Transition Metal Catalysts. *Nat. Chem.* **2015**, *7*, 597–603.

24. Cao-milán, R.; He, L. D.; Shorkey, S. Molecular Systems Design & Engineering Modulating the Catalytic Activity of Enzyme-like Nanoparticles through Their Surface. **2017**, 624–628.

25. Pixley, F. J.; Stanley, E. R. CSF-1 Regulation of the Wandering Macrophage : Complexity in Action, *Trends Cell. Biol.* **2004**, *14*, 10–12.

26. Jiang, Y.; Huo, S.; Mizuhara, T.; Das, R.; Lee, Y.-W.; Hou, S.; Moyano, D. F.; Duncan, B.; Liang, X.-J.; Rotello, V. M. The Interplay of Size and Surface Functionality on the Cellular Uptake of Sub-10 Nm Gold Nanoparticles. *ACS Nano* **2015**, *9*, 9986–9993.

27. Rana, S.; Bajaj, A.; Mout, R.; Rotello, V. M. Monolayer Coated Gold Nanoparticles for Delivery Applications. *Adv. Drug Deliv. Rev.* **2012**, *64*, 200–216.

28. Ghosh, P.; Han, G.; De, M.; Kim, C. K.; Rotello, V. M. Gold Nanoparticles in Delivery Applications. *Adv. Drug Deliv. Rev.* **2008**, *60*, 1307–1315.

29. Albanese, A.; Tang, P. S.; Chan, W. C. W. The Effect of Nanoparticle Size, Shape, and Surface Chemistry on Biological Systems. *Annu. Rev. Biomed. Eng.* **2012**, *14*, 1–16.

30. Yesilbag Tonga, G.; Mizuhara, T.; Saha, K.; Jiang, Z.; Hou, S.; Das, R.; Rotello, V. M. Binding Studies of Cucurbit[7]Uril with Gold Nanoparticles Bearing Different Surface Functionalities. *Tetrahedron Lett.* **2015**, *56*, 3653–3657.

31. Yusop, R. M.; Unciti-broceta, A.; Johansson, E. M. V; Sa, R. M.; Bradley, M. Palladium-Mediated Intracellular Chemistry. **2011**, *3*, 239–243.

32. Li, J.; Chen, P. R. Reactions in Bioorthogonal Chemistry. *Nat. Publ. Gr.* **2016**, *12*, 129–137.

33. Weiss, J. T.; Dawson, J. C.; Macleod, K. G.; Rybski, W.; Fraser, C.; Torres-Sánchez, C.; Patton, E. E.; Bradley, M.; Carragher, N. O.; Unciti-Broceta, A. Extracellular Palladium-Catalysed Dealkylation of 5-Fluoro-1-Propargyl-Uracil as a Bioorthogonally Activated Prodrug Approach. *Nat. Commun.* **2014**, *5*, 3277-3285.

34. Longley, D. B.; Harkin, D. P.; Johnston, P. G. 5-Fluorouracil: Mechanisms of Action and Clinical Strategies. *Nat. Rev. Cancer* **2003**, *3*, 330–338.

35. Cohen, S. S.; Flaks, J. G.; Barner, H. D.; Loeb, M. R.; Lichtenstein, J. The Mode of Action of 5-Fluorouracil and Its Derivatives. *Proc. Natl. Acad. Sci. U. S. A.* **1958**, *44*, 1004–1012.

36. Brust, M.; Walker, M.; Bethell, D.; Schiffrin, D. J.; Whyman, R. Synthesis of Thiol-Derivatised Gold Nanoparticles in a Two-Phase Liquid-Liquid System. *J. Chem. Soc. Chem. Commun.* **1994**, 801–802.

37. Chowdhuri, A. R.; Kumar, A.; Gwisai, T.; Rosita, N. Synergistic Antimicrobial Therapy Using Nanoparticles and Antibiotics for the Treatment of Multidrug-Resistant Bacterial Infection Synergistic Antimicrobial Therapy Using Nanoparticles and Antibiotics for the Treatment of Multidrug-Resistant Bacterial Inf.

38. R. Miranda, O.; Chen, H.-T.; You, C.-C.; E. Mortenson, D.; Yang, X.-C.; H. F. Bunz, U.; M. Rotello, V. Enzyme-Amplified Array Sensing of Proteins in Solution and in Biofluids. *J. Am. Chem. Soc.* **2010**, *132*, 5285–5289.

39. Ghosh, P.; Han, G.; De, M.; Kim, C. K.; Rotello, V. M. Gold Nanoparticles in Delivery Applications. *Adv. Drug Deliv. Rev.* **2008**, *60*, 1307–1315.

40. Suetsugu, A.; Katz, M.; Fleming, J.; Truty, M.; Thomas, R.; Saji, S.; Moriwaki, H.; Bouvet, M.; Hoffman, R. M. Noninvasive Fluorescent-Protein Imaging of Orthotopic Pancreatic Cancer Patient Tumorgraft Progression in Nude Mice. *Anticancer Res.* **2012,** *32*, 3063-3070.

41. Joshi, B. P.; Hardie, J.; Mingroni, M. A.; Farkas, M. E. Surface-Modified Macrophages Facilitate Tracking of Breast Cancer-Immune Interactions. *ACS Chem. Biol.* **2018**, *9, 509*-516.

CHAPTER 4

CHARGE-SWITCHABLE NANOZYMES FOR BIOORTHOGONAL IMAGING OF BIOFILM-ASSOCIATED INFECTIONS

4.1 Introduction

Bacterial infections are serious threat to public health, causing > 2 million cases of illnesses and >23,000 deaths each year in U.S.[1] The majority of human bacterial infections (~80%) are associated with biofilm formation on living tissues.[2] Biofilms are three-dimensional bacterial communities where microbes reside in an extracellular polymeric substance (EPS) matrix, and are highly protected from exogenous agents. Biofilm-associated infections are responsible for a range of chronic diseases including endocarditis, osteomyelitis and implant dysfunction, and are key co-morbity threats for other diseases such as cystic fibrosis.[3,4] Currently, biofilm infections are typically diagnosed only after they have become systemic or have caused significant anatomical damage,[5,6] highlighting the need for effective imaging tools.

Current techniques for imaging bacteria use probes such as autologous white blood cells[7], maltodextrin[8] and dipicolylamine zinc (II).[9] Although these systems are effective for imaging planktonic (dispersed) bacterial infections, only limited studies have been conducted on imaging of biofilm-associated infections.[10-12] Other imaging modalities such as ^{67}Ga-citrate and radiolabeled autologous white blood cells lack the spatial resolution required for surgical procedures such as debridement of infected tissue.6,[13] Most high resolution optical imaging approaches rely on fluorescent dyes conjugated to a biorecognition element, generating highly specific imaging probes that are susceptible to false responses due to phenotypic mutations of biofilm residing microbes.[14,15] Moreover, physical heterogeneity and complex biofilm architecture further complicates imaging of these highly refractory infections.[16] In particular, the dense and amphiphilic nature of EPS matrix prevents the penetration of imaging agents.[17,18] Synthetic macromolecules such as nanoparticles

(NPs) have shown potential to penetrate biofilms[19], however they currently lack the ability to intrinsically target these resilient infections.[20,21]

Biofilms have inherently acidic microenvironments (pH 4.5-6.5) as a by-product of sugar fermentation caused by bacteria.[22] For instance, pH in human dental biofilms often reaches below 4.5 causing acidic dissolution of tooth enamel.[23] Similarly, cystic fibrosis (CF) pulmonary infections are associated with acidification of airways in CF patients.[24] We hypothesized that pH-responsive sulfonamide-functionalized gold nanoparticles (AuNPs)[25] could be used to target this acidic environment. In this system, targeting of the biofilm is achieved through charge-switchable NPs that transition from zwitterionic (non-adhesive) to cationic (adhesive) at the pH values typically found in biofilms, providing a broad-spectrum recognition platform for bacteria with selectivity towards biofilms compared to healthy mammalian cells. Imaging of the biofilms is achieved by the embedded transition metal catalysts (TMCs) that activate the pro-fluorophores *in situ* inside the biofilms. These bioorthogonal 'nanozymes' provide an effective imaging system that selectively targets bacterial biofilms and provides amplified fluorescence signal output using bioorthogonal catalysis. This nanozyme platform was used to effectively image biofilms of different bacterial species with complete EPS matrix penetration, and to image biofilms in a complex mammalian cell - biofilm co-culture model.

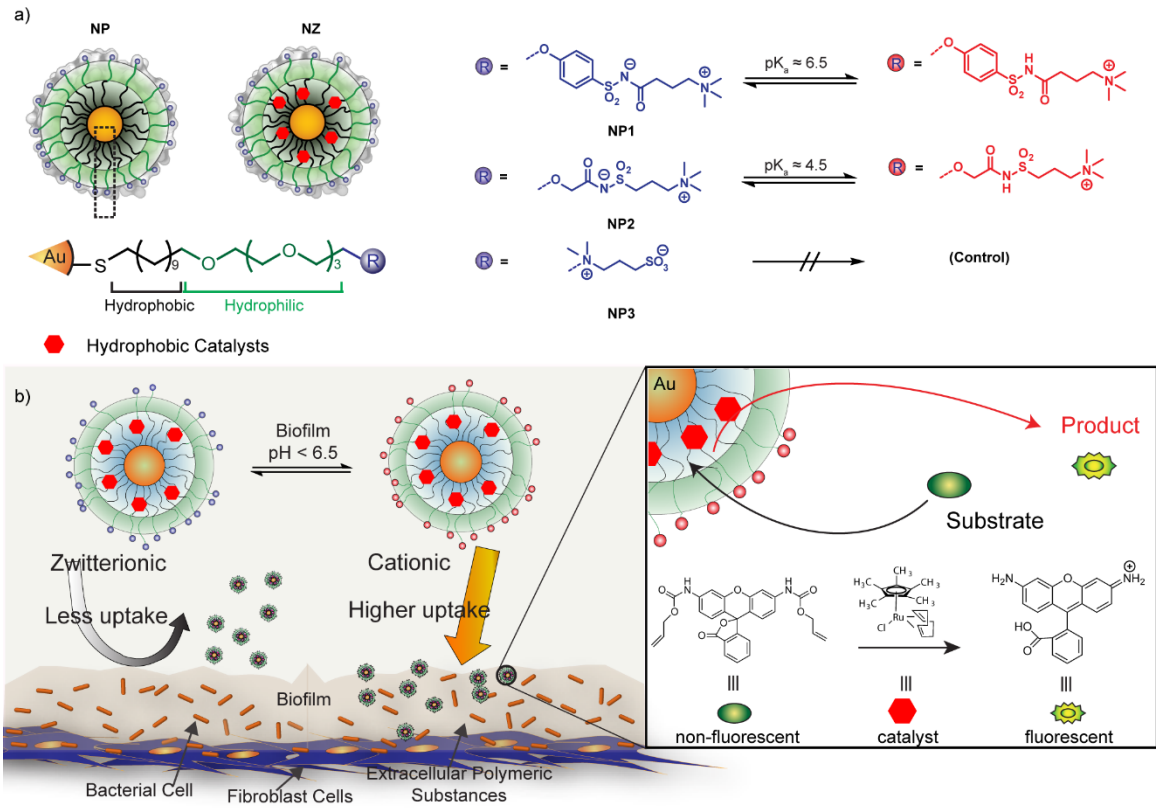

Figure 4.1. a) Molecular structures of pH-switchable and control ligands on gold nanoparticles (AuNPs). b) Schematic representation showing selective targeting of biofilm infections using pH-responsive nanoparticles and intrabiofilm fluorogenesis of profluorophores by transition metal catalysts (TMCs) embedded in the nanoparticle monolayers.

4.2 Results and discussion

Sensing was performed with 2nm AuNPs featuring terminal groups with distinct pK$_a$ values to selectively target the acidic microenvironment of biofilms.[25] Alkoxyphenyl acylsulfonamide-functionalized NP1 features groups that are protonated under weakly acidic conditions (pK$_a$ ~ 6.5), consistent with normal biofilm pH. Acylsulfonamide-functionalized NP2 has slightly lower pK$_a$ (~4.5) than its aryl analog, providing a tool for measuring the lower extremes of biofilm pH. Finally, NP3 features a sulfobetaine termini, providing a stable zwitterionic control for our studies (pKa < 1) (Figure 4.1 a).[26,27] These particles were synthesized from pentane-thiol capped 2nm core AuNPs using a place exchange reaction.

The nanozymes were generated through encapsulation of a ruthenium-based catalyst-[Cp*Ru(cod)Cl] (Cp* = pentamethylcyclopentadienyl, cod = 1,5-cyclooctadiene) into the ligand monolayer of NP1-3 to generate the respective nanozymes (NZ1-3).[28] Transmission electron microscopy (TEM) images and dynamic light scattering data of NPs before and after encapsulation of catalysts show no signs of aggregation. Further size distribution studies for NZs were conducted at a range of pH (3.5-7.4) using DLS, demonstrating their stability even in the acidic conditions (Figure 4.S1, Figure 4.S2). The quantification of catalysts encapsulated was done using inductively coupled plasma mass spectrometry (ICP-MS), indicating that 24 ± 2 catalyst molecules were encapsulated per AuNP for NZ1-3. The catalysts encapsulated per AuNP were similar at different pH ranges (3.5-7.4), as validated using ICP-MS (Figure 4.S3).

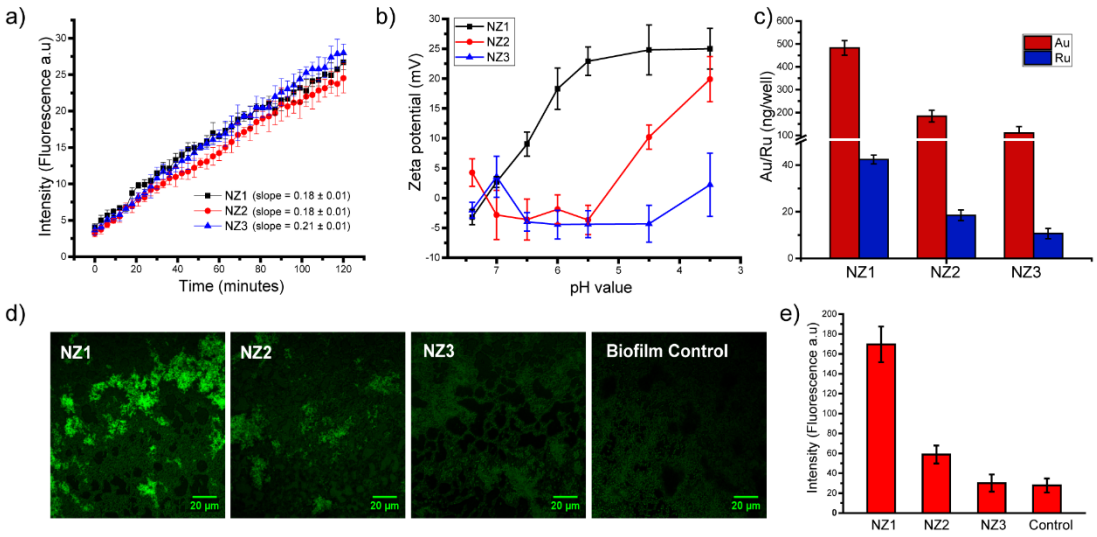

Figure 4.2. a) Catalysis of nanozymes with different chemical headgroups in neutral pH for 2 h at 37 °C. b) ζ-Potential of NZ1−3 (1 µM) measured in the pH range of 3.5−7.4 is plotted against different pH values. Error bars represent standard deviations based on three independent measurements per pH value. c) Nanoparticle and catalyst diffusion into P. aeruginosa (CD-1006) biofilms after incubation for 1 hr in pH 7.4 media with NZ1−3 (400 nM), as measured by ICP-MS. d) Confocal images of biofilm incubated with nanozymes (1 h, 400 nM) followed by incubation with alloc-Rho (1 h, 100 µM); biofilm control is the negative control in the absence of nanozyme. e) Quantitative analysis of fluorescence intensity generated upon addition of different nanozymes.

The catalytic activities of NZ1-3 were assessed in solution by deallylation of bis-N, N'-allyloxycarbonyl rhodamine 110 (alloc-Rho, Figure 4.1) at pH = 7.4.[29] The rate of increase in

fluorescence was similar (Figure 4.2a) for the NZ1-3 complexes, indicating similar catalytic activity for all NZs at physiological pH. Further, we tested the catalytic activity of NZ1 with varying pH (3.5-7.4), indicating no significant difference in the catalysis rate for the nanozyme (Figure 4.S4).

After establishing their catalytic activity in solution, we determined the pH dependence of the NZ's surface charge by measuring their zeta potential. The surface charge of all three NZs (1-3) were close to neutral at physiological pH (7.4), consistent with their zwitterionic structures. NZ (1-2) exhibited a sharp transition from neutral to overall positive charge at pH 6.5 and pH 4.5 respectively, consistent with their respective pKa's. As expected, NZ3 possessed near neutral charge even at highly acidic pH values as seen in Figure 4.2b and Figure 4.S2. Next, we performed NZ diffusion studies in biofilms using ICP-MS to investigate their ability to penetrate and accumulate inside biofilms. We observed that switchable NZ1 showed the highest diffusion into biofilms based on Au, with lesser amounts observed with NZ2 and NZ3 respectively (Figure 4.2c). This trend is mirrored in the Ru signal from the catalyst. This overall change to cationic surface charge of the pH-responsive NZs can play a crucial role in their ability to intrinsically target biofilms over the mammalian cells (Figure 4.S5).

We then investigated the ability of NZs to image biofilms using confocal microscopy. We chose uropathogenic clinical isolate of *P. aeruginosa* (CD-1006) as a model strain for imaging studies due to their high prevalence in clinical biofilms.[30,31] Imaging studies of biofilms were based on generation of fluorophore (Rhodamine 110) through deallylation of a non-fluorescent precursor as shown in Figure 4.1b. Catalytic activity of the NZs was probed inside the biofilms by incubating the NZs with biofilms for 1 h, followed by multiple washings to remove absorbed particles. Fresh media containing substrate was added following 1 h incubation and subsequent washings. Confocal images of biofilms treated with switchable NZ1 exhibited bright fluorescence, with only localized fluorescence observed with NZ2, and little or no fluorescence beyond auto fluorescence observed with NZ3, results mirrored in the quantified intensities (Figure 4.2 d, e). These results suggest that

pH responsive zwitterionic nanozyme NZ1 can be used to target the biofilms for imaging applications.

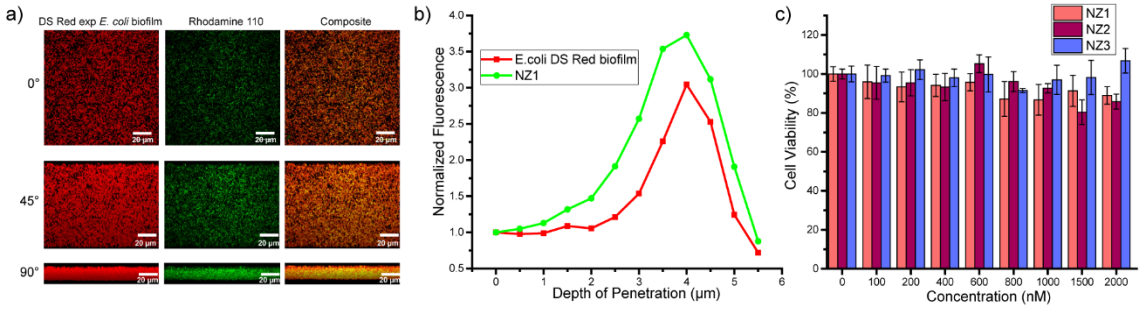

Figure 4.3. a) Confocal microscopy images of DS Red exp E. coli and activated Rhodamine 110 fluorophore in the presence of NZ1. Composite images show homogeneous colocalization of biofilm and activated fluorophores. The panels are projections at 0, 45, and 90° angle turning along the Y-axis. The scale bars are 20 μm b) Integrated intensity of Rhodamine 110 and DS Red biofilm after 1 h incubation with NZ1. The x-axis is the depth of penetration of biofilms, where 0 μm represents the top layer and ~5.6 μm the bottom layer. The y-axis, normalized fluorescence, is normalized intensity of red and green channels at the top layer to compare their localization c) Cell viability of 3T3 fibroblast cells after 24 h incubation with NZ1−3 (0.1−2 μM). The data are average of triplicates, and the error bars indicate standard deviations.

Z-stack confocal imaging was used to determine the localization of activated fluorophores inside DS Red (red fluorescent protein) expressing *E. coli* biofilms (Figure 4.3a). The penetration profile of NZ1 was quantified by using NIS element analysis software.[32] The intensity of green and red channel represents the intensity of Rhodamine-110 and biofilms respectively. The integrated intensities were normalized at the top layer of biofilm to compare their co-localization with varying biofilm depth (0-5.6 μm). As shown in Figure 4.3b, the activated fluorophore (Rhodamine 110) was distributed throughout the biofilm. Biofilms incubated without NZ1 were used as negative control. The ability of switchable NZ1 to image bacterial biofilms was further validated against three bacterial strains of clinical isolates - *Enterobacter cloacae* (CD-1412), methicillin-resistant *Staphylococcus aureus* (CD-489) and *Escherichia coli* (CD-2), demonstrating effective imaging of biofilms formed by both Gram positive (*S. aureus*) and Gram negative (*E. coli, P. aeruginosa, E. cloacae*) (Figure 4.S6) species. Further, we tested the cytotoxicity of these NZs against NIH 3T3

Fibroblast-cells that maintain high cell viability at 2 µM NZ incubation (Figure 4.3c). These studies indicate the biocompatibility of our zwitterionic nanozymes with mammalian cells.

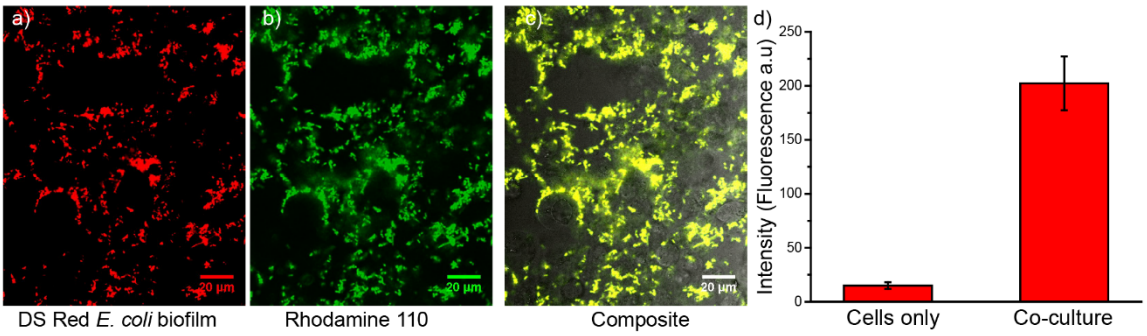

Figure 4.4. Confocal images of a fibroblast-DS Red E. coli biofilm coculture model incubated with switchable nanozyme NZ1 (400 nM) and alloc-rhodamine (nonfluorescent, 100 µM) for 1 h. a) DS Red, b) Rhodamine 110, and c) merged channels. d) Quantitative analysis of fluorescence intensity observed in the images of noninfected cells (cells only) and cells infected with biofilm (coculture). Scale bar is 20 µm.

Imaging of biofilms on biomedical surfaces such as medical implants and indwelling devices is a critical capability. However, tracking biofilm-associated infections on human tissues and organs is even more challenging and relevant for medical applications. In most cases of bacterial infections, microbes are embedded in human tissues inside resilient biofilms comprised of EPS.[33] Having established that pH responsive NZ1 exhibits the highest selectivity towards biofilms and are non-toxic to fibroblast cells, we next investigated their ability to track biofilms, using fibroblast-biofilm co-culture as a model. We chose DS Red (red fluorescent protein) expressing *E. coli* as representative strain to generate co-culture model using previously established protocols.[34,35,36] Co-cultures were then incubated with NZ1 for 1 hour, followed by multiple washings to remove non-adhering NZs. Subsequently, substrate alloc-Rho was added in fresh media for 1 hour, followed by multiple washing to remove excess substrate. The co-culture models were examined using confocal microscopy, exhibiting strong co-localization of Rhodamine and DS Red (from biofilm) and minimal fluorescence around mammalian cells (Figure 4.4, procedure to analyze image intensity is described in section 4.5, Figure 4.S7). The co-cultures incubated with alloc-Rho in absence of NZ1 was used as negative control. This high level of selectivity

demonstrates the potential of switchable NZs to image bacterial biofilms in physiologically relevant conditions. Their ability to selectively target the biofilms can be attributed to the overall change in their surface charge (from neutral to cationic) at acidic conditions. The positively charged NZ1 shows high accumulation inside the biofilm, whereas the neutral charged NZ1 exhibits minimal uptake in fibroblast cells. Hence, the pro-fluorophore gets selectively activated in the biofilm, already inhabited by the charge switchable nanozyme.

4.3 Conclusions

In conclusion, we have developed a strategy for rapid and effective imaging of biofilms that was effective in a complex co-culture model. The pH-responsive NPs penetrate and accumulate inside the acidic microenvironment of biofilms, with bioorthogonal catalysis providing a sensitive readout mechanism. This bioorthogonal activation of imaging agents is a promising approach to detect biofilm-associated infections, and to locate infected sites during critical debridement surgeries. These pH responsive nanozymes offer a broad-spectrum strategy for imaging biofilms arising from different and/or mixed bacteria species, circumventing the need for designing microbe-specific probes. Considering their enhanced ability to penetrate the biofilm matrix, nanozymes hold a strong advantage against currently used imaging probes. In a broader context, this study demonstrates the utility of bioorthogonal catalysis for bioimaging.

4.4 Experimental methods

4.4.1 Synthesis of Gold Nanoparticles. Ligands were synthesized using previously reported procedure.[25, 37] AuNPs was prepared through place-exchange reaction of 1-pentanethiolprotected 2 nm gold nanoparticle (Au-C5) according to previously reported procedure.[38] Briefly, to the solution of Au-C5 (10 mg) in CH_2Cl_2 (1 mL) was added the solution of ligand 1 (30 mg) in CH_2Cl_2: MeOH (4:1, 3 mL). After being stirred at rt for 24 h, the solvent was evaporated *in vacuo*. After nanoparticle residue was washed with EtOAc (10 mL × 3), the

nanoparticle was immediately dissolved in MilliQ water and the aqueous solution of the nanoparticle was purified by dialysis with distilled water using SnakeSkin™ Dialysis Tubing (Thermo Scientific, 10,000 MWCO).

4.4.2 Catalyst encapsulation in AuNP monolayer. The catalyst, [Cp*Ru(cod)Cl] (3.0 mg) was dissolved in 1 ml acetone and the AuNP (20 μM, 0.5 mL) were diluted to a final concentration of 5 μM with DI water (1 ml). Then, the catalyst and the AuNP solutions were mixed together and acetone was slowly removed by evaporation. During the evaporation, hydrophobic catalyst was encapsulated in the particle monolayer to yield to NP_Ru. Excess catalysts which precipitated in water were removed by filtration (Millex-GP filter; 25 mm PES, pore Size: 0.22 μm) and dialysis (Snake Skin® dialysis tubing, 10K) against water (5 L) for 24 h. Further purifications were followed by multiple filtrations (five times, Amicon® ultra 4, 10K) to remove free catalysts. The amount of encapsulated catalysts was measured by ICP-MS by tracking ^{101}Ru relative to ^{197}Au for NP_Ru.

4.4.3 Nanozyme kinetics in solution. Allylcarbamate protected Rhodamine 110 (alloc-Rho) was used as a substrate to test the catalytic activity of the nanozymes. A solution containing 100 nM nanozyme and 1 μM substrate was prepared in a 96-well plate. 400 nM nanozyme solution and 100 nM substrate solutions alone were used as negative controls. The kinetic study was done by tracking the fluorescence intensity (Ex: 488 nm, Em: 521 nm, Cutoff: 515 nm) using a Molecular Devices SpectraMax M2 microplate reader.

4.4.4 Biofilm culture. Bacteria were inoculated in LB broth at 37°C until stationary phase. The cultures were then harvested by centrifugation and washed with 0.85% sodium chloride solution three times. Concentrations of resuspended bacterial solution were determined by optical density measured at 600 nm. Seeding solutions were then made in minimal media, M9 broth to reach OD_{600} of 0.1. 500 μL of the seeding solutions were added to each well of the 24-well microplate. M9 medium without bacteria was used as a negative control. The plates were covered

and incubated at room temperature under static conditions for a desired period of 24 hours. Planktonic bacteria were removed by washing with PB saline three times.

4.4.5 Diffusion of nanozymes inside biofilms. After plating bacterial cells in a 24-well plate. On the following day, planktonic bacteria were removed by washing with PBS three times. and incubated with NZ 1, NZ 2 and NZ 3 (400 nM each) in minimal M-9 media (pH 7.4) for 3 h at 37 °C. After incubation, biofilms were washed three times with PBS and lysis buffer was added to each well. All lysed samples were then further processed for ICP-MS analysis (*vide infra*) to determine the intracellular amount of gold and ruthenium. Diffusion experiments were performed independently at least two times and each experiment was comprised of three replicates.

4.4.6 Confocal imaging of biofilms. 10^8 bacterial cells/ml were seeded (2 ml in M9 media) in a confocal dish and were allowed to grow, old media was replaced every 24 hours. After 3 days media was replaced by 400 nM of the NZ 1, NZ 2 and NZ 3 and biofilms were incubated for 1 h, biofilm samples incubated with only M9 media were used as control. After 1 h, biofilms were washed with PBS three times and were incubated with 100 μM of the substrates for 1 h. The cells were then washed with PBS three times. Confocal microscopy images were obtained on a Zeiss LSM 510 Meta microscope by using a 60× objective. The settings of the confocal microscope were as follows: green channel: λ_{ex}=488 nm and λ_{em}=BP 505-530 nm; red channel: λ_{ex}=543 nm and λ_{em}=LP 650 nm. Emission filters: BP=band pass, LP=high pass.

4.4.7 Mammalian cell viability studies. These experiments were done using previously reported protocol.[39] Briefly, 20,000 NIH 3T3 fibroblast cells (ATCC CRL-1658) were cultured in DMEM medium in presence of 10% bovine calf serum and 1% antibiotic solution. The cells were cultured at 37 °C in a humidified atmosphere of 5% CO_2 for 48 h. Next, the cells were washed with phosphate-buffered saline (PBS) and different concentration of NZs (1-3) in 10% serum containing media were incubated with the cells for 3 h at 37 °C. After the incubation period, cells were washed with PBS (3 times) and cell viability was then determined using Alamar blue assays according to manufacturer's protocol (Invitrogen Biosource). Washed cells were incubated with 220 μl of 10%

Alamar Blue solution in 10% serum containing media. The solution was incubated at 37 °C under a humidified atmosphere of 5% CO_2 for 3 h. Subsequently, 200 µl solution from the wells was transferred in a 96-well black-microplate. The fluorescence reading was measured using a UV/vis spectrophotometer with excitation and emission at 560 and 590 nm respectively. Cell incubated without NPs were treated as 100% viable cells and the cell viability was calculated accordingly. These experiments were performed in triplicates.

4.4.8 Imaging of Co-culture models. Fibroblast-3T3 co-culture was performed using a previously reported protocol.[36] A total of 20,000 NIH 3T3 (ATCC CRL-1658) cells were cultured in Dulbecco's modified Eagle medium (DMEM; ATCC 30-2002) with 10% bovine calf serum and 1% antibiotics at 37°C in a humidified atmosphere of 5% CO_2. Cells were kept for 24 hours to reach a confluent monolayer in a confocal dish. Bacteria (*P. aeruginosa*) were inoculated and harvested as mentioned above. Afterwards, seeding solutions 10^8 cells/ml were inoculated in buffered DMEM supplemented with glucose. Old media was removed from 3T3 cells followed by addition of 2 mL of seeding solution. The co-cultures were then stored in a box humidified with damp paper towels at 37°C overnight without shaking. The co-cultures were treated with NZs and substrates using similar procedure used for biofilm models.

4.5 Supplementary information

4.5.1 Stability of NZs at different pH values. Hydrodynamic diameter of the NZs at different pH were measured by dynamic light scattering (DLS) in 5mM Phosphate buffer (pH 5.5-7.4) and 5mM Citrate buffer (pH 3.5-4.5) using a Malvern Zetasizer Nano ZS instrument. The NZs (1 µM) were incubated in the respective buffers for 3 hours before each measurement. No significant changes in the NZ size were observed. The size distribution by number are presented in the Figure 4.S1.

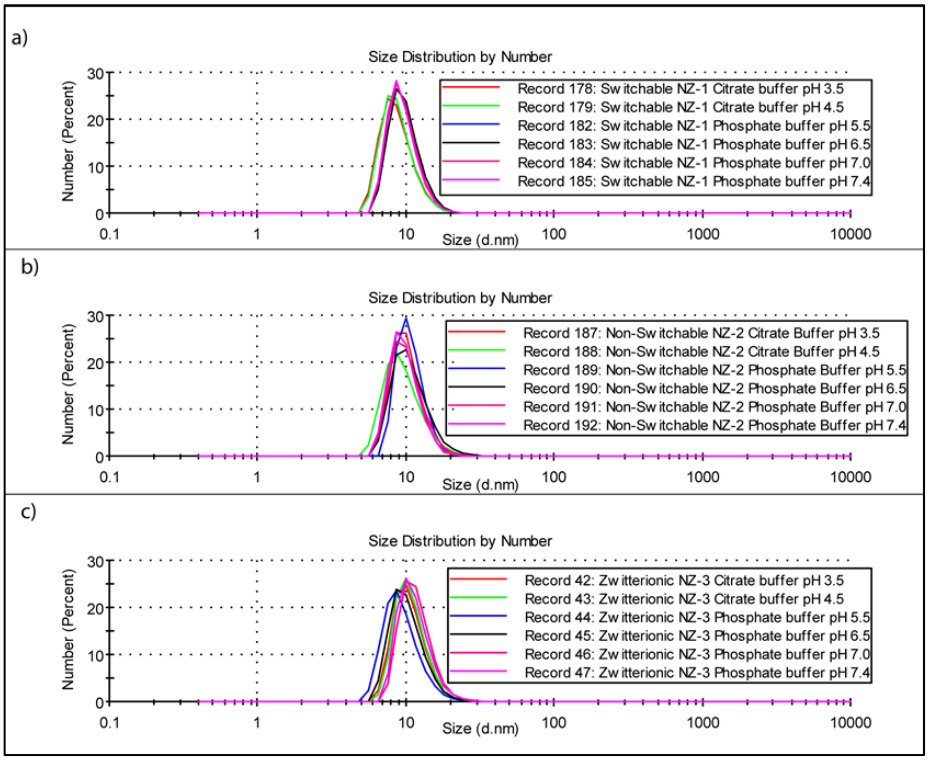

Figure 4.5. DLS measurements of NZs after 3-hour incubation in buffers with varying pH (3.5-7.4) indicate that NZ size remains same even at acidic conditions.

4.5.2 Zeta potential of NZs at different pH values. Zeta potential of the NZs at different pH were measured by dynamic light scattering (DLS) in 5mM Phosphate buffer (pH 5.5-7.4) and 5mM Citrate buffer (pH 3.5-4.5) using a Malvern Zetasizer Nano ZS instrument. The NZs (1 μM) were incubated in the respective buffers for 3 hours before each measurement. The zeta potential measured at different pH are presented below in the Figure 4.S2.

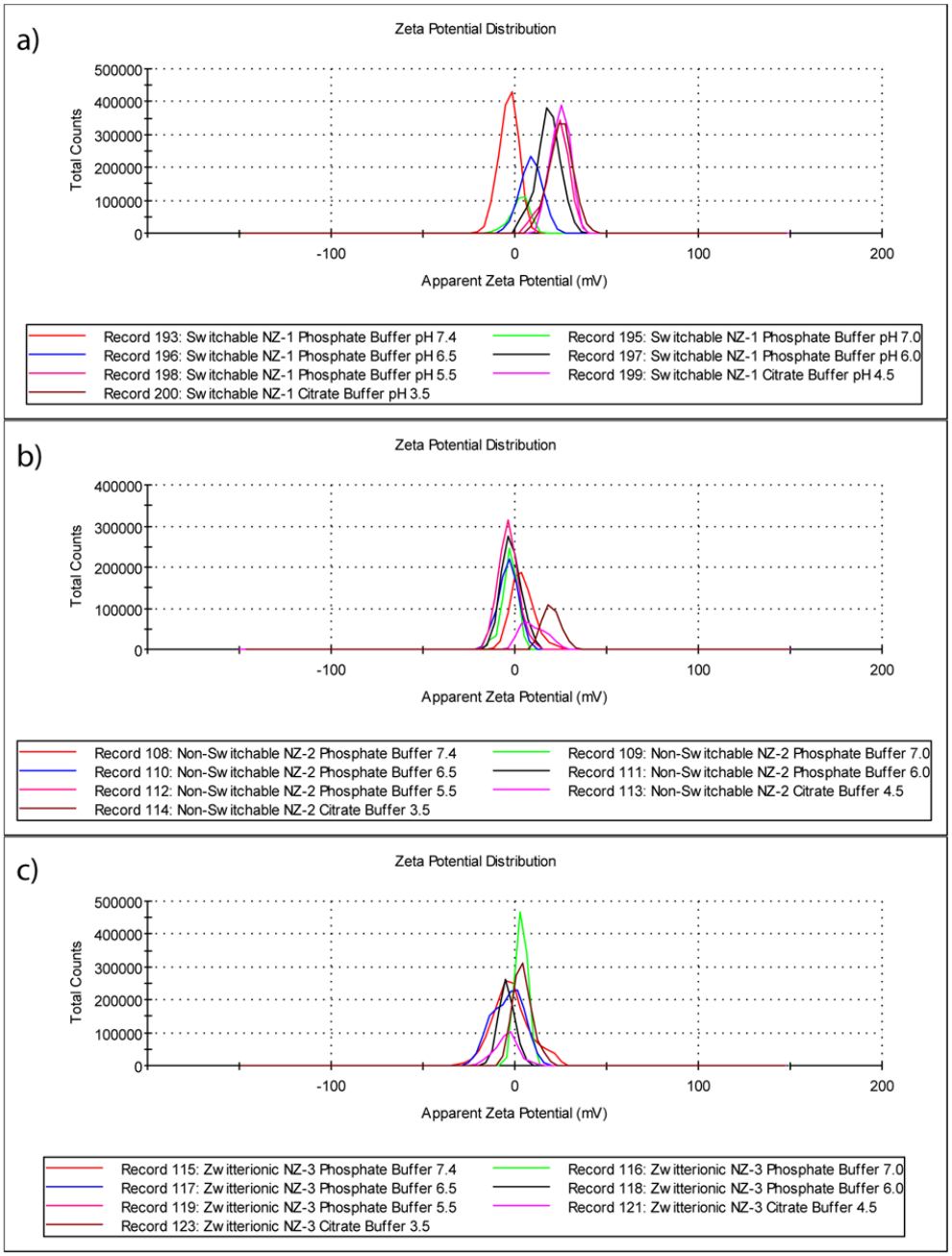

Figure 4.6. Zeta potential of NZs at different pH values, indicating overall change in surface charge of NZ1 and NZ2 at pH 6.5 and 4.5 respectively. NZ3 remains neutral in charge throughout the pH range.

4.5.3 Quantification of Au and Ru using ICP-MS characterization. ICP-MS analyses were performed on a Perkin-Elmer NexION 300X ICP mass spectrometer to quanify ^{197}Au and ^{101}Ru. Operating conditions are listed as below: nebulizer flow rate: 0.95 L/min; rf power: 1600 W; plasma Ar flow rate: 18 L/min; dwell time: 50 ms. A series of solutions with gold and ruthenium

(concentration: 0, 0.2, 0.5, 1, 2, 5, 10, and 20 ppb) were prepared for calibration. Nanozyme solutions were diluted in water to 200 nM. 10 μL sample solution was transferred to 15 mL centrifuge tubes. 0.5 mL of fresh *aqua regia* was added to each sample including the standard samples and was diluted to 10 mL with de-ionized water.

Sample Preparation: was added to the 10 μL sample solution and then the sample was diluted to 10 mL with de-ionized water.

	Au (ng)	Ru (ng)	Ru(ng)/ AuNP (pmol)	Ru/AuNp
NZ 1	238.367	11.380	2.257	
	239.175	11.442	2.408	
	234.014	11.946	2.565	23.850
NZ 2	235.474	10.918	2.187	
	242.668	12.273	2.531	
	239.170	11.290	2.450	23.644
NZ 3	229.469	10.845	2.193	
	231.307	11.718	2.466	
	231.790	12.253	2.687	24.230

Figure 4.7. Ruthenium amount in the nanozymes using ICP-MS measurement. The Catalyst/NP represents number of Ruthenium catalysts encapsulated per gold nanoparticle.

4.5.4 Nanozyme catalysis in solution at different pH. Allylcarbamate protected Rhodamine 110 (alloc-Rho) was used as a substrate to test the catalytic activity of the nanozymes. A solution containing 400 nM nanozyme and 100 μM substrate was prepared in a 96-well plate using buffers with varying pH (3.5-7.4). 400 nM nanozyme solution and 100 μM substrate solutions alone were used as negative controls. The kinetic study was done by tracking the fluorescence intensity (Ex: 488 nm, Em: 521 nm, Cutoff: 515 nm) using a Molecular Devices SpectraMax M2 microplate reader as shown in Figure 4.S4. 5 mM Phosphate buffer were used for pH range (5.5-7.5) and 5mM Citrate buffer for pH range (3.5-4.5).

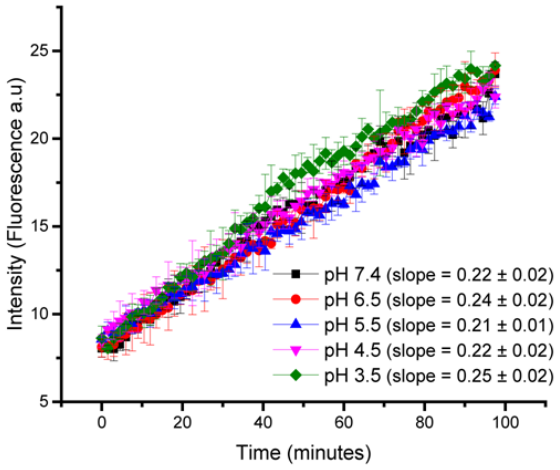

Figure 4.8. Catalysis of NZ1 at different pH for 2 hours at 37 ºC.

4.5.5 Cellular uptake of NZs in 3T3 Fibroblast cells: The cellular uptake experiments were done using previously approved protocols. 30K Fibrobast cell/well were plated in a 24-well plate prior to the experiment. Next day, the cells were washed with PBS and incubated with NZ1 (1 μM) in 10% serum-containing media for 3h at 37 °C. Subsequently, the cells were washed with PBS (3 times) and then subjected to lysis buffer. The lysed cells were then further processed for ICP-MS analysis as shown in Figure 4.S5. These experiments were performed independently two times and each experiment was comprised of 3 replicates.

4.5.6 Sample preparation for ICP-MS and ICP-MS instrumentation: Samples were prepared using previously reported protocols. The cells were lysed by a lysis buffer and were transferred to 15 mL centrifuge tubes. A series of standard solutions of gold and ruthenium (0, 0.2, 0.5, 1, 2, 5, 10, and 20 ppb) were prepared for calibration. 0.5 mL of fresh *aqua regia* were added to each sample including the standard samples and were diluted to 10 mL with de-ionized water. ^{197}Au and ^{101}Ru quantification were done on a Perkin-Elmer NexION 300X ICP mass spectrometer under standard mode. Operating conditions are listed as below: nebulizer flow rate: 0.95-1 L/min; rf power: 1600 W; plasma Ar flow rate: 18 L/min; dwell time: 50 ms.

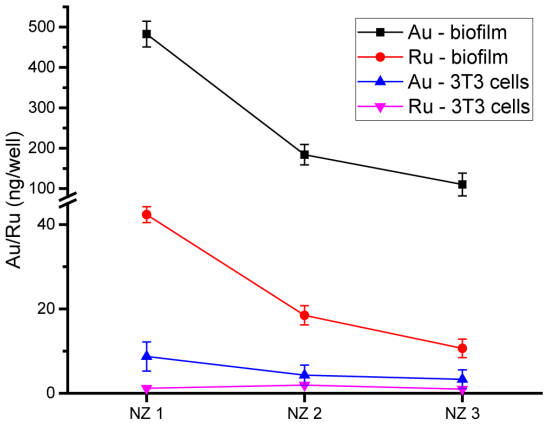

Figure 4.9. Nanoparticle and catalyst uptake in P. aeruginosa (CD-1006) biofilms and NIH-3T3 Fibroblast cells after incubation for 1 hour in pH 7.4 (cell culture media with 10% serum) with NZ1 (400 nM), as measured by ICP-MS.

4.5.7 Confocal imaging of 4 different strains: We used the same procedure for imaging biofilms as described in the materials and methods section of the manuscript in Figure 4.S6.

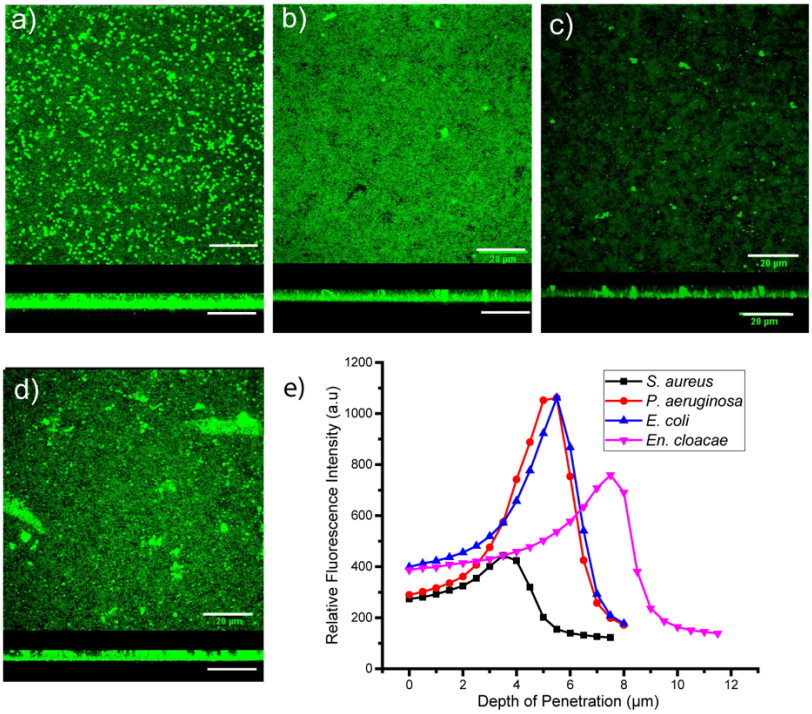

Figure 4.10. Confocal microscopy images of a. CD-489 (*S. aureus*, a methicillin resistant strain), b. CD-1006 (*P. aeruginosa*), c. CD-2 (*E. coli*) and d. CD-1412 (*En. cloacae*) treated with nanozymes (NZ1) and pro-rhodamine. The panels are projections at 0º and 90º angle turning along Y-axis. The scale bars are 20 μm. e) Integrated intensity of Rhodamine 110 after 1-hour incubation with NZ1. The x-axis is the depth of penetration of biofilms, where 0 μm represents the top layer. The y-axis is the integrated intensity of the fluorescence resulted from the deprotection of Alloc-Rho.

4.5.8 Data analysis of confocal images. The data analysis of the confocal images was done using the previously reported procedure.[40,41] Briefly, confocal images obtained were analyzed using ImageJ software. After opening the file in ImageJ, the site of interest was selected using drawing selection tool (rectangle). Next, from the analyze menu, "set measurements" was selected for determining Area, Integrated density and mean grey value. To obtain final cell/biofilm fluorescence, the following formula was used -:

CTCF = Integrated Density – (Area of selected location × Mean fluorescence of background readings)

An example for the data points obtained for image analysis can be explained using Figure S7. Box 1 represents the background, box 2 represents the site for cells only and box 3 represents biofilm-mammalian cell coculture in Figure 4.S7. The fluorescence calculated for cells only and biofilms was done by selecting 50 similar data points and averaging the results obtained for all them.

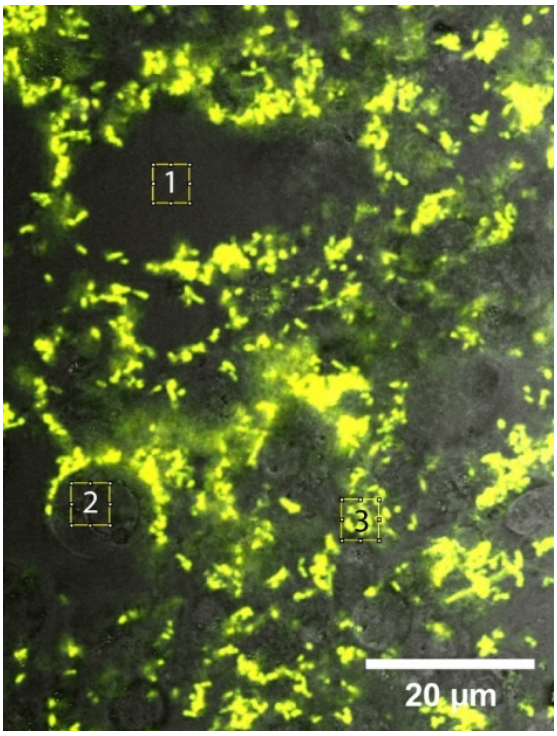

Figure 4.11. Image showing an example of sites used for image analysis of biofilm-mammalian cell co-culture models. Box 1, 2, 3 represents background, cells only and biofilm-cells respectively.

4.6 References

1. FY15 Detect and Protect Against Antibiotic Resistance Budget Initiative; Centers for Disease Control and Prevention: Atlanta, GA, 2003, http://www.cdc.gov/drugresistance/ threat-report-2013/pdf/FY15-DPAR-budget-init.pdf.

2. Lewis, K. Persister Cells, Dormancy and Infectious Disease. *Nat Rev Micro* **2007**, *5*, 48–56.

3 . Hall-Stoodley, L.; Costerton, J. W.; Stoodley, P. Bacterial Biofilms: From the Natural Environment to Infectious Diseases. *Nat. Rev. Microbiol.* **2004**, *2*, 95–108.

4. Bjarnsholt, T. The Role of Bacterial Biofilms in Chronic Infections. *Apmis* **2013**, *121*, 1–58.

5. Costerton, J. W.; Post, J. C.; Ehrlich, G. D.; Hu, F. Z.; Kreft, R.; Nistico, L.; Kathju, S.; Stoodley, P.; Hall-Stoodley, L.; Maale, G.; James, G.; Sotereanos, N.; DeMeo, P. New Methods for the Detection of Orthopedic and Other Biofilm Infections. *FEMS Immunol. Med. Microbiol.* **2011**, *61*, 133–140.

6. van Oosten, M.; Schäfer, T.; Gazendam, J. A. C.; Ohlsen, K.; Tsompanidou, E.; de Goffau, M. C.; Harmsen, H. J. M.; Crane, L. M. A; Lim, E.; Francis, K. P.; Cheung, L.; Olive, M.; Ntziachristos, V.; Dijl, J. M. V.; Dam, G. M.V. Real-Time in Vivo Imaging of Invasive- and Biomaterial-Associated Bacterial Infections Using Fluorescently Labelled Vancomycin. *Nat. Commun.* **2013**, *4*, 2584.

7. Love, C.; Tomas, M. B.; Tronco, G. G.; Palestro, C. J. FDG PET of Infection and Inflammation. *Radiographics* **2005**, *25*, 1357–1368.

8. Ning, X.; Lee, S.; Wang, Z.; Kim, D.; Stubblefield, B.; Gilbert, E.; Murthy, N. Maltodextrin-Based Imaging Probes Detect Bacteria in Vivo with High Sensitivity and Specificity. *Nat Mater* **2011**, *10*, 602–607.

9. Leevy, W. M.; Gammon, S. T.; Jiang, H.; Johnson, J. R.; Maxwell, D. J.; Jackson, E. N.; Marquez, M.; Piwnica-Worms, D.; Smith, B. D. Optical Imaging of Bacterial Infection in Living Mice Using a Fluorescent near-Infrared Molecular Probe. *J. Am. Chem. Soc.* **2006**, *128*, 16476–16477.

10. Hall-Stoodley, L.; Stoodley, P.; Kathju, S.; Høiby, N.; Moser, C.; William Costerton, J.; Moter, A.; Bjarnsholt, T. Towards Diagnostic Guidelines for Biofilm-Associated Infections. *FEMS Immunol. Med. Microbiol.* **2012**, *65*, 127–145.

11. Sauer, K.; Camper, A. K.; Ehrlich, G. D.; Costerton, J. W.; Davies, D. G. Pseudomonas Aeruginosa Displays Multiple Phenotypes during Development as a Biofilm. *J. Bacteriol.* **2002**, *184*, 1140–1154.

12. Hall-Stoodley, L.; Hu, F. Z.; Gieseke, A.; Nistico, L.; Nguyen, D.; Hayes, J.; Forbes, M.; Greenberg, D. P.; Dice, B.; Burrows, A.; et al. Direct Detection of Bacterial Biofilms on the Middle-Ear Mucosa of Children with Chronic Otitis Media. *JAMA*, *J. Am. Med. Assoc.* **2006**, *296*, 202–211.

13. Sasser, T. A.; Avermaete, A. E. Van; White, A.; Chapman, S.; Johnson, J. R.; Avermaete, T. Van; Gammon, S. T.; Leevy, W. M.; Health, C.; Imaging, M. Bacterial Infection Probes and

Imaging Strategies in Clinical Nuclear Medicine and Preclinical Molecular Imaging. *Curr. Top. Med. Chem.* **2013**, *13*, 479–487.

14. T Neu, T. R.; Swerhone, G. D. W.; Lawrence, J. R. Assessment of Lectin-Binding Analysis for in Situ Detection of Glycoconjugates in Biofilm Systems. *Microbiology* **2001**, *147*, 299–313.

15. Bjarnsholt, T.; Alhede, M.; Alhede, M.; Eickhardt-Sørensen, S. R.; Moser, C.; Kühl, M.; Jensen, P. Ø.; Høiby, N. The in Vivo Biofilm. *Trends Microbiol.* **2013**, *21*, 466–474.

16. Fux, C. a; Stoodley, P.; Hall-Stoodley, L.; Costerton, J. W. Bacterial Biofilms: A Diagnostic and Therapeutic Challenge. *Expert Rev. Anti. Infect. Ther.* **2003**, *1*, 667–683.

17. Anderl, J. N.; Franklin, M. J.; Stewart, P. S. Role of Antibiotic Penetration Limitation in Klebsiella Pneumoniae Biofilm Resistance to Ampicillin and Ciprofloxacin. *Antimicrob. Agents Chemother.* **2000**, *44*, 1818–1824.

18. Stewart, P. S.; Costerton, J. W. Antibiotic Resistance of Bacteria in Biofilms. *Lancet* **2001**, *358*, 135–138.

19. Li, X.; Yeh, Y.-C.; Giri, K.; Mout, R.; Landis, R. F.; Prakash, Y. S.; Rotello, V. M. Control of Nanoparticle Penetration into Biofilms through Surface Design. *Chem. Commun.* **2015**, *51*, 282–285.

20. Peulen, T. O.; Wilkinson, K. J. Diffusion of Nanoparticles in a Biofilm. *Environ. Sci. Technol.* **2011**, *45*, 3367–3373.

21. Gupta, A.; Landis, R. F.; Rotello, V. M. Nanoparticle-Based Antimicrobials: Surface Functionality Is Critical. *F1000Research* **2016**, *5*, 1–10.

22. Benoit, D. S. W.; Koo, H. Targeted, Triggered Drug Delivery to Tumor and Biofilm Microenvironments. *Nanomedicine* **2016**, *11*, 873–879.

23. Horev, B.; Klein, M. I.; Hwang, G.; Li, Y.; Kim, D.; Koo, H.; Benoit, D. S. W. PH-Activated Nanoparticles for Controlled Topical Delivery of Farnesol to Disrupt Oral Biofilm Virulence. *ACS Nano* **2015**, *9*, 2390–2404.

24. Moriarty, T. F.; Elborn, J. S.; Tunney, M. M. Effect of pH on the Antimicrobial Susceptibility of Planktonic and Biofilm-Grown Clinical Pseudomonas Aeruginosa Isolates. *Br. J. Biomed. Sci.* **2007**, *64*, 101–104.

25. Mizuhara, T.; Saha, K.; Moyano, D. F.; Kim, C. S.; Yan, B.; Kim, Y. K.; Rotello, V. M. Acylsulfonamide-Functionalized Zwitterionic Gold Nanoparticles for Enhanced Cellular Uptake at Tumor pH. *Angew. Chemie - Int. Ed.* **2015**, *54*, 6567–6570.

26. Das, M.; Sanson, N.; Kumacheva, E. Zwitterionic Poly(betaine-N-Isopropylacrylamide) Microgels: Properties and Applications. *Chem. Mater.* **2008**, *20*, 7157–7163.

27. Madura, J. D.; Lombardini, J. B.; Briggs, J. M.; Minor, D. L.; Wierzbicki, A. Physical and Structural Properties of Taurine and Taurine Analogues. *Amino Acids* **1997**, *13*, 131–139.

28. Tonga, G. Y.; Jeong, Y.; Duncan, B.; Mizuhara, T.; Mout, R.; Das, R.; Kim, S. T.; Yeh, Y.-C.; Yan, B.; Hou, S.; Rotello, V.M. Supramolecular Regulation of Bioorthogonal Catalysis in Cells Using Nanoparticle-Embedded Transition Metal Catalysts. *Nat. Chem.* **2015**, *7*, 597–603.

29. Yusop, R. M.; Unciti-Broceta, A.; Johansson, E. M.; Sanchez-Martin, R. M.; Bradley, M. Palladium-Mediated Intracellular Chemistry. *Nat Chem* **2011**, *3*, 239–243.

30. Oliver, A.; Canton, R.; Campo, P.; Baquero, F.; Blazquez, J.; Cantón, R.; Campo, P.; Baquero, F.; Blázquez, J. High Frequency of Hypermutable Pseudomonas Aeruginosa in Cystic Fibrosis Lung Infection. *Science* **2000**, *288*, 1251–1253.

31. Nickel, J. C.; Ruseska, I.; Wright, J. B.; Costerton, J. W. Tobramycin Resistance of Pseudomonas Aeruginosa Cells Growing as a Biofilm on Urinary Catheter Material. *Antimicrob. Agents Chemother.* **1985**, *27*, 619–624.

32. Yun, S.-W.; Leong, C.; Zhai, D.; Tan, Y. L.; Lim, L.; Bi, X.; Lee, J.-J.; Kim, H. J.; Kang, N.-Y.; Ng, S. H.; *et al.* Neural Stem Cell Specific Fluorescent Chemical Probe Binding to FABP7. *Proc. Natl. Acad. Sci.* **2012**, *109*, 10214–10217.

33. Costerton, W.; Veeh, R.; Shirtliff, M.; Pasmore, M.; Post, C.; Ehrlich, G. The Application of Biofilm Science to the Study and Control of Chronic Bacterial Infections. *J. Clin. Invest.* **2003**, *112*, 1466–1477.

34. Anderson, G. G.; Moreau-Marquis, S.; Stanton, B. A.; O'Toole, G. A. In Vitro Analysis of Tobramycin-Treated Pseudomonas Aeruginosa Biofilms on Cystic Fibrosis-Derived Airway Epithelial Cells. *Infect. Immun.* **2008**, *76*, 1423–1433.

35. Anderson, G. G.; Kenney, T. F.; Macleod, D. L.; Henig, N. R.; O'Toole, G. A. Eradication of Pseudomonas Aeruginosa Biofilms on Cultured Airway Cells by a Fosfomycin/tobramycin Antibiotic Combination. *Pathog. Dis.* **2013**, *67*, 39–45.

36. Landis, R. F.; Gupta, A.; Lee, Y.-W.; Wang, L.-S.; Golba, B.; Couillaud, B.; Ridolfo, R.; Das, R.; Rotello, V. M. Crosslinked Polymer-Stabilized Nanocomposites for the Treatment of Bacterial Biofilms. *ACS Nano* **2016**, *11*, acsnano.6b07537.

37. Gupta, A.; Saleh, N. M.; Das, R.; Landis, R. F.; Bigdeli, A.; Motamedchaboki, K.; Rosa Campos, A.; Pomeroy, K.; Mahmoudi, M.; Rotello, V. M. Synergistic Antimicrobial Therapy Using Nanoparticles and Antibiotics for the Treatment of Multidrug-Resistant Bacterial Infection. *Nano Futur.* **2017**, *1*, 15004-15009.

38. You, C.-C.; Miranda, O. R.; Gider, B.; Ghosh, P. S.; Kim, I.-B.; Erdogan, B.; Krovi, S. A.; Bunz, U. H. F.; Rotello, V. M. Detection and Identification of Proteins Using Nanoparticle-Fluorescent Polymer "Chemical Nose" Sensors. *Nat. Nanotechnol.* **2007**, 2, 318–323.

39. Gupta, A.; Saleh, N. M.; Das, R.; Landis, R. F.; Bigdeli, A.; Motamedchaboki, K.; Rosa Campos, A.; Pomeroy, K.; Mahmoudi, M.; Rotello, V. M. Synergistic Antimicrobial Therapy Using Nanoparticles and Antibiotics for the Treatment of Multidrug-Resistant Bacterial Infection. *Nano Futur.* **2017**, *1*, 15004-15009.

40. Burgess, A.; Vigneron, S.; Brioudes, E.; Labbé, J.-C.; Lorca, T.; Castro, A. Loss of Human Greatwall Results in G2 Arrest and Multiple Mitotic Defects due to Deregulation of the Cyclin B-Cdc2/PP2A Balance. *Proc. Natl. Acad. Sci. U. S. A.* **2010**, *107*, 12564–12569.

41. McCloy, R. A.; Rogers, S.; Caldon, C. E.; Lorca, T.; Castro, A.; Burgess, A. Partial Inhibition of Cdk1 in G2 Phase Overrides the SAC and Decouples Mitotic Events. *Cell Cycle* **2014**, *13*, 1400–1412.

CHAPTER 5

RBC-MEDIATED DELIVERY OF BIOORTHOGONAL NANOZYMES FOR SELECTIVE TARGETING OF BACTERIAL INFECTIONS

5.1 Introduction

Bioorthogonal catalysis offers a strategy for chemical transformations complementary to bioprocesses and has proven to be a powerful tool in biochemistry and medical sciences.[1-3] Nanoparticles embedded with transition metal catalysts (nanozymes) have demonstrated excellent ability to catalyze reactions beyond the capabilities of biological systems.[4,5] Nanozymes can implement bioorthogonal approach to chemically transform a biologically inert substrate to its active form at the site of interest.[6,7] Localization of bio-orthogonal nanozymes at targeted biological site is central in maximizing the efficacy of the strategy.[8,9] One approach to control spatiotemporal localization of biorthogonal catalysts utilizes tuning the size of carrier.[10,11] Alternatively, biorthogonal catalysts can be functionalized with different ligands, peptides or biomolecules to target the diseased physiological site.[7,8] However, these synthetic carrier-based approaches are susceptible to non-specific uptake and potential degradation of vehicles in macrophages, compromising the efficacy of therapy.[12,13]

Red blood cells (RBCs) have been used as cell-based drug delivery systems owing to their biocompatibility, long circulation time and low immunogenicity.[14-16] RBCs are significantly hemolyzed by bacterial toxins, providing these RBC carriers with intrinsic targeting ability towards pathogenic bacteria.[17-19] Moreover, high surface to volume ratio of RBCs provides an ideal surface for hitchhiking of nanoparticles through supramolecular interactions with RBC cell surface. Recent studies have demonstrated that RBC-hitchhiking of NPs enhanced the delivery efficacy to the target organs with minimal non-specific uptake by the reticuloendothelial system.[20,21]

Notably, maintaining the stability of RBC membranes is critical in retaining the biocompatibility and immune-evading ability of NP-hitchhiked RBCs. Surface functionality of NPs

dictates their interaction with RBCs and is key to generate RBC "super-carriers" as effective drug delivery systems.[22] For example, cationic NPs can bind to the anionic glycocalyx on RBC cell surface.[23] Similarly, NPs can also bind to hydrophobic domains present on RBC's plasma membranes irrespective of NP surface charge.[24] Moreover, tuning hydrophilic and hydrophobic moieties on NP-surface can significantly impact the hemolysis caused by NPs.[25]

We hypothesized that integration of "super-carrier" RBCs with bioorthogonal nanozymes would offer a novel route to combat bacterial infections while minimizing the possible off-target effects. Here, we have designed a series of nanozymes that feature diverse functional groups with different binding ability to RBCs. The structure-activity studies revealed that hydrophilic cationic NZs can stably attach onto RBC surface, resulting in formation of RBC-hitchhiked nanozymes (RBC-NZs). Subsequently, these RBCs were hemolyzed by bacterial toxins, resulting in accumulation of nanozymes at the site of bacterial infection. These NZs activated protected-antibiotic molecules and effectively eradicate biofilms formed by uropathogenic bacteria, whereas minimal toxicity was observed against non-virulent bacterial strains. Moreover, RBC-NZs showed minimal uptake in macrophage cells as opposed to free nanozymes, suggesting that nanozyme hitchhiking does not compromise the immune-evading ability of RBCs. Overall, we have generated RBC-hitchhiked nanozymes illustrating the ability of passively targeting bacterial infections triggered by bacterial toxins while minimizing non-selective killing of bacteria.

5.2 Results and discussion

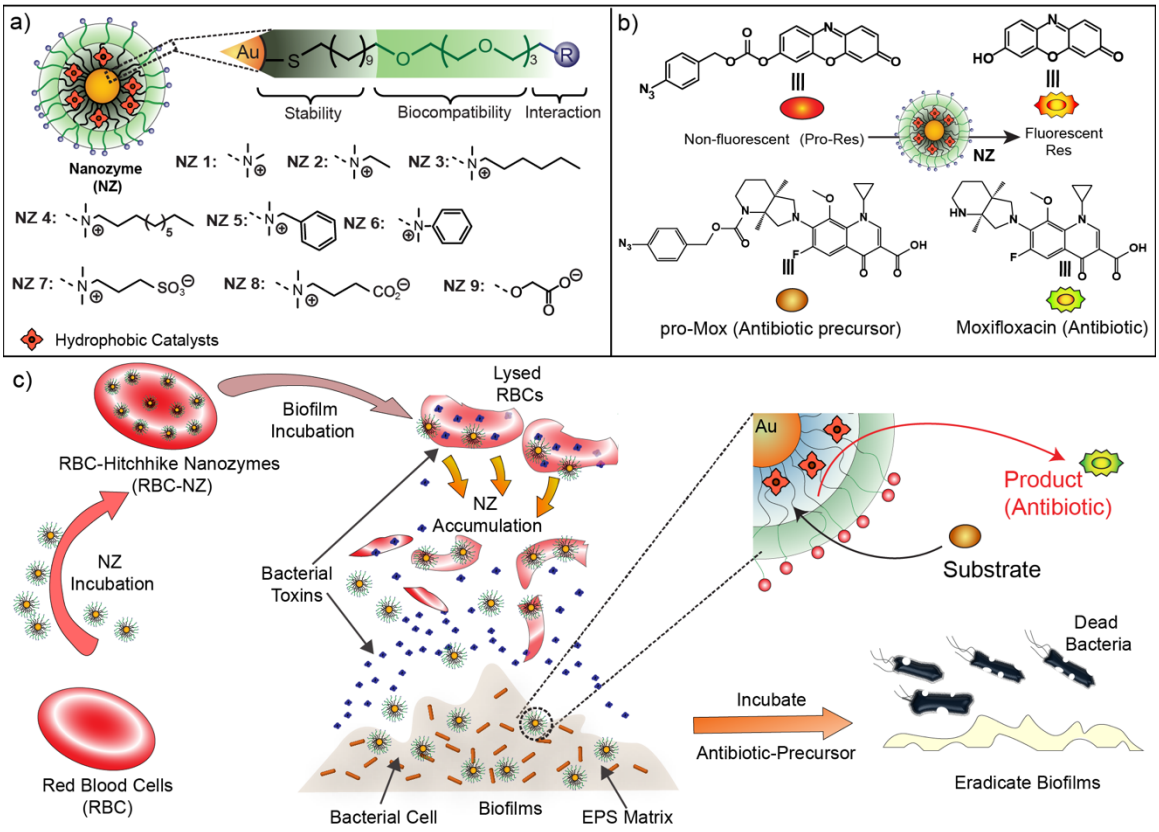

Figure 5.1. a) Molecular structures of the ligand structures used on nanozymes used in the RBC-adsorption study. b) Structures of the substrates Resorufin and moxicillin derivative (Pro-Res, Pro-Mox) and products (Resorufin, Moxifloxacin) after cleavage by TMC c) Schematic representation showing hitchhiking of NZs on Red Blood Cells, selective targeting of biofilms infections due to lysis of RBCs in presence of bacterial toxins and intrabiofilm generation of antibiotics by transition metal catalysts (TMCs) embedded in the nanoparticle monolayers.

Nanozymes were fabricated using AuNPs with ~ 2 nm core diameter as scaffolds. AuNPs were functionalized with ligands featuring three main components: (1) a hydrophobic alkyl chain interior enabling encapsulation of hydrophobic catalysts, (2) tetra ethylene glycol spacer providing biocompatibility and (3) terminal groups dictating NP-binding with Red Blood Cells.[26] Aqueous solution of AuNPs was mixed with catalysts (iron (III) tetraphenyl porphyrin (FeTPP)) dissolved in organic solvents in 1:1 ratio (% v/v). The mixture was slowly evaporated to remove organic solvents, resulting in encapsulation catalysts in the surface monolayer of AuNPs to form nanozymes (NZs). Excess catalyst was filtered out by using molecular-weight cut-off filter,

centrifugal filter and dialysis (experimental details are provided in methods section).[27]The chemical functionality of NZ-surface ligands plays a critical role in determining their compatibility with RBCs, in-turn dictating ability of NZs to hitchhike on RBC surface.[20,23] We synthesized a family of NPs (1-9) with varying surface charge, hydrophobicity and aromatic properties using ligand place exchange reactions with pentanethiol-capped 2 nm Au core (detailed description for synthesis of NPs is described in Supporting Information). NPs (1-9) were used to fabricate NZs (1-9) and characterized using dynamic light scattering (DLS) (Figure 5.S1, Table 5.S1) and transmission electron microscopy (TEM, Figure 5.S2). TEM and DLS results showed no signs of aggregation of NZs upon catalyst encapsulation. The number of catalysts encapsulated were quantified using inductively coupled mass spectrometry (ICP-MS, Table 5.S2), indicating that 30±6 catalyst molecules were encapsulated per AuNP for NZ 1-9.

Our initial focus was to adsorb NZs on RBCs without compromising the stability of cell membrane, hence we screened the library of NZs for hemolytic activity against RBCs both in PBS and serum-containing media. NZs (1-9) were incubated with RBCs for 30 minutes and the absorbance of released hemoglobin was measured at 570 nm.[28] We observed that cationic hydrophilic NZs (NZ 1-2) showed minimal hemolysis as compared to their hydrophobic counterparts. Similarly, anionic and zwitterionic NZs (NZ 7-9) showed minimal hemolysis of RBCs (Figure 5.2a, 5.S3), consistent with previously reported studies.[25] Next, we studied the adsorption of non-hemolytic NZs (NZ1-2, NZ7-9) on RBCs to determine their suitability for RBC hitchhiking. NZs were incubated with RBCs for 30 minutes and washed to remove excess NZs. The harvested RBCs were then analyzed using ICP-MS to quantify gold content on the cells. Cationic NZs showed significant adsorption on RBCs as compared to the anionic and zwitterionic NZs (Figure 5.2b), attributed to electrostatic interactions between NZs and RBCs.

Nanoparticles can frequently detach from RBCs due to shear force and lose their targeting ability.[24] Hence, we further investigated the stability of NZs hitchhiked on RBCs by subjecting these RBC-NZs to multiple washing and centrifuging cycles. No significant difference in Au

content was observed even after 5 centrifuging cycles, indicating that NZs remain attached to RBCs (Figure 5.2c). Adsorption of NZ 1 on RBCs was further investigated at a reduced incubation time of 30 minutes (Figure 5.2d). The catalytic activity of RBC-NZs was assessed by fluorometric measurement of resorufin molecule fragmented from the non-fluorescent pro-Res (Figure 5.1b) due to azide reduction by FeTTP catalyst in presence of glutathione (1 mM).[29] Linear increase in the fluorescence indicate that NZs retain their catalytic activity even after adsorption on RBCs. The rate of fluorescence increase was similar for free NZs as compared to RBC-NZs (500 nM). Moreover, catalytic rate of RBC-NZs increased linearly with increasing concentration of RBC-NZs (50-100 nM) as seen in Figure 5.2e. RBC-NZs incubated with pro-Res and glutathione were visualized under confocal microscope, further indicating that RBC-NZs retain their catalytic activity.

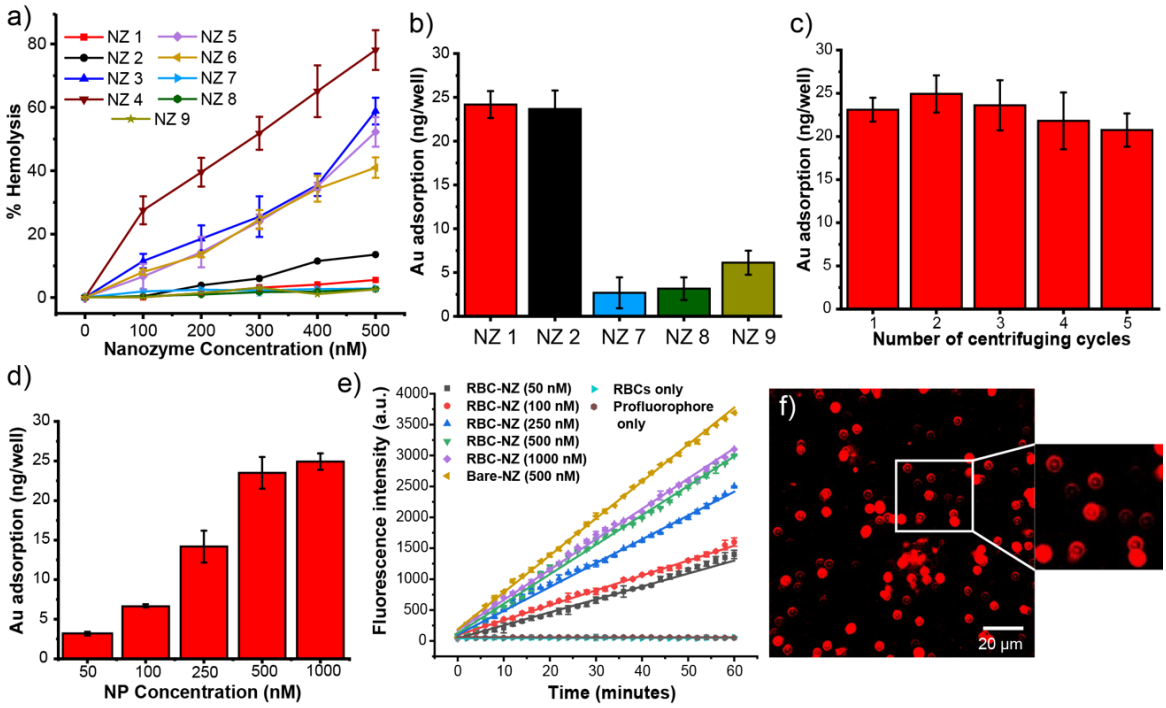

Figure 5.2. a) Dose-dependent hemolytic activity of NZ 1–NZ 9 in the absence of plasma proteins. % hemolysis was calculated using water as the positive control. Error bars represent standard deviations (n = 3). Amount of NZ adsorption on Red Blood Cells after b) incubation for 30 minutes c) after multiple cycles of centrifugation, at a concentration of 500 nM, as measured using ICP-MS. Dose dependent d) hemolytic activity of NZ 1 for 10^7 Red Blood Cell/mL, e) NZ adsorption for NZ 1 for 10^7 Red Blood Cell/mL. f) Catalysis of free nanozymes and RBC-NZs in PBS for 1 h at 37 °C.

RBCs lose their prolonged circulation upon damage to RBC plasma membrane such as those caused by pore-forming toxins (PFTs).[16,19] Infections caused by bacteria often involve secretion of pore-PFTs as a virulence mechanism.[30,31] These toxins disrupt the host-cell membrane for pathogenesis, in particular causing high hemolysis of RBCs. For example, α-hemolysin toxin released by *S. aureus* and *E. coli* is one of the key virulence factors of the invading strains.[17,32,33] Next, we investigated the hemolysis of RBCs caused by uropathogenic clinical isolates (*E. coli*, methicillin-resistant *S. aureus* (MRSA)) and non-pathogenic laboratory strains (*P. aeruginosa*, *B. sub*). We observed that uropathogenic strains caused complete hemolysis of the RBCs within 30 minutes of incubation with RBCs, whereas the non-pathogenic strains caused minimal hemolysis of RBCs (Figure 5.3a). Having established that cationic hydrophilic NZs can hitchhike onto RBCs and these RBCs were hemolyzed in presence of bacterial infections. We set out to determine whether hemolysis of RBCs could result in selective catalytic activity of RBC-NZs against pathogenic bacterial infections.

Conventional antibiotic-based strategies to combat bacterial infections often disrupt the ecology of human microbiome by killing helpful bacteria species inhabiting the host.[34,35] Hence, it is critical to develop strategies with increased efficacy to target pathogenic infections.[36,37] We investigated the selectivity of RBC-NZs towards virulent biofilms through imaging studies using confocal microscopy. Studies for imaging biofilms were based on generation of fluorophore (Resorufin) through aryl-reduction of non-fluorescent precursor (Pro-Res) as shown in Figure 1b.[26,29] RBC-NZs were incubated with toxin-secreting (Green Fluorescent Protein (GFP) *expressing* methicillin-resistant *Staphylococcus aureus*, MRSA) and non-virulent (GFP *expressing E. coli*) bacterial biofilms for 24 hours. Biofilms were then washed multiple times, followed by 1-hour incubation with substrate and subsequent washings. Uropathogenic biofilms showed bright red fluorescence when observed under confocal, with minimal fluorescence observed in non-pathogenic biofilms (Figure 5.3b). Moreover, the z-stack confocal images demonstrate that NZs

can completely penetrate the EPS matrix of biofilm, indicating their potential as an effective therapeutic strategy.[38]

After establishing selective catalytic activity of RBC-NZs in pathogenic biofilms, we tested the accumulation of RBC-NZs using ICP-MS in pathogenic and non-pathogenic biofilms. We observed that RBC-NZs showed high accumulation in toxin-secreting uropathogenic bacterial biofilms based on Au, whereas minimal amount of Au was observed in non-hemolytic bacterial biofilms (Figure 5.3c), whereas free NZ 1 showed similar accumulation in pathogenic and non-pathogenic biofilms (Figure 5.S4). These results are consistent with our observations indicating pathogenic bacteria cause higher hemolysis of biofilms as compared to their non-pathogenic counterparts. In another experiment, we determined the amount of Au attached to the cell debris upon hemolysis of RBCs to understand the association of NZs with the carrier cells. It was determined that significant number of NZs were released into the solution upon hemolysis of RBCs, whereas NZs remained attached to cell-surface in case of non-hemolyzed RBCs (Figure 5.3d). This phenomenon could be attributed to compromised electrostatic interaction between NZs and RBCs upon lysis of the erythrocyte cells.[39]

After establishing the ability of RBC-NZs to selectively target pathogenic bacterial biofilms, we probed the immunocompatibility of RBC-NZs. RAW 264.7 macrophage cells were incubated with RBC-NZs for 24 hours, followed by washing and addition of pro-Res for 24 hours. It was observed that macrophages incubated with RBC-NZs exhibited minimal fluorescence, whereas macrophages incubated with free NZ 1 (Bare-NZ) showed strong punctate fluorescence due to activation of pro-fluorophore by macrophage uptaken nanozymes (Figure 5.5). Additionally, free NZ 1 (bare-NZ) showed high uptake in macrophages whereas RBC-NZs showed minimal uptake as quantified by ICP-MS (Figure 5.3c, 5.6). These results further suggest that RBC hitchhiking can be used to selectively target pathogenic biofilms while avoiding non-specific uptake by macrophages.

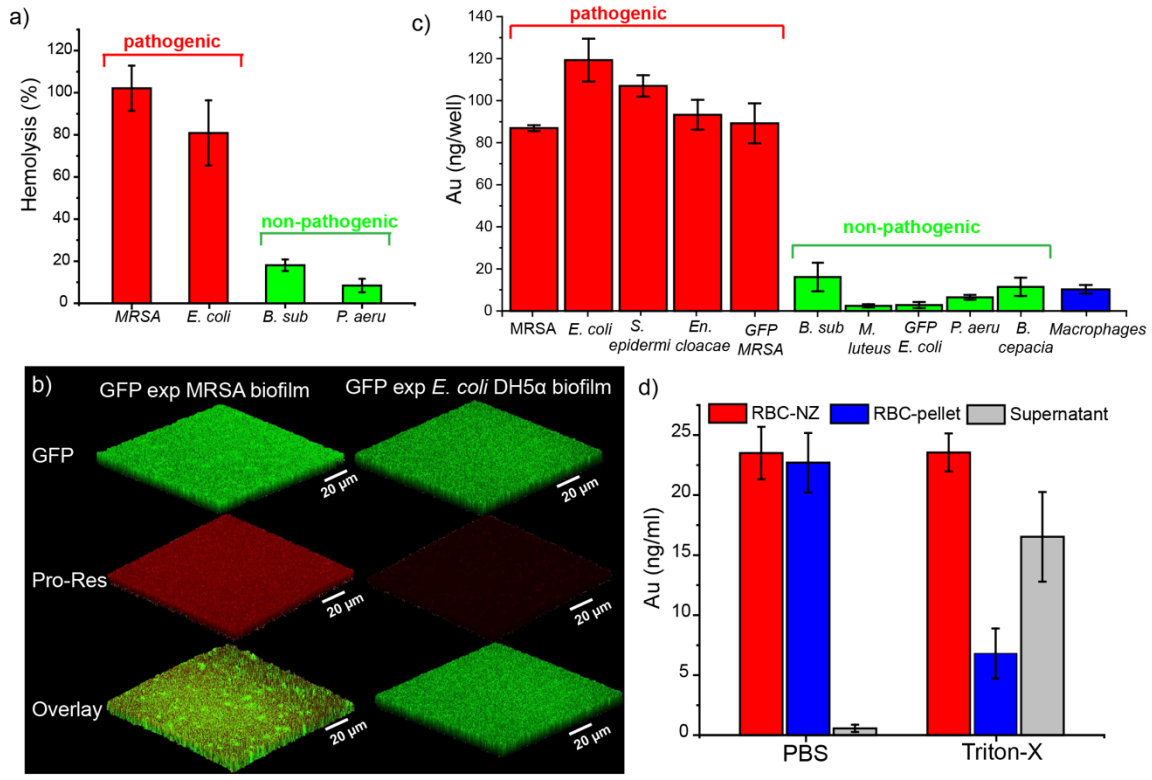

Figure 5.3. a) Hemolysis of Red Blood Cells by bacterial biofilms b) Quantification of Au (ng/well) on RBCs-nanozymes incubated in PBS and Triton-X c) Nanozyme diffusion of Au (ng/well) in different bacterial biofilms including pathogenic (methicillin-resistant *S. aureus*, MRSA and *E. coli*) and non-virulent (*P. aeruginosa* ATCC 17660, *B. Sub* FD6b) biofilms after incubation for 1 day with RBC-NZ (10^7 cell/mL, 100 nM NZ), as measured by ICP-MS. Cellular uptake of Au (ng/well) in macrophage (RAW 264.7) (20,000 cells/well) after incubation for 1 day with RBC-NZ (10^7 cell/mL, 100 nM NZ), as measured by ICP-MS d) Confocal images of biofilms incubated with RBC-NZs (1 h) followed by incubation with Pro-Res (1 h, 10 μM).

After establishing the localization of NZs at the site of pathogenic bacteria, we investigated the ability of RBC-NZs to selectively activate antibiotic-precursor and eradicate pathogenic bacterial biofilms. For this study, aryl azide protected moxifloxacin (pro-Mox) was chosen as a model pro-antibiotic due to the high clinical relevance of moxifloxacin in the treatment of MDR infections.[40] The synthetic protection of secondary amine group on moxifloxacin inhibits them to bind with target bacterial enzymes, inhibiting their antimicrobial activity prior to activation.[41] Alamar Blue assays were performed on biofilms treated with RBC-NZs and pro-Mox to determine biofilm viability.

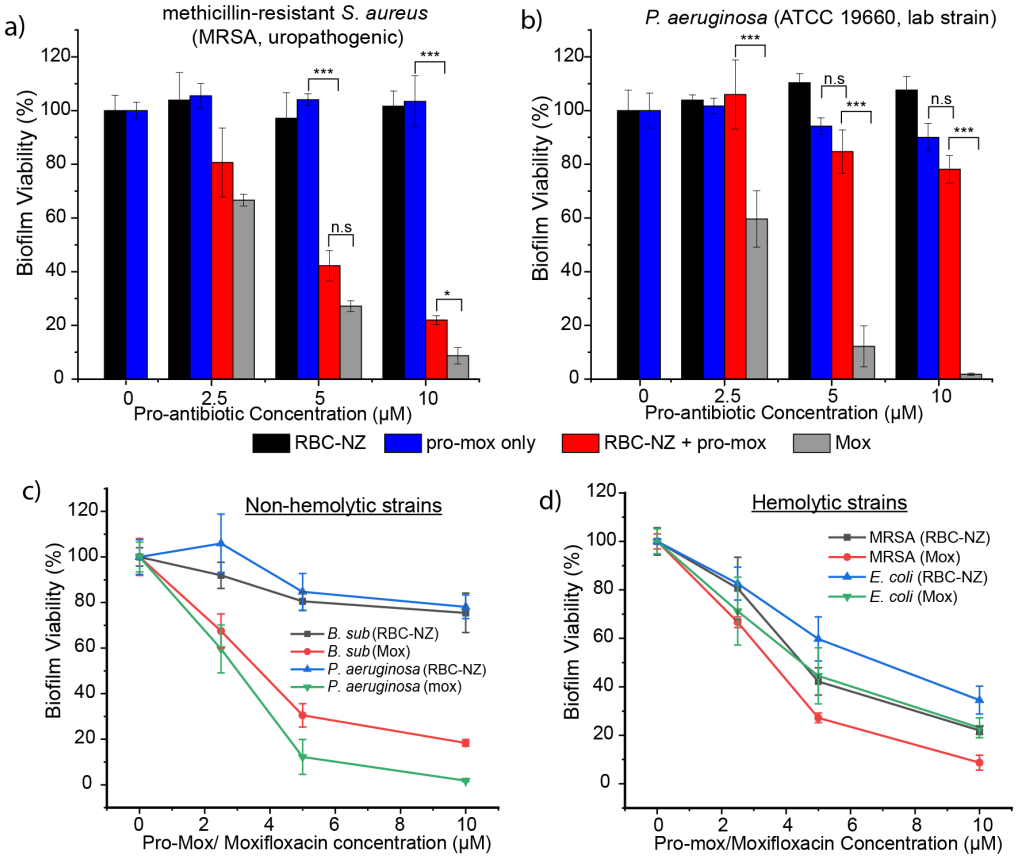

Figure 5.4. Deprotection of antimicrobials in biofilms using RBC-hitchhiked nanozymes. RBC-NZ was used for selective activation of antibiotic prodrugs that decrease biofilms viability. a) *E. coli* (toxin producing) biofilms and b) *B. sub* (non-virulent) biofilms treated with pro-Mox and RBC-NZ (red bars) at 37 °C. Biofilms treated only with pro-Mox (blue bars) or with Mox (grey bars) were used in all experiments as negative and positive controls, respectively. Biofilm viability of c) hemolytic (pathogenic) and d) non-pathogenic bacterial strains after treatment with RBC-NZ and pro-Mox and moxifloxacin antibiotic alone. Each experiment was replicated five times. Error bars represent standard deviations of these measurements. *$p < 0.05$, ***$p < 0.001$

We chose methicillin-resistant *S. aureus* (MRSA) and *E. coli* for biofilm viability studies due to their high clinical relevance and pathogenicity caused by α-hemolysin toxin secreted by these species.[17,18,36] Non-pathogenic bacterial strains of *P. aeruginosa*, *B. sub* were used as models strains to study the effect of RBC-NZs on non-hemolytic strains. Biofilms were incubated with RBC-NZs (500 nM) for 24 hours, washed and subsequently incubated with different concentrations of pro-Mox for 24 hours (more details are provided

in methods section). Cells incubated with only pro-Mox and moxifloxacin antibiotics were used as negative and positive controls respectively (Figures 5.4, 5.S7, 5.S8). It was observed that pro-Mox did not reduce biofilm viability against both pathogenic and non-pathogenic biofilms. However, pro-Mox incubated with RBC-NZs showed reduced biofilm viability of pathogenic biofilms while no significant antimicrobial activity was observed against non-pathogenic biofilms. These results indicate that selective accumulation of NZs in pathogenic biofilms enabled catalytic activation of pro-antibiotics thereby increasing the specificity of the therapy. Moreover, moxifloxacin reduced bacterial viability of both pathogenic and non-pathogenic species, indicating the non-selective bacteria killing caused by antibiotic treatment.

5.3 Conclusions

Taken together, we have developed a strategy that integrates natural carrier RBCs with biomimetic nanozymes, providing a platform to perform abiotic chemical reactions with targeting ability in physiological conditions. In this study, we have utilized RBC-hitchhiked nanozymes to selectively eradicate pathogenic bacterial infections. RBCs are hemolyzed in presence of toxins secreted by pathogenic bacteria resulting in selective accumulation of nanozymes at the site of infection. These accumulated nanozymes can subsequently activate antibiotics at the diseased site and eradicate pre-formed biofilms, without harming non-virulent bacterial species. Moreover, RBC-hitchhiked nanozymes show minimal immune response strengthening their claim as a potent *in vivo* therapeutic. With the ability to act as inactive reservoirs this strategy can be particularly useful in treating recurring bacterial infections including chronic wounds and medical device associated infections. This strategy can be further explored to activate multiple therapeutic molecules at the targeted site to combat complex infections and promote healing of the surrounding tissue simultaneously. Combining RBCs with engineered nanozymes provides a platform with

controlled and potentially “incessant” therapeutic loading while circumventing the limitations associated with delivery of nanovehicles. Modular nature of this approach makes it suitable for numerous imaging and therapeutic applications for diverse range of diseases.

5.4 Experimental methods

5.4.1 NP synthesis. 2nm diameter gold nanoparticles were synthetized by the Brust-Schiffrin two-phase methodology using pentanethiol as the stabilizer; these clusters were purified with successive extractions with ethanol and acetone. A Murray place exchange reaction was carried out in dry DCM to functionalize the nanoparticles with each ligand.[42,43] The monolayer-protected nanoparticles were redispersed in water and the excesses of ligand/pentanethiol were removed by dialysis using a 10,000 MWCO snake-skin membrane. The final concentration was measured by UV spectroscopy on a Molecular Devices SpectraMax M2 at 506 nm according to the reported methodology.[44]

5.4.2 Hemolysis assay. Hemolysis assay was performed on human red blood cells as we described in previous study.[45] Briefly, citrate-stabilized human whole blood (pooled, mixed gender) was purchased from Bioreclamation LLC, NY. The red blood cells were purified and re-suspended in 10 mL phosphate buffered saline as soon as received. 0.1 mL of RBC solution was added to 0.4 mL of NP solution in PBS in 1.5 mL centrifuge tube.

The mixture was incubated at 37 ˚C, 150 rpm for 30 minutes followed by centrifugation at 4000 rpm for 5 minutes. The absorbance value of the supernatant was measured at 570 nm with absorbance at 655 nm as a reference. RBCs incubated with PBS as well as water were used as negative and positive control, respectively. All samples were prepared in triplicate. The percent hemolysis was calculated using the following formula:

% Hemolysis = ((sample absorbance-negative control absorbance)) / ((positive control absorbance-negative control absorbance)) × 100.

5.4.3 Biofilm culture. Bacteria were inoculated in LB broth at 37 °C until stationary phase. The cultures were then harvested by centrifugation and washed with 0.85% sodium chloride solution three times. Concentrations of resuspended bacterial solution were determined by optical density measured at 600 nm. Seeding solutions were then made in minimal media, M9 broth to reach OD600 of 0.1. Then, 500 μL of the seeding solutions was added to each well of the 24-well microplate. M9 medium without bacteria was used as a negative control. The plates were covered and incubated at room temperature under static conditions for a desired period of 24 h. Planktonic bacteria were removed by washing with phosphate-buffered saline (PBS) three times.

5.4.4 Nanozyme accumulation in biofilms. After plating bacterial cells in a 24-well plate. On the following day, planktonic bacteria were removed by washing with PBS three times and incubated with RBC-NZ, Bare-NZ (10^7 RBC/ml, 500 nM respectively) in minimal M-9 media (pH 7.4) for 1 h at 37 °C. After incubation, biofilms were washed three times with PBS, and lysis buffer was added to each well. All lysed samples were then further processed for ICP-MS analysis (vide inf ra) to determine the intracellular amount of gold and ruthenium. Diffusion experiments were performed independently at least two times, and each experiment comprised three replicates.

5.4.5 Confocal Imaging of Bacteria. A total of 10^8 bacterial cells/mL was seeded (2 mL in M9 media) in a confocal dish and allowed to grow; old medium was replaced every 24 h. After 3 days, medium was replaced by RBC-NZ and biofilms were incubated for 1 h; biofilm samples incubated with only M9 media were used as the control. After 1 h, biofilms were washed with PBS three times and were incubated with 10 μM of the substrates for 1 h. The cells were then washed with PBS three times. Confocal microscopy images were obtained on a Zeiss LSM 510 Meta microscope by using a 60× objective. The settings of the confocal microscope were as follows: green channel, λex = 488 nm and λem = BP 505−530 nm; red channel, λex = 543 nm and λem = LP 650 nm. Emission filters: BP =band pass, LP = high pass.

5.4.6 Prodrug activation: Biofilms were cultured as mentioned in the above section. Biofilms were washed off and incubated with RBC-NZ (500 nM) in minimal M9 media. After 24 h, biofilms were washed with PBS buffer three times and treated with pro-Mox at a concentration of 2.5, 5, 10 μM for 24 h. The cells were then completely washed off and 10% alamar blue in minimal media was added to each well (220 μl) and incubated further at 37°C for 2 h. Biofilm viability was then determined by measuring the fluorescence intensity at 570 nm using a SpectraMax M5 microplate spectrophotometer.

5.5 Supplementary information

5.5.1 DLS characterization of nanozymes. The hydrodynamic diameter of the nanozymes were measured by dynamic light scattering (DLS) in DI water using Malvern Zetasizer Nano ZS instrument. The measurement setting were as follows: angle: 173° (backscatter), "multiple narrow modes" (high resolution) based on non-negative-least-squares (NNLS).

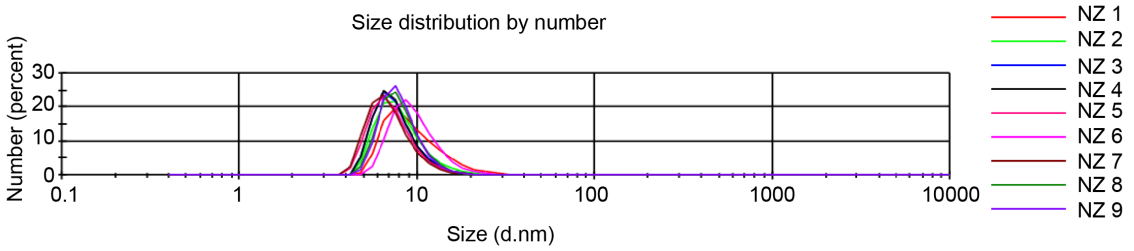

Figure 5.5. DLS measurements of NZ 1 - NZ 9.

Table 5.1. The size of nanozymes obtained from DLS.

Nanozymes	Size (d.nm)
NZ 1	9.1 ± 2.1
NZ 2	9.8 ± 2.3
NZ 3	8.7 ± 3.5
NZ 4	8.7 ± 0.9

NZ 5	8.1 ± 1.9
NZ 6	8.1 ± 2.4
NZ 7	8.1 ± 3.7
NZ 8	8.4 ± 4.1
NZ 9	9.4 ± 2.9

5.5.2 TEM characterization of nanozymes. Transmission Electron Microscopy (TEM) images of samples were taken using JEOL CX-100 electron microscopy. Samples were prepared by placing one drop of the desired solution onto a 300-mesh Cu grid-coated with carbon film. No aggregation was observed after catalyst encapsulation.

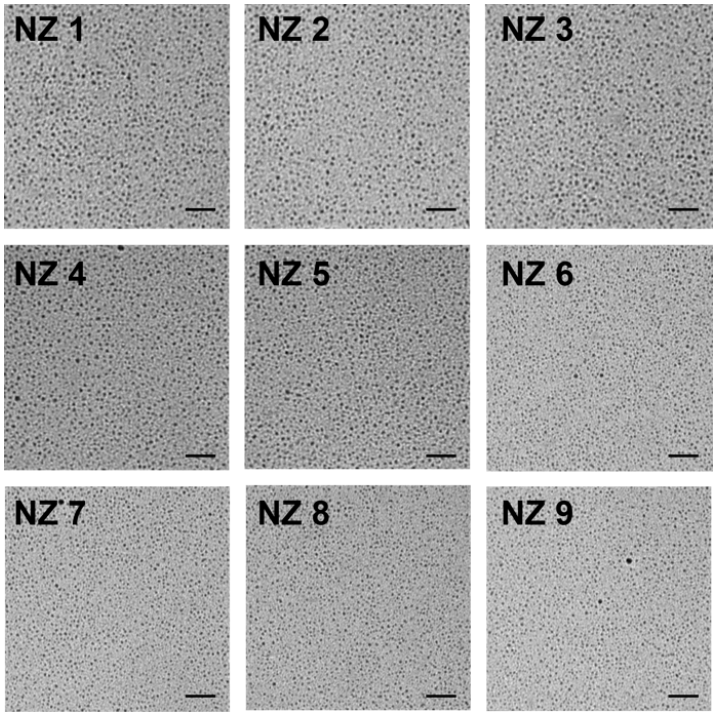

Figure 5.6. TEM images of nanozymes. Scale bar = 20 nm.

5.5.3 Quantification of catalyst per AuNP using ICP-MS characterization. The catalysts were quantified using previously established protocols.[46] Briefly, the nanoparticle solutions were diluted in milli-Q water to 200 nM. 10 μL of the diluted solution was taken for each

replicate. 0.5 mL of aqua regia was added to each replicate and was diluted to 10 mL by adding milli-Q water. The amount of encapsulated catalysts was measured by a Perkin-Elmer NexION 300X ICP mass spectrometer by tracking ^{56}Fe relative to ^{197}Au. For calibration, a series of solutions with gold and iron (concentration: 0, 0.2, 0.5,1, 2, 5, 10, and 20 ppb) were prepared. Operating conditions were as follows: nebulizer flow rate: 0.95 L/min; rf power: 1600 W; plasma Ar flow rate: 18 L/min; dwell time: 50 ms.

Table 5.2. Gold (Au) and iron (Fe) amount in the nanozymes using ICP-MS measurement. The Fe/AuNP represents number of catalysts encapsulated per AuNP.

Nanozymes	Au(ppb)	Fe(ppb)	Fe/AuNP
1	24.6	1.2	35.6 ± 2.1
2	27.7	1.3	33.2 ± 1.1
3	27.3	1.1	34.8 ± 5.9
4	24.6	0.9	34.9 ± 3.6
5	27.1	1.4	33.1 ± 1.8
6	25.9	1.1	35.4 ± 7.1
7	26.6	1.2	30.2 ± 10.3
8	22.9	1.0	30.7 ± 9.9
9	28.7	1.2	31.1 ± 8.2

5.5.4 Hemolysis assays with nanozymes. Hemolysis assays on red blood cells were performed using previously reported protocols.[47] Briefly, human whole blood (pooled, mixed gender) was purchased from Bioreclamation LLC, NY and processed as soon as received. 10 ml phosphate buffered saline (PBS) was added to the blood and centrifuged for 5 minutes at 5000 r.p.m. Supernatant was discarded followed by redispersion of RBCs in 10 ml of PBS. This cycle was repeated at least 5 times. Finally, RBCs were diluted in 10 ml of PBS and kept on ice during sample preparation. 0.4 ml of NZs (different concentrations) were prepared in a 1.5 ml Eppendorf tube, followed by addition of 0.1 ml of RBC solution. RBCs incubated with water and PBS were used as negative and positive controls respectively and all the samples were prepared in triplicates. These mixtures were incubated at 37 °C, 150 r.p.m for 24 hours. The mixtures were then centrifuged at 4000 r.p.m for 5 minutes and 100 µl of supernatant was transferred to a 96-well plate.

The absorbance of supernatant was measured at 570 nm using Molecular Devices SpectraMax M2 microplate reader with 655 nm as a reference.

5.5.5 Nanozyme adsorption on RBCs. RBCs were isolated from human whole blood as described in the above section. Next, nanozymes (NZ 1-9) with varied concentrations (100 – 1000 nM) were incubated with RBCs in PBS for 1 hour at 37 °C, 150 r.p.m. The NZ-RBC mixture were then washed with PBS five times at 4000 r.p.m for 5 minutes to remove excess NZs in the solution. The isolated RBCs were then processed for ICP-MS analysis and quantified for gold content.

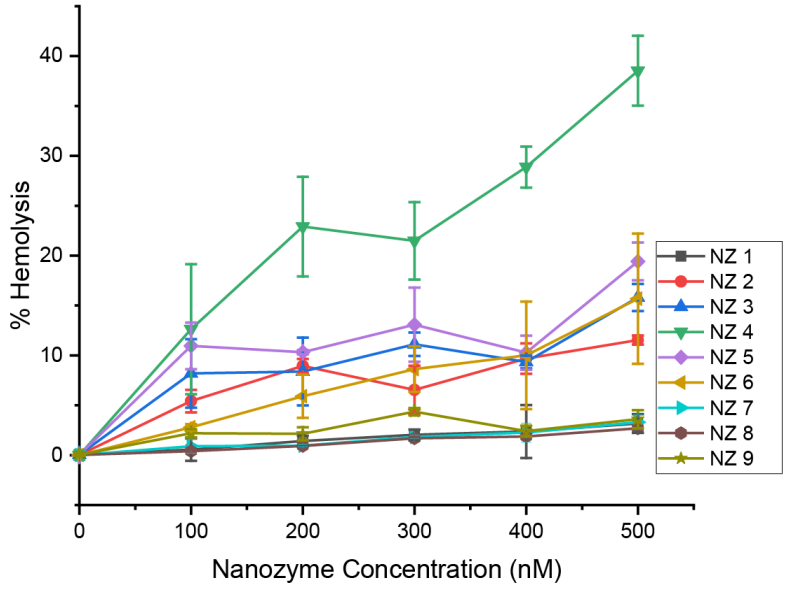

Figure 5.7. Dose-dependent hemolytic activity of NZ 1–NZ 9 in the presence of plasma proteins. % hemolysis was calculated using water as the positive control. Error bars represent standard deviations (n = 3).

5.5.6 Synthesis of aryl-azide protected resorufin substrate (pro-res).

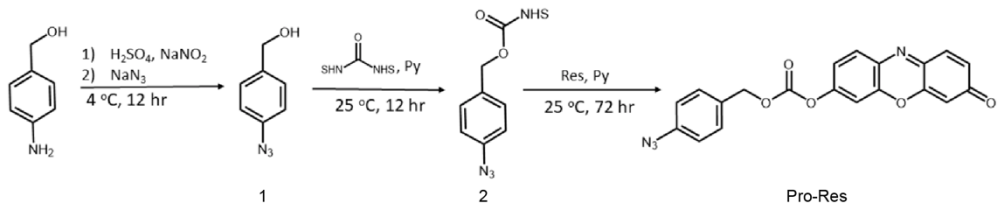

Compound 1 was synthesized from the corresponding aminated compound. A solution of 4-aminobenzyl alcohol (2.15 g, 17.5 mmol) was dissolved in THF (25 mL) and mixed with an aqueous solution of H_2SO_4 (4.8 mL 98%, in 60 mL of water) cooled at 4 ºC in a round bottom flask. An aqueous solution of $NaNO_2$ (1.45 g, 21 mmol) was added to the solution and was allowed to react for 1 h in ice bath. An aqueous solution of NaN_3 (1.8 g, 28.9 mmol) was added to the solution. The mixture was led to react overnight followed by collecting 4-azidobenzyl alcohol by three liquid-liquid extraction processes using dichloromethane (100 mL). Fractions were collected and dried over anhydrous Na_2SO_4, concentrated and purified by flash column chromatography (DCM: MetOH 19:1). Yield 84%.

5.5.7 Nanozyme kinetics in solution. Pro-res (non-fluorescent) was used as a substrate to test the catalytic activity of the nanozymes. A solution containing 10 μM substrate and RBC-NZs (100 – 1000 nM) was prepared in a 96-well plate. A solution of 500 nM free nanozyme (Bare-NZ) with 10 μM substrate was used for comparison. Solutions of RBC-NZs, 10 μM substrate, RBCs alone were used as negative controls. The kinetic study was done by tracking the fluorescence intensity (ex = 561 nm, em = 590 nm) using a Molecular Devices SpectraMax M2 microplate reader.

5.5.8 Biofilm Culture. Biofilms were cultured as reported in previously established protocols. Briefly, bacteria were grown overnight in LB media at 37 ˚C until to reach stationary phase. Bacteria cultures were then centrifuged and washed three times using 0.85% sodium chloride solution. Bacteria were resuspended in PBS and their concentrations were determined using optical density measurements at 600 nm. Seeding solutions were made in M9 media to reach an OD_{600} of 0.1. 500 μL of the seeding solutions were added to each well of the 12-well microplate (100 μl seeding soltions were used for 96-well plates). The plates were covered and incubated at room temperature for 24 hours in static conditions.

5.5.9 Hemolytic activity of bacterial strains. Biofilms were cultured in a 12-well plate using the above-mentioned protocol. Red Blood Cells were isolated from human whole blood and

suspended in PBS. 500 µl of RBC solution was added to the 12-well plates containing biofilms and incubated at 37 °C, 150 rpm for 30 minutes and 24 hours. RBC solution incubated in PBS and milli-q water (500 µl) were used positive and negative controls respectively. Solutions from 12-well plate were collected in a 1.5 ml eppendorf tubes and centrifuged at 4000 rpm for 5 minutes. The supernatant was transferred to a clear 96-well microplate and absorbance was measured at 570 nm using Molecular Devices SpectraMax M2 microplate reader with reference at 655 nm.

5.5.10 Nanozyme accumulation studies in biofilms. 0.1 OD_{600} bacterial cells were plated in a 12-well plate for 24 hours. On the following day, media was replaced with fresh M9 minimal media and further incubated for 24 hours. Biofilms were then washed three times with PBS, followed by incubation with RBC-NZs (500 nM) in minimal M9 media for 24 hours at 37 °C. Biofilms incubated with free NZs (Bare-NZs) and media alone were used as controls. After incubation, the biofilms were washed with PBS three times, followed by addition of lysis buffer to each well. All lysed samples were then further processed for ICP-MS analysis (*vide infra*) to determine the intrabiofilm amount of gold. Nanozyme accumulation experiments were performed at least two times, and each experiment comprised three replicates.

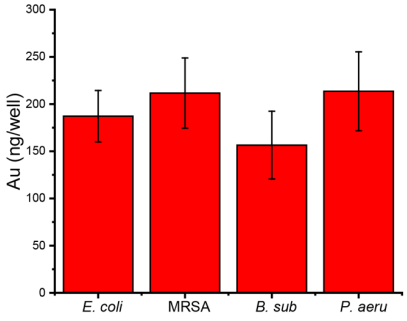

Figure 5.8. Amount of gold (Au) accumulated in biofilms obtained from ICP-MS upon treatment with free NZ 1.

5.5.11 Confocal imaging of biofilms. 10^8 cfu/ml of GFP expressing methicillin-resistant *S. aureus* supplemented with 1mM of IPTG (isopropyl β-D-1-thiogalactopyranoside) bacteria solution (2 ml in M9 media) was seeded in a confocal dish and allowed to grow for 3 days. Old media was replaced every 24 hours. After 3 days, media was replaced by RBC-NZs (500 nM) and

biofilms were incubated for 3 hours. Biofilms were then washed with PBS three times to remove excess NZs or RBC debris from the solution, followed by addition of 20 μM Pro-Res (substrate) for 1 hour. The biofilms were then washed three times with PBS and visualized under a confocal microscope. Confocal images were obtained on a Zeiss LSM 519 Meta microscope by using a 63× objective. The settings of the confocal microscope were as follows: green channel: λ_{ex}=488 nm and λ_{em}=BP 505-530 nm; red channel: λ_{ex}=543 nm and λ_{em}=LP 650 nm. Emission filters: BP=band pass, LP=high pass.

5.5.12 Synthesis of aryl-azide protected moxofloxacin substrate (pro-Mox).

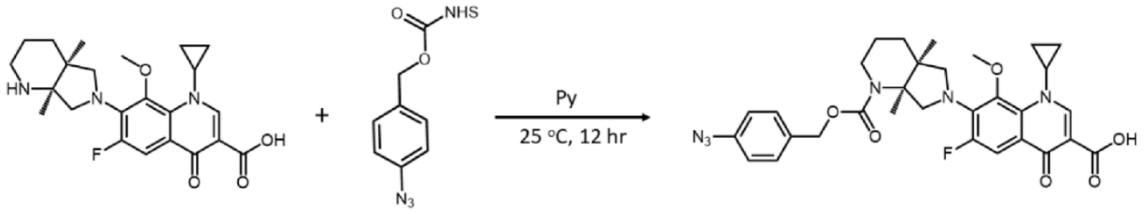

Mox 3 Pro-Mox

The compound 3 (100 mg, 1 eq) was added to a rounded bottom flask containing a solution of Mox (100 mg, 0.75 eq) and 50 mg of solid $NaHCO_3$ (1.2 eq) in anhydrous DMF (5 mL). The mixture was left to react overnight. Cold water was added and the product was extracted by washing with ethyl acetate. All organic fractions were then collected and dried over anhydrous Na_2SO_4, concentrated and purified by recrystallization in ethyl acetate. Yield 64 %.

5.5.13 Cellular uptake experiments. 20,000 RAW 264.7 macrophage cell lines (purchased from American Type Culture Collection, Manassas, VA) were cultured in Dulbecco's modified Eagle medium (DMEM; ATCC 30-2002) in the presence of 10% bovine calf serum and 1% antibiotic solution at 37 ºC in a humidified atmosphere of 5% CO_2 for 48 h. Old medium was replaced and washed with PBS. Meanwhile, RBC-NZs (100, 250 and 500 nM) solutions were prepared in prewarmed 10% serum containing media. Next, the cells were incubated with RBC-NZs (100, 250 and 500 nM) in 10% serum-containing media for 24 h at 37 °C. Free nanozymes (Bare-NZs) were used as controls. Subsequently, the cells were washed three times with PBS and

treated with lysis buffer. Lysed cells were then processed for ICP-MS analysis. Each experiment comprised of 3 replicates.

5.5.14 Confocal imaging of macrophage cells. Macrophages were seeded in a confocal disc at a concentration of 200,000 cells/mL in a 10% serum containing media. After 24 h, the cells were treated with RBC-NZ and were stored in incubator for overnight. Next, the cells were washed three times with PBS and were incubated with pro-resorufin for 0.5 h. Hoechst 33342 was used as a nuclear staining dye. The cells treated with free NZ and proflurophore only were used as positive and negative controls respectively.

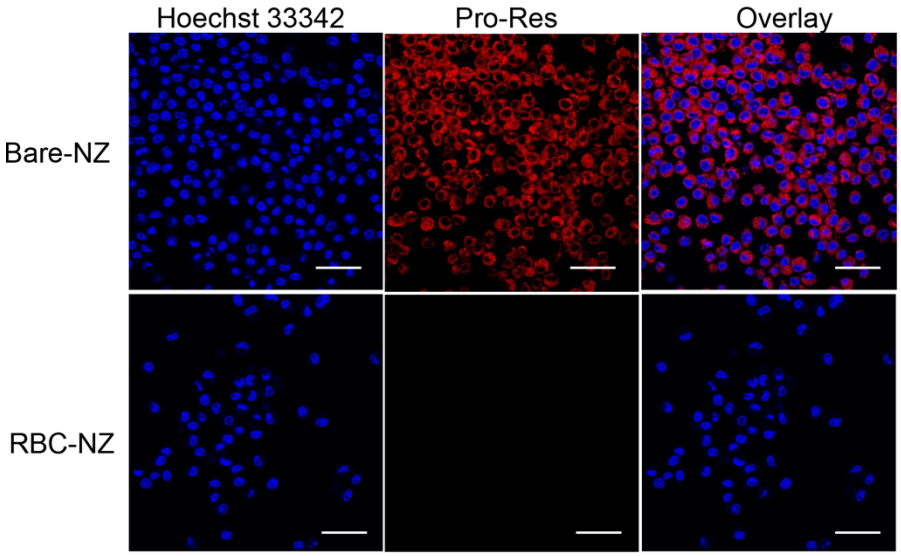

Figure 5.9. Confocal images of macrophage cells (RAW 264.7) incubated with RBC-NZ and Bare-NZ in presence of pro-resorufin. No fluorescence was generated by RBC-NZ, indicating that the RBC-hichhiked nanozymes were not uptaken by macrophages. Hoechst 33342 was used as a nuclear staining dye. The scale bars are 25 μm.

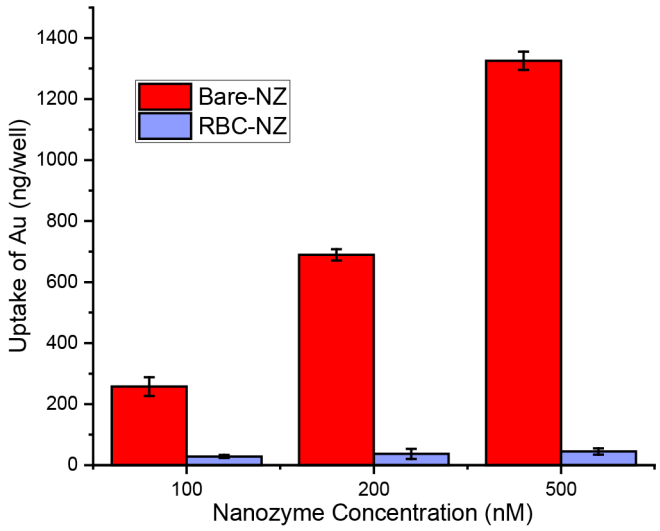

Figure 5.10. Nanoparticle uptake by RAW 264.7 macrophage cells biofilms after incubation for 24 h in pH 7.4 media with Bare-NZ and RBC-NZ (500 nM), as measured by ICP-MS. These results indicate that RBC hitchhiking prevents uptake of NZ 1.

5.5.15 Biofilm treatment using pro-antibiotic activation. 10^8 cfu/ml of bacteria seeding solution was prepared in minimal M9 media. 100 µl of the seeding solution was added to each well of the 96-well microplate. The plates were covered and incubated at room temperature for 24 hours at static conditions. On the following day, solution of RBC-NZs was prepared in M9 media and diluted to desired levels and incubated with biofilms for 24 hours at 37 °C overnight without shaking. Biofilms were then washed with PBS to remove unattached NZs or RBC debris, and incubated with pro-mox (1-10 µM) diluted in M9 minimal media for 24 hours at 37 °C. The cells were then washed three times with PBS and incubated with 10% alamar blue in minimal M9 media for 3 hours at 37 °C. Biofilm viability was then determined by measuring fluorescence intensity at 570 nm using a Molecular Devices SpectraMax M2 microplate reader. Biofilms incubated with RBC-NZs, pro-mox and moxifloxacin only were used as controls.

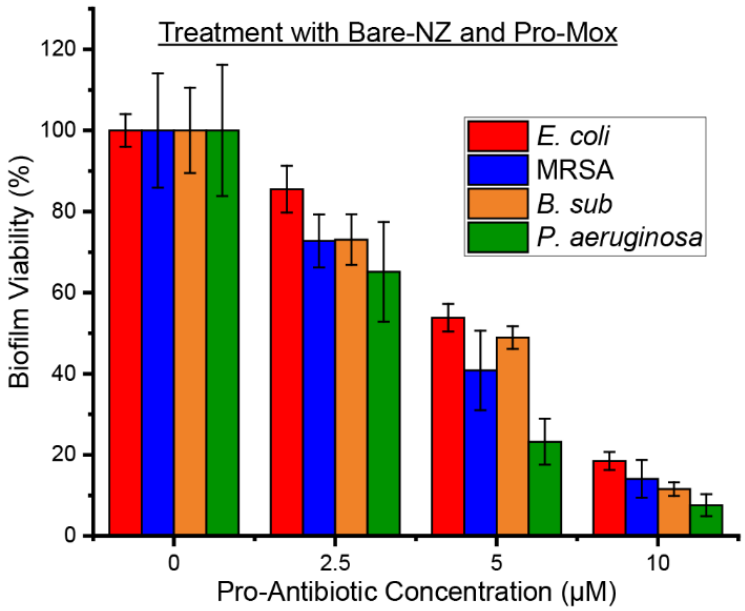

Figure 5.11. Viability % of biofilm treated with bare-NZ with increasing concentration of pro-Mox.

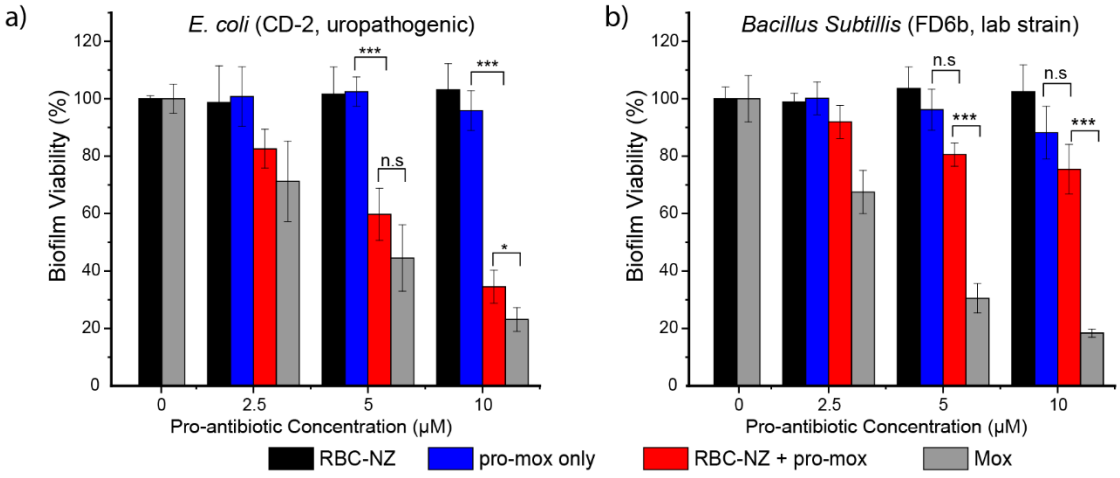

Figure 5.12. Deprotection of antimicrobials in biofilms using RBC-hitchhiked nanozymes: a) *E. coli* (toxin producing) biofilms and b) *B. Sub* (non-pathogenic) biofilms treated with pro-Mox and RBC-NZ (red bars) at 37 °C. Biofilms treated only with pro-Mox (blue bars) or with Mox (grey bars) were used in all experiments as negative and positive controls, respectively. Each experiment was replicated five times. Error bars represent standard deviations of these measurements. *$p < 0.05$, ***$p < 0.001$

5.6 References

1. Sletten, E. M.; Bertozzi, C. R. Bioorthogonal Chemistry: Fishing for Selectivity in a Sea of Functionality. *Angew. Chemie Int. Ed.* **2009,** *48,* 6974–6998.

2. Yang, M.; Li, J.; Chen, P. R.; Transition metal-mediated bioorthogonal protein chemistry in living cells. *Chem. Soc. Rev.* **2014,** *23,* 6511–6526.

3. Patterson, D. M.; Nazarova, L. A.; Prescher, J. A. Finding the Right (Bioorthogonal) Chemistry. *ACS Chem. Biol.* **2014,** *9,* 592–605.

4. Ramil, C. P.; Lin, Q. Bioorthogonal chemistry: strategies and recent developments. *Chem. Commun.* **2013,** *49,* 11007–11022.

5. Volker, T.; Meggers, E. Transition-metal-mediated uncaging in living human cells-an emerging alternative to photolabile protecting groups. *Curr. Opin. Chem. Biol.* **2015,** *25,* 48–54.

6. Jeschek, M.; Reuter, R.; Heinisch, T.; Trindler, C.; Klehr, J.; Panke, S.; Ward, T. R. Directed Evolution of Artificial Metalloenzymes for in Vivo Metathesis. *Nature* **2016**, *537*, 661-665.

7. Zhang, X.; Huang, R.; Gopalakrishnan, S.; Cao-Milán, R.; Rotello, V. M. Bioorthogonal Nanozymes: Progress towards Therapeutic Applications. *Trends Chem.* **2019,** *1,* 90–98.

8. Bai, Y.; Chen, J.; Zimmerman, S. C. Designed transition metal catalysts for intracellular organic synthesis. *Chem. Soc. Rev.* **2018,** *47,* 1811–1821.

9. Das, R.; Landis, R. F.; Tonga, G. Y.; Cao-Milán, R.; Luther, D. C.; Rotello, V. M. Control of Intra- versus Extracellular Bioorthogonal Catalysis Using Surface-Engineered Nanozymes. *ACS Nano.* **2018**, *13*, 229-235.

10. Weiss, J. T.; Dawson, J. C.; Macleod, K. G.; Rybski, W.; Fraser, C.; Torres-Sánchez, C.; Patton, E. E.; Bradley, M.; Carragher, N. O.; Unciti-Broceta, A. Extracellular Palladium-Catalysed Dealkylation of 5-Fluoro-1-Propargyl-Uracil as a Bioorthogonally Activated Prodrug Approach. *Nat. Commun.* **2014**, *5*, 3277-3285.

11 . Yusop, R. M.; Unciti-Broceta, A.; Johansson, E. M. V.; Sánchez-Martín, R. M.; Bradley, M. Palladium-mediated intracellular chemistry. *Nat. Chem.* **2011,** *3,* 239–243.

12. Gustafson, H. H.; Holt-Casper, D.; Grainger, D. W.; Ghandehari, H. Nanoparticle uptake: The phagocyte problem. *Nano Today* **2015,** *10,* 487–510.

13 . Riehemann, K.; Schneider, S. W.; Luger, T. A.; Godin, B.; Ferrari, M.; Fuchs, H. Nanomedicine—Challenge and Perspectives. *Angew. Chemie Int. Ed.* **2009**, *48*, 872–897.

14. Muzykantov, V. R. Drug delivery by red blood cells: vascular carriers designed by mother nature. *Expert Opin. Drug Deliv.* **2010,** *7,* 403–427.

15. Han, X.; Wang, C.; Liu, Z. Red Blood Cells as Smart Delivery Systems. *Bioconjug. Chem.* **2018,** *29,* 852–860.

16. Villa, C. H.; Pan, D. C.; Zaitsev, S.; Cines, D. B.; Siegel, D. L.; Muzykantov, V. R. Delivery of Drugs Bound to Erythrocytes: New Avenues for an Old Intravascular Carrier. *Ther. Deliv.* **2015**, *6*, 795–826.

17. Bhakdi, S.; Tranum-Jensen, J. Alpha-toxin of Staphylococcus aureus. *Microbiol. Rev.* **1991,** *55,* 733-751.

18. O'Hanley, P.; Lalonde, G.; Ji, G. Alpha-hemolysin contributes to the pathogenicity of piliated digalactoside-binding Escherichia coli in the kidney: efficacy of an alpha-hemolysin vaccine in preventing renal injury in the BALB/c mouse model of pyelonephritis. *Infect. Immun.* **1991,** *59,* 1153–1161.

19. Hu, C.-M. J.; Fang, R. H.; Copp, J.; Luk, B. T.; Zhang, L. A biomimetic nanosponge that absorbs pore-forming toxins. *Nat. Nanotechnol.* **2013,** *8,* 336-341.

20. Brenner, J. S.; Pan, D. C.; Myerson, J. W.; Marcos-Contreras, O. A.; Villa, C. H.; Patel, P.; Hekierski, H.; Chatterjee, S.; Tao, J.-Q.; Parhiz, H.; *et al.* Red Blood Cell-Hitchhiking Boosts Delivery of Nanocarriers to Chosen Organs by Orders of Magnitude. *Nat. Commun.* **2018**, *9*, 2684-2695.

21. Wang, C.; Sun, X.; Cheng, L.; Yin, S.; Yang, G.; Li, Y.; Liu, Z. Multifunctional Theranostic Red Blood Cells For Magnetic-Field-Enhanced in Vivo Combination Therapy of Cancer. *Adv. Mater.* **2014**, *26*, 4794–4802.

22. Villa, C. H.; Anselmo, A. C.; Mitragotri, S.; Muzykantov, V. Red blood cells: Supercarriers for drugs, biologicals, and nanoparticles and inspiration for advanced delivery systems. *Adv. Drug Deliv. Rev.* **2016,** *106,* 88–103.

23. Mai, T. D.; d'Orlyé, F.; Ménager, C.; Varenne, A.; Siaugue, J.-M. Red blood cells decorated with functionalized core–shell magnetic nanoparticles: elucidation of the adsorption mechanism. *Chem. Commun.* **2013,** *49,* 5393–5395.

24. Chambers, E.; Mitragotri, S. Long circulating nanoparticles via adhesion on red blood cells: mechanism and extended circulation. *Exp. Biol. Med. (Maywood).* **2007,** *232,* 958–966.

25. Saha, K.; Moyano, D. F.; Rotello, V. M. Protein coronas suppress the hemolytic activity of hydrophilic and hydrophobic nanoparticles. *Mater. Horizons* **2014,** *1,* 102–105.

26. Gupta, A.; Das, R.; Yesilbag Tonga, G.; Mizuhara, T.; Rotello, V. M. Charge-Switchable Nanozymes for Bioorthogonal Imaging of Biofilm-Associated Infections. *ACS Nano* **2018,** *12,* 89–94.

27. Tonga, G. Y.; Jeong, Y.; Duncan, B.; Mizuhara, T.; Mout, R.; Das, R.; Kim, S. T.; Yeh, Y.-C.; Yan, B.; Hou, S.; *et al.* Supramolecular Regulation of Bioorthogonal Catalysis in Cells Using Nanoparticle-Embedded Transition Metal Catalysts. *Nat. Chem.* **2015**, *7*, 597–603.

28. Huo, S.; Jiang, Y.; Gupta, A.; Jiang, Z.; Landis, R. F.; Hou, S.; Liang, X.-J.; Rotello, V. M. Fully Zwitterionic Nanoparticle Antimicrobial Agents through Tuning of Core Size and Ligand Structure. *ACS Nano* **2016**, *10*, 8732–8737.

29. Sasmal, P. K.; Carregal-Romero, S.; Han, A. A.; Streu, C. N.; Lin, Z.; Namikawa, K.; Elliott, S. L.; Köster, R. W.; Parak, W. J.; Meggers, E. Catalytic Azide Reduction in Biological Environments. *ChemBioChem* **2012**, *13*, 1116–1120.

30. Los, F. C. O.; Randis, T. M.; Aroian, R. V.; Ratner, A. J. Role of Pore-Forming Toxins in Bacterial Infectious Diseases. *Microbiol. Mol. Biol. Rev.* **2013,** *77,* 173–207.

31. Peraro, M. D.; van der Goot, F. G. Pore-forming toxins: ancient, but never really out of fashion. *Nat. Rev. Microbiol.* **2015,** *14,* 77-86.

32. Skals, M.; Jensen, U. B.; Ousingsawat, J.; Kunzelmann, K.; Leipziger, J.; Praetorius, H. A. Escherichia Coli α-Hemolysin Triggers Shrinkage of Erythrocytes via KCa3.1 and TMEM16A Channels with Subsequent Phosphatidylserine Exposure. *J. Biol. Chem.* **2010**, *285*, 15557–15565.

33. Song, L.; Hobaugh, M. R.; Shustak, C.; Cheley, S.; Bayley, H.; Gouaux, J. E. Structure of Staphylococcal α-Hemolysin, a Heptameric Transmembrane Pore. *Science.* **1996**, *274*, 1859 1865.

34. Langdon, A.; Crook, N.; Dantas, G. The effects of antibiotics on the microbiome throughout development and alternative approaches for therapeutic modulation. *Genome Med.* **2016,** *8,* 39-44.

35. Li, Z.; Behrens, A. M.; Ginat, N.; Tzeng, S. Y.; Lu, X.; Sivan, S.; Langer, R.; Jaklenec, A. Biofilm-Inspired Encapsulation of Probiotics for the Treatment of Complex Infections. *Adv. Mater.* **2018**, *30*, 1803925.

36. Pornpattananangkul, D.; Zhang, L.; Olson, S.; Aryal, S.; Obonyo, M.; Vecchio, K.; Huang, C.-M.; Zhang, L. Bacterial Toxin-Triggered Drug Release from Gold Nanoparticle-Stabilized Liposomes for the Treatment of Bacterial Infection. *J. Am. Chem. Soc.* **2011**, *133*, 4132–4139.

37. Gao, W.; Vecchio, D.; Li, J.; Zhu, J.; Zhang, Q.; Fu, V.; Li, J.; Thamphiwatana, S.; Lu, D.; Zhang, L. Hydrogel Containing Nanoparticle-Stabilized Liposomes for Topical Antimicrobial Delivery. *ACS Nano* **2014**, *8*, 2900–2907.

38 . Gupta, A.; Landis, R. F.; Rotello, V. M. Nanoparticle-Based Antimicrobials: Surface Functionality Is Critical. *F1000Research* **2016**, *5*, 364-375.

39. Pan, D. C.; Myerson, J. W.; Brenner, J. S.; Patel, P. N.; Anselmo, A. C.; Mitragotri, S.; Muzykantov, V. Nanoparticle Properties Modulate Their Attachment and Effect on Carrier Red Blood Cells. *Sci. Rep.* **2018**, *8*, 1615-1621

40. Tulkens, P. M.; Arvis, P.; Kruesmann, F. Moxifloxacin safety: an analysis of 14 years of clinical data. *Drugs R. D.* **2012,** *12,* 71–100.

41. Emami, S.; Shafiee, A.; Foroumadi, A. Structural features of new quinolones and relationship to antibacterial activity against Gram-positive bacteria. *Mini Rev. Med. Chem.* **2006,** *6,* 375–386.

42. Miranda, R. O.; Chen, H.-T.; You, C.-C.; E. Mortenson, D.; Yang, X.-C.; H. F. Bunz, U.; M. Rotello, V. Enzyme-Amplified Array Sensing of Proteins in Solution and in Biofluids. *J. Am. Chem. Soc.* **2010**, *132*, 5285–5289.

43. De, M.; Rana, S.; Akpinar, H.; Miranda, O. R.; Arvizo, R. R.; Bunz, U. H. F.; Rotello, V. M. Sensing of Proteins in Human Serum Using Conjugates of Nanoparticles and Green Fluorescent Protein. *Nat. Chem.* **2009**, *1*, 461-469.

44. Liu, X.; Atwater, M.; Wang, J.; Huo, Q. Extinction Coefficient of Gold Nanoparticles with Different Sizes and Different Capping Ligands. *Colloids Surf.* **2007**, *58*, 3-7.

45. Saha, K.; Moyano, D. F.; Rotello, V. M. Protein Coronas Suppress the Hemolytic Activity of Hydrophilic and Hydrophobic Nanoparticles. *Mater. Horiz.* **2014**, *1*, 102–105.

46. Gupta, A.; Das, R.; Yesilbag Tonga, G.; Mizuhara, T.; Rotello, V. M. Charge-Switchable Nanozymes for Bioorthogonal Imaging of Biofilm-Associated Infections. *ACS Nano* **2018**, *12* (1), 89–94.

47. Huo, S.; Jiang, Y.; Gupta, A.; Jiang, Z.; Landis, R. F.; Hou, S.; Liang, X. J.; Rotello, V. M. Fully Zwitterionic Nanoparticle Antimicrobial Agents through Tuning of Core Size and Ligand Structure. *ACS Nano* **2016**, *10* (9), 8732–8737.

BIBLIOGRAPHY

Agarwal, P.; Bertozzi, C. R. Site-Specific Antibody–Drug Conjugates: The Nexus of Bioorthogonal Chemistry, Protein Engineering, and Drug Development. *Bioconjug. Chem.* **2015**, *26*, 176–192.

Albanese, A.; Tang, P. S.; Chan, W. C. W. The Effect of Nanoparticle Size, Shape, and Surface Chemistry on Biological Systems. *Annu. Rev. Biomed. Eng.* **2012**, *14*, 1–16.

Anderl, J. N.; Franklin, M. J.; Stewart, P. S. Role of Antibiotic Penetration Limitation in Klebsiella Pneumoniae; Biofilm Resistance to Ampicillin and Ciprofloxacin. *Antimicrob. Agents Chemother.* **2000**, *44*, 1818–1824.

Anderson, G. G.; Kenney, T. F.; MacLeod, D. L.; Henig, N. R.; O'Toole, G. A. Eradication of Pseudomonas Aeruginosa Biofilms on Cultured Airway Cells by a Fosfomycin/Tobramycin Antibiotic Combination . *Pathog. Dis.* **2013**, *67*, 39–45.

Anderson, G. G.; Moreau-Marquis, S.; Stanton, B. A.; O'Toole, G. A. In Vitro Analysis of Tobramycin-Treated Pseudomonas Aeruginosa Biofilms on Cystic Fibrosis-Derived Airway Epithelial Cells. *Infect. Immun.* **2008**, *76*, 1423–1433.

Anselmo, A. C.; Mitragotri, S. Cell-Mediated Delivery of Nanoparticles: Taking Advantage of Circulatory Cells to Target Nanoparticles. *J. Control. Release* **2014**, *190*, 531–541.

Bae, J.; McNamara, L. E.; Nael, M. A.; Mahdi, F.; Doerksen, R. J.; Bidwell, G. L.; Hammer, N. I.; Jo, S. Nitroreductase-Triggered Activation of a Novel Caged Fluorescent Probe Obtained from Methylene Blue. *Chem. Commun.* **2015**, *51*, 12787–12790.

Bai, Y.; Chen, J.; Zimmerman, S. C. Designed Transition Metal Catalysts for Intracellular Organic Synthesis. *Chem. Soc. Rev.* **2018**, *47*, 1811–1821.

Batrakova, E. V; Gendelman, H. E.; Kabanov, A. V. Cell-Mediated Drug Delivery. *Expert Opin. Drug Deliv.* **2011**, *8*, 415–433.

Becer, C. R.; Hoogenboom, R.; Schubert, U. S. Click Chemistry beyond Metal-Catalyzed Cycloaddition. *Angew. Chemie Int. Ed.* **2009**, *48*, 4900–4908.

Benoit, D. S. W.; Koo, H. Targeted, Triggered Drug Delivery to Tumor and Biofilm Microenvironments. *Nanomedicine* **2016**, *11*, 873–879.

Bertozzi, C. R. A Decade of Bioorthogonal Chemistry. *Acc. Chem. Res.* **2011**, *44*, 651–653.

Bhakdi, S.; Tranum-Jensen, J. Alpha-toxin of Staphylococcus aureus. *Microbiol. Rev.* **1991,** *55,* 733-751.

Bjarnsholt, T. The Role of Bacterial Biofilms in Chronic Infections. *APMIS* **2013**, *121*, 1–58.

Boyce, M.; Bertozzi, C. R. Bringing Chemistry to Life. *Nat. Methods* **2011**, *8*, 638-642.

Brannon-Peppas, L.; Blanchette, J. O. Corrigendum to "Nanoparticle and Targeted Systems for Cancer Therapy" *Adv. Drug Deliv. Rev.* **2009**, *61*, 364-371.

Bray, T. L.; Salji, M.; Brombin, A.; Pérez-López, A. M.; Rubio-Ruiz, B.; Galbraith, L. C. A.; Patton, E. E.; Leung, H. Y.; Unciti-Broceta, A. Bright Insights into Palladium-Triggered Local Chemotherapy. *Chem. Sci.* **2018**, *9*, 7354–7361.

Brenner, J. S.; Pan, D. C.; Myerson, J. W.; Marcos-Contreras, O. A.; Villa, C. H.; Patel, P.; Hekierski, H.; Chatterjee, S.; Tao, J.-Q.; Parhiz, H.; *et al.* Red Blood Cell-Hitchhiking Boosts Delivery of Nanocarriers to Chosen Organs by Orders of Magnitude. *Nat. Commun.* **2018**, *9*, 2684-2691.

Brown, J. M.; Giaccia, A. J. The Unique Physiology of Solid Tumors: Opportunities (and Problems) for Cancer Therapy. *Cancer Res.* **1998**, *58*, 1408 LP – 1416.

Brust, M.; Walker, M.; Bethell, D.; Schiffrin, D. J.; Whyman, R. Synthesis of Thiol-Derivatised Gold Nanoparticles in a Two-Phase Liquid-Liquid System. *J. Chem. Soc. Chem. Commun.* **1994**, *5,* 801–802.

Burgess, A.; Vigneron, S.; Brioudes, E.; Labbé, J.-C.; Lorca, T.; Castro, A. Loss of Human Greatwall Results in G2 Arrest and Multiple Mitotic Defects Due to Deregulation of the Cyclin B-Cdc2/PP2A Balance. *Proc. Natl. Acad. Sci.* **2010**, *107*, 12564 LP – 12569.

Byrne, J. D.; Betancourt, T.; Brannon-Peppas, L. Active Targeting Schemes for Nanoparticle Systems in Cancer Therapeutics. *Adv. Drug Deliv. Rev.* **2008**, *60*, 1615–1626.

Cao-Milán, R.; He, L. D.; Shorkey, S.; Tonga, G. Y.; Wang, L.-S.; Zhang, X.; Uddin, I.; Das, R.; Sulak, M.; Rotello, V. M. Modulating the Catalytic Activity of Enzyme-like Nanoparticles through Their Surface Functionalization. *Mol. Syst. Des. Eng.* **2017**, *2*, 624–628.

Choi, J.; Kim, H.; Jin, E.; Jung, J.; Park, J.; Chung, H.; Seong, J.; Shin, J.; Joo, H.; Yeol, S.; *et al.* Biomaterials Use of Macrophages to Deliver Therapeutic and Imaging Contrast Agents to Tumors. *Biomaterials* **2012**, *33*, 4195–4203.

Choi, M. R.; Stanton-Maxey, K. J.; Stanley, J. K.; Levin, C. S.; Bardhan, R.; Akin, D.; Badve, S.; Sturgis, J.; Robinson, J. P.; Bashir, R.; *et al.* A Cellular Trojan Horse for Delivery of Therapeutic Nanoparticles into Tumors. *Nano Lett.* **2007**, *7*, 3759–3765.

Clavadetscher, J.; Indrigo, E.; Chankeshwara, S. V; Lilienkampf, A.; Bradley, M. In-Cell Dual Drug Synthesis by Cancer-Targeting Palladium Catalysts. *Angew. Chemie* **2017**, *129*, 6968–6972.

Cohen, S. S.; Flaks, J. G.; Barner, H. D.; Loeb, M. R.; Lichtenstein, J. THE MODE OF ACTION OF 5-FLUOROURACIL AND ITS DERIVATIVES. *Proc. Natl. Acad. Sci. U. S. A.* **1958**, *44*, 1004–1012.

Costerton, J. W.; Post, J. C.; Ehrlich, G. D.; Hu, F. Z.; Kreft, R.; Nistico, L.; Kathju, S.; Stoodley, P.; Hall-Stoodley, L.; Maale, G.; *et al.* New Methods for the Detection of Orthopedic and Other Biofilm Infections. *FEMS Immunol. Med. Microbiol.* **2011**, *61*, 133–140.

Costerton, W.; Veeh, R.; Shirtliff, M.; Pasmore, M.; Post, C.; Ehrlich, G. The Application of Biofilm Science to the Study and Control of Chronic Bacterial Infections. *J. Clin. Invest.* **2003**, *112*, 1466–1477.

Danhier, F.; Feron, O.; Préat, V. To Exploit the Tumor Microenvironment: Passive and Active Tumor Targeting of Nanocarriers for Anti-Cancer Drug Delivery. *J. Control. Release* **2010**, *148*, 135–146.

Das, M.; Sanson, N.; Kumacheva, E. Zwitterionic Poly(Betaine-N-Isopropylacrylamide) Microgels: Properties and Applications. *Chem. Mater.* **2008**, *20*, 7157–7163.

Das, R.; Landis, R. F.; Tonga, G. Y.; Cao-Milán, R.; Luther, D. C.; Rotello, V. M. Control of Intra- versus Extracellular Bioorthogonal Catalysis Using Surface-Engineered Nanozymes. *ACS Nano* **2019** *13*, 229-235.

De, M.; Rana, S.; Akpinar, H.; Miranda, O. R.; Arvizo, R. R.; Bunz, U. H. F.; Rotello, V. M. Sensing of Proteins in Human Serum Using Conjugates of Nanoparticles and Green Fluorescent Protein. *Nat. Chem.* **2009**, *1*, 461-469.

Debets, M. F.; van Berkel, S. S.; Dommerholt, J.; Dirks, A. (Ton) J.; Rutjes, F. P. J. T.; van Delft, F. L. Bioconjugation with Strained Alkenes and Alkynes. *Acc. Chem. Res.* **2011**, *44*, 805–815.

Devaraj, N. K. The Future of Bioorthogonal Chemistry. *ACS Cent. Sci.* **2018**, *4*, 952–959.

Dhar, S.; Daniel, W. L.; Giljohann, D. A.; Mirkin, C. A.; Lippard, S. J. Polyvalent Oligonucleotide Gold Nanoparticle Conjugates as Delivery Vehicles for Platinum(IV) Warheads. *J. Am. Chem. Soc.* **2009**, *131*, 14652–14653.

Doshi, N.; Swiston, A. J.; Gilbert, J. B.; Alcaraz, M. L.; Cohen, R. E.; Rubner, M. F.; Mitragotri, S. Cell-Based Drug Delivery Devices Using Phagocytosis- Resistant Backpacks. **2011**, *17,* 269-276.

Emami, S.; Shafiee, A.; Foroumadi, A. Structural features of new quinolones and relationship to antibacterial activity against Gram-positive bacteria. *Mini Rev. Med. Chem.* **2006,** *6,* 375–386.

Ganta, S.; Devalapally, H.; Shahiwala, A.; Amiji, M. A Review of Stimuli-Responsive Nanocarriers for Drug and Gene Delivery. **2008**, *126*, 187–204.

Gao, W.; Vecchio, D.; Li, J.; Zhu, J.; Zhang, Q.; Fu, V.; Li, J.; Thamphiwatana, S.; Lu, D.; Zhang, L. Hydrogel Containing Nanoparticle-Stabilized Liposomes for Topical Antimicrobial Delivery. *ACS Nano* **2014**, *8*, 2900–2907.

Garber, S. B.; Kingsbury, J. S.; Gray, B. L.; Hoveyda, A. H. Efficient and Recyclable Monomeric and Dendritic Ru-Based Metathesis Catalysts. *J. Am. Chem. Soc.* **2000**, *122*, 8168–8179.

Garzon, R.; Marcucci, G.; Croce, C. M. Targeting MicroRNAs in Cancer: Rationale, Strategies and Challenges. *Nat. Rev. Drug Discov.* **2010**, *9*, 775-782.

Ghosh, P.; Han, G.; De, M.; Kim, C. K.; Rotello, V. M. Gold Nanoparticles in Delivery Applications. *Adv. Drug Deliv. Rev.* **2008**, *60*, 1307–1315.

Gibson, J. D.; Khanal, B. P.; Zubarev, E. R. Paclitaxel-Functionalized Gold Nanoparticles. *J. Am. Chem. Soc.* **2007**, *129*, 11653–11661.

Gupta, A.; Das, R.; Yesilbag Tonga, G.; Mizuhara, T.; Rotello, V. M. Charge-Switchable Nanozymes for Bioorthogonal Imaging of Biofilm-Associated Infections. *ACS Nano* **2018**, *12*, 89–94.

Gupta, A.; Landis, R. F.; Li, C.-H.; Schnurr, M.; Das, R.; Lee, Y.-W.; Yazdani, M.; Liu, Y.; Kozlova, A.; Rotello, V. M. Engineered Polymer Nanoparticles with Unprecedented Antimicrobial Efficacy and Therapeutic Indices against Multidrug-Resistant Bacteria and Biofilms. *J. Am. Chem. Soc.* **2018**, *140*, 12137–12143.

Gupta, A.; Moyano, D. F.; Parnsubsakul, A.; Papadopoulos, A.; Wang, L.-S.; Landis, R. F.; Das, R.; Rotello, V. M. Ultrastable and Biofunctionalizable Gold Nanoparticles. *ACS Appl. Mater. Interfaces* **2016**, *8*, 14096–14101.

Gupta, A.; Mumtaz, S.; Li, C.-H.; Hussain, I.; Rotello, V. M. Combatting Antibiotic-Resistant Bacteria Using Nanomaterials. *Chem. Soc. Rev.* **2019**, *48*, 415–427.

Gupta, A.; Saleh, N. M.; Das, R.; Landis, R. F.; Bigdeli, A.; Motamedchaboki, K.; Rosa Campos, A.; Pomeroy, K.; Mahmoudi, M.; Rotello, V. M. Synergistic Antimicrobial Therapy Using Nanoparticles and Antibiotics for the Treatment of Multidrug-Resistant Bacterial Infection. *Nano Futur.* **2017**, *1*, 15004-15009.

Gustafson, H. H.; Holt-Casper, D.; Grainger, D. W.; Ghandehari, H. Nanoparticle Uptake: The Phagocyte Problem. *Nano Today* **2015**, *10*, 487–510.

Hall-Stoodley, L.; Costerton, J. W.; Stoodley, P. Bacterial Biofilms: From the Natural Environment to Infectious Diseases. *Nat. Rev. Microbiol.* **2004**, *2*, 95–108.

Hall-Stoodley, L.; Hu, F. Z.; Gieseke, A.; Nistico, L.; Nguyen, D.; Hayes, J.; Forbes, M.; Greenberg, D. P.; Dice, B.; Burrows, A.; *et al.* Direct Detection of Bacterial Biofilms on the Middle-Ear Mucosa of Children With Chronic Otitis Media. *JAMA* **2006**, *296*, 202–211.

Hall-Stoodley, L.; Stoodley, P.; Kathju, S.; Høiby, N.; Moser, C.; William Costerton, J.; Moter, A.; Bjarnsholt, T. Towards Diagnostic Guidelines for Biofilm-Associated Infections. *FEMS Immunol. Med. Microbiol.* **2012**, *65*, 127–145.

Han, X.; Wang, C.; Liu, Z. Red Blood Cells as Smart Delivery Systems. *Bioconjug. Chem.* **2018**, *29*, 852–860.

Hang, H. C.; Yu, C.; Kato, D. L.; Bertozzi, C. R. A Metabolic Labeling Approach toward Proteomic Analysis of Mucin-Type O-Linked Glycosylation. *Proc. Natl. Acad. Sci.* **2003**, *100*, 14846–14851.

Hein, J. E.; Fokin, V. V. Copper-Catalyzed Azide–Alkyne Cycloaddition (CuAAC) and beyond: New Reactivity of Copper(i) Acetylides. *Chem. Soc. Rev.* **2010**, *39*, 1302–1315.

Hong, R.; Fischer, N. O.; Verma, A.; Goodman, C. M.; Emrick, T.; Rotello, V. M. Control of Protein Structure and Function through Surface Recognition by Tailored Nanoparticle Scaffolds. *J. Am. Chem. Soc.* **2004**, *126*, 739–743.

Hong, R.; Han, G.; Fernández, J. M.; Kim, B.; Forbes, N. S.; Rotello, V. M. Glutathione-Mediated Delivery and Release Using Monolayer Protected Nanoparticle Carriers. *J. Am. Chem. Soc.* **2006**, *128*, 1078–1079.

Horev, B.; Klein, M. I.; Hwang, G.; Li, Y.; Kim, D.; Koo, H.; Benoit, D. S. W. PH-Activated Nanoparticles for Controlled Topical Delivery of Farnesol To Disrupt Oral Biofilm Virulence. *ACS Nano* **2015**, *9*, 2390–2404.

Hostetler, M. J.; Templeton, A. C.; Murray, R. W. Dynamics of Place-Exchange Reactions on Monolayer-Protected Gold Cluster Molecules. *Langmuir* **1999**, *15*, 3782–3789.

Hu, C.-M. J.; Fang, R. H.; Copp, J.; Luk, B. T.; Zhang, L. A Biomimetic Nanosponge That Absorbs Pore-Forming Toxins. *Nat. Nanotechnol.* **2013**, *8*, 336–340.

Huang, K.; Ma, H.; Liu, J.; Huo, S.; Kumar, A.; Wei, T.; Zhang, X.; Jin, S.; Gan, Y.; Wang, P. C.; *et al.* Size-Dependent Localization and Penetration of Ultrasmall Gold Nanoparticles in Cancer Cells, Multicellular Spheroids, and Tumors in Vivo. *ACS Nano* **2012**, *6*, 4483–4493.

Huma, Z.; Gupta, A.; Javed, I.; Das, R.; Hussain, S. Z.; Mumtaz, S.; Hussain, I.; Rotello, V. M. Cationic Silver Nanoclusters as Potent Antimicrobials against Multidrug-Resistant Bacteria. *ACS Omega* **2018**, *3*, 16721–16727.

Huo, S.; Jiang, Y.; Gupta, A.; Jiang, Z.; Landis, R. F.; Hou, S.; Liang, X.-J.; Rotello, V. M. Fully Zwitterionic Nanoparticle Antimicrobial Agents through Tuning of Core Size and Ligand Structure. *ACS Nano* **2016**, *10*, 8732–8737.

Jeong, Y.; Tonga, G. Y.; Duncan, B.; Yan, B.; Das, R.; Sahub, C.; Rotello, V. M. Solubilization of Hydrophobic Catalysts Using Nanoparticle Hosts. *Small* **2018**, *14*, 1702198.

Jeschek, M.; Reuter, R.; Heinisch, T.; Trindler, C.; Klehr, J.; Panke, S.; Ward, T. R. Directed Evolution of Artificial Metalloenzymes for in Vivo Metathesis. *Nature* **2016**, *537*, 661-665.

Jiang, Y.; Hardie, J.; Liu, Y.; Ray, M.; Luo, X.; Das, R.; Landis, R. F.; Farkas, M. E.; Rotello, V. M. Nanocapsule-Mediated Cytosolic SiRNA Delivery for Anti-in Fl Ammatory Treatment. **2018**, *2*, 235–240.

Jiang, Y.; Huo, S.; Mizuhara, T.; Das, R.; Lee, Y.-W.; Hou, S.; Moyano, D. F.; Duncan, B.; Liang, X.-J.; Rotello, V. M. The Interplay of Size and Surface Functionality on the Cellular Uptake of Sub-10 Nm Gold Nanoparticles. *ACS Nano* **2015**, *9*, 9986–9993.

Jordan, B. J.; Hong, R.; Han, G.; Rana, S.; Rotello, V. M. Modulation of Enzyme–Substrate Selectivity Using Tetraethylene Glycol Functionalized Gold Nanoparticles. *Nanotechnology* **2009**, *20*, 434004-434011.

Joshi, B. P.; Hardie, J.; Farkas, M. E. Harnessing Biology to Deliver Therapeutic and Imaging Entities via Cell-Based Methods. **2018**, *21,* 8717–8726.

Joshi, B. P.; Hardie, J.; Mingroni, M. A.; Farkas, M. E. Surface-Modified Macrophages Facilitate Tracking of Breast Cancer-Immune Interactions. *ACS Chem. Biol.* **2018**, *9*, 509-516.

Kang, K.; Park, J.; Kim, E. Tetrazine Ligation for Chemical Proteomics. *Proteome Sci.* **2017**, *15*, 15-20.

Kim, C. K.; Ghosh, P.; Pagliuca, C.; Zhu, Z.-J.; Menichetti, S.; Rotello, V. M. Entrapment of Hydrophobic Drugs in Nanoparticle Monolayers with Efficient Release into Cancer Cells. *J. Am. Chem. Soc.* **2009**, *131*, 1360–1361.

Kim, C. S.; Duncan, B.; Creran, B.; Rotello, V. M. Triggered Nanoparticles as Therapeutics. *Nano Today* **2013**, *8*, 439–447.

Klán, P.; Šolomek, T.; Bochet, C. G.; Blanc, A.; Givens, R.; Rubina, M.; Popik, V.; Kostikov, A.; Wirz, J. Photoremovable Protecting Groups in Chemistry and Biology: Reaction Mechanisms and Efficacy. *Chem. Rev.* **2013**, *113*, 119–191.

Kolb, H. C.; Finn, M. G.; Sharpless, K. B. Click Chemistry: Diverse Chemical Function from a Few Good Reactions. *Angew. Chemie Int. Ed.* **2001**, *40*, 2004–2021.

Kubin, R. F.; Fletcher, A. N. Fluorescence Quantum Yields of Some Rhodamine Dyes. *J. Lumin.* **1982**, *27*, 455–462.

Landis, R. F.; Gupta, A.; Lee, Y.-W.; Wang, L.-S.; Golba, B.; Couillaud, B.; Ridolfo, R.; Das, R.; Rotello, V. M. Cross-Linked Polymer-Stabilized Nanocomposites for the Treatment of Bacterial Biofilms. *ACS Nano* **2017**, *11*, 946–952.

Lang, K.; Davis, L.; Wallace, S.; Mahesh, M.; Cox, D. J.; Blackman, M. L.; Fox, J. M.; Chin, J. W. Genetic Encoding of Bicyclononynes and Trans-Cyclooctenes for Site-Specific Protein Labeling in Vitro and in Live Mammalian Cells via Rapid Fluorogenic Diels-Alder Reactions. *J. Am. Chem. Soc.* **2012**, *134*, 10317–10320.

Langdon, A.; Crook, N.; Dantas, G. The effects of antibiotics on the microbiome throughout development and alternative approaches for therapeutic modulation. *Genome Med.* **2016,** *8,* 39-44.

Lee, Y. W.; Luther, D. C.; Kretzmann, J. A.; Burden, A.; Jeon, T.; Zhai, S.; Rotello, V. M. Protein Delivery into the Cell Cytosol Using Non-Viral Nanocarriers. *Theranostics* **2019**, *9*, 3280–3292.

Leevy, W. M.; Gammon, S. T.; Jiang, H.; Johnson, J. R.; Maxwell, D. J.; Jackson, E. N.; Marquez, M.; Piwnica-Worms, D.; Smith, B. D. Optical Imaging of Bacterial Infection in Living Mice Using a Fluorescent Near-Infrared Molecular Probe. *J. Am. Chem. Soc.* **2006**, *128*, 16476–16477.

Lewis, C. E.; Pollard, J. W. Distinct Role of Macrophages in Different Tumor Microenvironments. *Cancer Res.* **2006**, *66*, 605–612.Distinct Role of Macrophages in Different Tumor Microenvironments. *Cancer Res.* **2006**, *66*, 605–612.

Lewis, K. Persister Cells, Dormancy and Infectious Disease. *Nat. Rev. Microbiol.* **2007**, *5*, 48-56.

Li, J.; Chen, P. R. Reactions in Bioorthogonal Chemistry. *Nat. Publ. Gr.* **2016**, *12*, 129–137.

Li, J.; Yu, J.; Zhao, J.; Wang, J.; Zheng, S.; Lin, S.; Chen, L.; Yang, M.; Jia, S.; Zhang, X.; *et al.* Palladium-Triggered Deprotection Chemistry for Protein Activation in Living Cells. *Nat. Chem.* **2014**, *6*, 352-361.

Li, X.; Yeh, Y.-C.; Giri, K.; Mout, R.; Landis, R. F.; Prakash, Y. S.; Rotello, V. M. Control of Nanoparticle Penetration into Biofilms through Surface Design. *Chem. Commun.* **2015**, *51*, 282–285.

Li, Z.; Behrens, A. M.; Ginat, N.; Tzeng, S. Y.; Lu, X.; Sivan, S.; Langer, R.; Jaklenec, A. Biofilm-Inspired Encapsulation of Probiotics for the Treatment of Complex Infections. *Adv. Mater.* **2018**, *30*, 1803925.

Liang, L.; Astruc, D. The Copper(I)-Catalyzed Alkyne-Azide Cycloaddition (CuAAC) "Click" Reaction and Its Applications. An Overview. *Coord. Chem. Rev.* **2011**, *255*, 2933–2945.

Liao, W.-C.; Sohn, Y. S.; Riutin, M.; Cecconello, A.; Parak, W. J.; Nechushtai, R.; Willner, I. Drug Delivery: The Application of Stimuli-Responsive VEGF- and ATP-Aptamer-Based Microcapsules for the Controlled Release of an Anticancer Drug, and the Selective Targeted Cytotoxicity toward Cancer Cells (Adv. Funct. Mater. 24/2016). *Adv. Funct. Mater.* **2016**, *26*, 4423-4432.

Liu, D. S.; Nivón, L. G.; Richter, F.; Goldman, P. J.; Deerinck, T. J.; Yao, J. Z.; Richardson, D.; Phipps, W. S.; Ye, A. Z.; Ellisman, M. H.; *et al.* Computational Design of a Red Fluorophore Ligase for Site-Specific Protein Labeling in Living Cells. **2014**, *111,* E4551-E4559.

Longley, D. B.; Harkin, D. P.; Johnston, P. G. 5-Fluorouracil: Mechanisms of Action and Clinical Strategies. *Nat. Rev. Cancer* **2003**, *3*, 330–338.

Los, F. C. O.; Randis, T. M.; Aroian, R. V.; Ratner, A. J. Role of Pore-Forming Toxins in Bacterial Infectious Diseases. *Microbiol. Mol. Biol. Rev.* **2013,** *77,* 173–207.

Love, C.; Tomas, M. B.; Tronco, G. G.; Palestro, C. J. FDG PET of Infection and Inflammation. *RadioGraphics* **2005**, *25*, 1357–1368.

Madura, J. D.; Lombardini, J. B.; Briggs, J. M.; Minor, D. L.; Wierzbicki, A. Physical and Structural Properties of Taurine and Taurine Analogues. *Amino Acids* **1997**, *13*, 131–139.

Mai, T. D.; d'Orlyé, F.; Ménager, C.; Varenne, A.; Siaugue, J.-M. Red blood cells decorated with functionalized core–shell magnetic nanoparticles: elucidation of the adsorption mechanism. *Chem. Commun.* **2013,** *49,* 5393–5395.

Matikonda, S. S.; Fairhall, J. M.; Fiedler, F.; Sanhajariya, S.; Tucker, R. A. J.; Hook, S.; Garden, A. L.; Gamble, A. B. Mechanistic Evaluation of Bioorthogonal Decaging with Trans-Cyclooctene: The Effect of Fluorine Substituents on Aryl Azide Reactivity and Decaging from the 1,2,3-Triazoline. *Bioconjug. Chem.* **2018**, *29,* 324-334.

McCloy, R. A.; Rogers, S.; Caldon, C. E.; Lorca, T.; Castro, A.; Burgess, A. Partial Inhibition of Cdk1 in G2 Phase Overrides the SAC and Decouples Mitotic Events. *Cell Cycle* **2014**, *13*, 1400–1412.

McKay, C. S.; Finn, M. G. Click Chemistry in Complex Mixtures: Bioorthogonal Bioconjugation. *Chem. Biol.* **2014**, *21*, 1075–1101.

Miyawaki, A.; Sawano, A.; Kogure, T. Lighting up Cells : Labelling Proteins with Fluorophores. **2003**, *5,* 1–7.

Mizuhara, T.; Saha, K.; Moyano, D. F.; Kim, C. S.; Yan, B.; Kim, Y.-K.; Rotello, V. M. Acylsulfonamide-Functionalized Zwitterionic Gold Nanoparticles for Enhanced Cellular Uptake at Tumor PH. *Angew. Chemie Int. Ed.* **2015**, *54*, 6567–6570.

Mura, S.; Nicolas, J.; Couvreur, P. Stimuli-Responsive Nanocarriers for Drug Delivery. *Nat. Mater.* **2013**, *12*, 991–1003.

Murdoch, C.; Giannoudis, A.; Lewis, C. E. Mechanisms Regulating the Recruitment of Macrophages into Hypoxic Areas of Tumors and Other Ischemic Tissues. *Blood* **2004**, *104*, 2224 LP – 2234.

Muzykantov, V. R. Drug Delivery by Red Blood Cells: Vascular Carriers Designed by Mother Nature. *Expert Opin. Drug Deliv.* **2010**, *7*, 403–427.

Jiang, Y.; Huo, S.; Mizuhara, T.; Das, R.; Lee, Y.; Hou, S.; Moyano, D. F.; Duncan, B.; Liang, X.; *et al.* The Interplay of Size and Surface Functionality on the Cellular Uptake. **2015**, *9,* 9986–9993.

Navya, P. N.; Kaphle, A.; Srinivas, S. P.; Bhargava, S. K.; Rotello, V. M.; Daima, H. K. Current Trends and Challenges in Cancer Management and Therapy Using Designer Nanomaterials. *Nano Converg.* **2019**, *6*, 23-30.

Neu, T. R.; Swerhone, G. D. W.; Lawrence, J. R. Assessment of Lectin-Binding Analysis for in Situ Detection of Glycoconjugates in Biofilm Systems. *Microbiology* **2001**, *147*, 299–313.

Ngo, J. T.; Adams, S. R.; Deerinck, T. J.; Boassa, D.; Palida, S. F.; Bertozzi, C. R.; Ellisman, M. H. HHS Public Access. **2016**, *12*, 459–465.

Nickel, J. C.; Ruseska, I.; Wright, J. B.; Costerton, J. W. Tobramycin Resistance of Pseudomonas Aeruginosa Cells Growing as a Biofilm on Urinary Catheter Material. *Antimicrob. Agents Chemother.* **1985**, *27*, 619 LP – 624.

Ning, X.; Lee, S.; Wang, Z.; Kim, D.; Stubblefield, B.; Gilbert, E.; Murthy, N. Maltodextrin-Based Imaging Probes Detect Bacteria in Vivo with High Sensitivity and Specificity. *Nat. Mater.* **2011**, *10*, 602–607.

Hanley, P.; Lalonde, G.; Ji, G. Alpha-Hemolysin Contributes to the Pathogenicity of Piliated Digalactoside-Binding Escherichia Coli in the Kidney: Efficacy of an Alpha-Hemolysin Vaccine in Preventing Renal Injury in the BALB/c Mouse Model of Pyelonephritis. *Infect. Immun.* **1991,** *59,* 1153–1161.

O'Hanley, P.; Lalonde, G.; Ji, G. Alpha-hemolysin contributes to the pathogenicity of piliated digalactoside-binding Escherichia coli in the kidney: efficacy of an alpha-hemolysin vaccine in preventing renal injury in the BALB/c mouse model of pyelonephritis. *Infect. Immun.* **1991,** *59,* 1153–1161.

Okamoto, Y.; Kojima, R.; Schwizer, F.; Bartolami, E.; Heinisch, T.; Matile, S.; Fussenegger, M.; Ward, T. R. A Cell-Penetrating Artificial Metalloenzyme Regulates a Gene Switch in a Designer Mammalian Cell. *Nat. Commun.* **2018**, *9*, 1–7.

Oliver, A.; Canton, R.; Campo, P.; Baquero, F.; Blazquez, J.; Cantón, R.; Campo, P.; Baquero, F.; Blázquez, J. High Frequency of Hypermutable Pseudomonas Aeruginosa in Cystic Fibrosis Lung Infection. *Science* **2000**, *288*, 1251–1253.

Pan, D. C.; Myerson, J. W.; Brenner, J. S.; Patel, P. N.; Anselmo, A. C.; Mitragotri, S.; Muzykantov, V. Nanoparticle Properties Modulate Their Attachment and Effect on Carrier Red Blood Cells. *Sci. Rep.* **2018**, *8*, 1615-1621.

Patterson, D. M.; Nazarova, L. A.; Prescher, J. A. Finding the Right (Bioorthogonal) Chemistry. *ACS Chem. Biol.* **2014,** *9,* 592–605.

Peraro, M. D.; van der Goot, F. G. Pore-forming toxins: ancient, but never really out of fashion. *Nat. Rev. Microbiol.* **2015,** *14,* 77-86.

Peulen, T.-O.; Wilkinson, K. J. Diffusion of Nanoparticles in a Biofilm. *Environ. Sci. Technol.* **2011**, *45*, 3367–3373.

Pierigè, F.; Serafini, S.; Rossi, L.; Magnani, M. Cell-Based Drug Delivery. *Adv. Drug Deliv. Rev.* **2008**, *60*, 286–295.

Pixley, F. J.; Stanley, E. R. CSF-1 Regulation of the Wandering Macrophage : Complexity in Action. **2004**, *14*, 10–12.

Pollard, J. W. Tumour-Educated Macrophages Promote Tumour Progression and Metastasis. *Nat. Rev. Cancer* **2004**, *4*, 71–78.

Pornpattananangkul, D.; Zhang, L.; Olson, S.; Aryal, S.; Obonyo, M.; Vecchio, K.; Huang, C.-M.; Zhang, L. Bacterial Toxin-Triggered Drug Release from Gold Nanoparticle-Stabilized Liposomes for the Treatment of Bacterial Infection. *J. Am. Chem. Soc.* **2011**, *133*, 4132–4139.

R. Miranda, O.; Chen, H.-T.; You, C.-C.; E. Mortenson, D.; Yang, X.-C.; H. F. Bunz, U.; M. Rotello, V. Enzyme-Amplified Array Sensing of Proteins in Solution and in Biofluids. *J. Am. Chem. Soc.* **2010**, *132*, 5285–5289.

Rakhit, R.; Navarro, R.; Wandless, T. J. Chemical Biology Strategies for Posttranslational Control of Protein Function. *Chem. Biol.* **2014**, *21*, 1238–1252.

Ramil, C. P.; Lin, Q. Bioorthogonal chemistry: strategies and recent developments. *Chem. Commun.* **2013,** *49,* 11007–11022.

Rana, S.; Bajaj, A.; Mout, R.; Rotello, V. M. Monolayer Coated Gold Nanoparticles for Delivery Applications. *Adv. Drug Deliv. Rev.* **2012**, *64*, 200–216.

Ren, Y.; Wang, R.; Gao, L.; Li, K.; Zhou, X.; Guo, H.; Liu, C.; Han, D.; Tian, J.; Ye, Q.; *et al.* Sequential Co-Delivery of MiR-21 Inhibitor Followed by Burst Release Doxorubicin Using NIR-Responsive Hollow Gold Nanoparticle to Enhance Anticancer Efficacy. *J. Control. Release* **2016**, *228*, 74–86.

Riehemann, K.; Schneider, S. W.; Luger, T. A.; Godin, B.; Ferrari, M.; Fuchs, H. Nanomedicine—Challenge and Perspectives. *Angew. Chemie Int. Ed.* **2009**, *48*, 872–897.

Saha, K.; Agasti, S. S.; Kim, C.; Li, X.; Rotello, V. M. Gold Nanoparticles in Chemical and Biological Sensing. *Chem. Rev.* **2012**, *112*, 2739–2779.

Saha, K.; Moyano, D. F.; Rotello, V. M. Protein Coronas Suppress the Hemolytic Activity of Hydrophilic and Hydrophobic Nanoparticles. *Mater. Horiz.* **2014**, *1*, 102–105.

Saha, K.; Rahimi, M.; Yazdani, M.; Kim, S. T.; Moyano, D. F.; Hou, S.; Das, R.; Mout, R.; Rezaee, F.; Mahmoudi, M.; *et al.* Regulation of Macrophage Recognition through the Interplay of Nanoparticle Surface Functionality and Protein Corona. *ACS Nano* **2016**, *10*, 4421–4430.

Sasikala, S. P.; Henry, L.; Yesilbag Tonga, G.; Huang, K.; Das, R.; Giroire, B.; Marre, S.; Rotello, V. M.; Penicaud, A.; Poulin, P.; *et al.* High Yield Synthesis of Aspect Ratio Controlled Graphenic Materials from Anthracite Coal in Supercritical Fluids. *ACS Nano* **2016**, *10*, 5293–5303.

Sasmal, P. K.; Streu, C. N.; Meggers, E. Metal Complex Catalysis in Living Biological Systems. *Chem. Commun.* **2013**, *49*, 1581–1587.

Sasmal, P. K.; Carregal-Romero, S.; Han, A. A.; Streu, C. N.; Lin, Z.; Namikawa, K.; Elliott, S. L.; Köster, R. W.; Parak, W. J.; Meggers, E. Catalytic Azide Reduction in Biological Environments. *ChemBioChem* **2012**, *13*, 1116–1120.

Sasser, T. A.; Avermaete, A. E. Van; White, A.; Chapman, S.; Johnson, J. R.; Avermaete, T. Van; Leevy, S. T. G. and W. M. Bacterial Infection Probes and Imaging Strategies in Clinical Nuclear Medicine and Preclinical Molecular Imaging. *Current Topics in Medicinal Chemistry*, 2013, *13*, 479–487.

Sauer, K.; Camper, A. K.; Ehrlich, G. D.; Costerton, J. W.; Davies, D. G. <Em>Pseudomonas Aeruginosa</Em> Displays Multiple Phenotypes during Development as a Biofilm. *J. Bacteriol.* **2002**, *184*, 1140 LP – 1154.

Skals, M.; Jensen, U. B.; Ousingsawat, J.; Kunzelmann, K.; Leipziger, J.; Praetorius, H. A. Escherichia Coli α-Hemolysin Triggers Shrinkage of Erythrocytes via KCa3.1 and TMEM16A Channels with Subsequent Phosphatidylserine Exposure. *J. Biol. Chem.* **2010**, *285*, 15557–15565.

Sletten, E. M.; Bertozzi, C. R. From Mechanism to Mouse: A Tale of Two Bioorthogonal Reactions. *Acc. Chem. Res.* **2011**, *44*, 666–676.

Sletten, E. M.; Bertozzi, C. R. Bioorthogonal Chemistry: Fishing for Selectivity in a Sea of Functionality. *Angew. Chemie - Int. Ed.* **2009**, *48*, 6974–6998.

Song, L.; Hobaugh, M. R.; Shustak, C.; Cheley, S.; Bayley, H.; Gouaux, J. E. Structure of Staphylococcal α-Hemolysin, a Heptameric Transmembrane Pore. *Science.* **1996**, *274*, 1859 LP – 1865.

Springer, C. J.; Niculescu-Duvaz, I.; Marais, R.; Spooner, R.; Light, Y.; Martin, J.; Springer, C.; Bridgewater, J.; Huber, B.; Richards, C.; *et al.* Prodrug-Activating Systems in Suicide Gene Therapy. *J. Clin. Invest.* **2000**, *105*, 1161–1167.

Stewart, P. S.; William Costerton, J. Antibiotic Resistance of Bacteria in Biofilms. *Lancet* **2001**, *358*, 135–138.

Streu, C.; Meggers, E. Ruthenium-Induced Allylcarbamate Cleavage in Living Cells. *Angew. Chemie - Int. Ed.* **2006**, *45*, 5645–5648.

T. Weiss, J.; C. Dawson, J.; Fraser, C.; Rybski, W.; Torres-Sánchez, C.; Bradley, M.; Elizabeth Patton, E.; O. Carragher, N.; Unciti-Broceta, A. Development and Bioorthogonal Activation of Palladium-Labile Prodrugs of Gemcitabine. *J. Med. Chem.* **2014**, *57*, 5395–5404.

Tacar, O.; Sriamornsak, P.; Dass, C. R. Doxorubicin: An Update on Anticancer Molecular Action. *J. Pharm. Pharmacol*. **2013**, *65,* 157–170.

Thirumurugan, P.; Matosiuk, D.; Jozwiak, K. Click Chemistry for Drug Development and Diverse Chemical–Biology Applications. *Chem. Rev.* **2013**, *113*, 4905–4979.

Tonga, G. Y.; Jeong, Y.; Duncan, B.; Mizuhara, T.; Mout, R.; Das, R.; Kim, S. T.; Yeh, Y.-C.; Yan, B.; Hou, S.; *et al.* Supramolecular Regulation of Bioorthogonal Catalysis in Cells Using Nanoparticle-Embedded Transition Metal Catalysts. *Nat. Chem.* **2015**, *7*, 597–603.

Topete, A.; Alatorre-Meda, M.; Villar-Alvarez, E. M.; Carregal-Romero, S.; Barbosa, S.; Parak, W. J.; Taboada, P.; Mosquera, V. Polymeric-Gold Nanohybrids for Combined Imaging and Cancer Therapy. *Adv. Healthc. Mater.* **2014**, *3*, 1309–1325.

Torchilin, V. P. Recent Advances with Liposomes as Pharmaceutical Carriers. *Nat. Rev. Drug Discov.* **2005**, *4*, 145–160.

Tulkens, P. M.; Arvis, P.; Kruesmann, F. Moxifloxacin safety: an analysis of 14 years of clinical data. *Drugs R. D.* **2012,** *12,* 71–100.

van Dongen, S. F. M.; de Hoog, H.-P. M.; Peters, R. J. R. W.; Nallani, M.; Nolte, R. J. M.; van Hest, J. C. M. Biohybrid Polymer Capsules. *Chem. Rev.* **2009**, *109*, 6212–6274.

Vçlker, T.; Meggers, E. Chemical Activation in Blood Serum and Human Cell Culture : Improved Ruthenium Complex for Catalytic Uncaging of Alloc-Protected Amines. **2017**, *24,* 1083–1086.

Villa, C. H.; Pan, D. C.; Zaitsev, S.; Cines, D. B.; Siegel, D. L.; Muzykantov, V. R. Delivery of Drugs Bound to Erythrocytes: New Avenues for an Old Intravascular Carrier. *Ther. Deliv.* **2015**, *6*, 795–826.

Völker, T.; Dempwolff, F.; Graumann, P. L.; Meggers, E. Progress towards Bioorthogonal Catalysis with Organometallic Compounds. *Angew. Chem. Int. Ed. Engl.* **2014**, *53*, 10536–10540.

Völker, T.; Meggers, E. Transition-Metal-Mediated Uncaging in Living Human Cells-an Emerging Alternative to Photolabile Protecting Groups. *Curr. Opin. Chem. Biol.* **2015**, *25*, 48–54.

Wang, C.; Sun, X.; Cheng, L.; Yin, S.; Yang, G.; Li, Y.; Liu, Z. Multifunctional Theranostic Red Blood Cells For Magnetic-Field-Enhanced in Vivo Combination Therapy of Cancer. *Adv. Mater.* **2014**, *26*, 4794–4802.

Weiss, J. T.; Carragher, N. O.; Unciti-Broceta, A. Palladium-Mediated Dealkylation of N-Propargyl-Floxuridine as a Bioorthogonal Oxygen-Independent Prodrug Strategy. *Sci. Rep.* **2015**, *5*, 9329-9333.

Weiss, J. T.; Dawson, J. C.; Fraser, C.; Rybski, W.; Torres-Sánchez, C.; Bradley, M.; Patton, E. E.; Carragher, N. O.; Unciti-Broceta, A. Development and Bioorthogonal Activation of Palladium-Labile Prodrugs of Gemcitabine. *J. Med. Chem.* **2014**, *57*, 5395–5404.

Weiss, J. T.; Dawson, J. C.; Macleod, K. G.; Rybski, W.; Fraser, C.; Torres-Sánchez, C.; Patton, E. E.; Bradley, M.; Carragher, N. O.; Unciti-Broceta, A. Extracellular Palladium-Catalysed Dealkylation of 5-Fluoro-1-Propargyl-Uracil as a Bioorthogonally Activated Prodrug Approach. *Nat. Commun.* **2014**, *5*, 3277-3285.

Wilson, W. R.; Hay, M. P. Targeting Hypoxia in Cancer Therapy. *Nat. Rev. Cancer* **2011**, *11*, 393.Wilson, W. R.; Hay, M. P. Targeting Hypoxia in Cancer Therapy. **2011**.

Xu, J.; Sun, S.; Li, Q.; Yue, Y.; Li, Y.; Shao, S. A Rapid Response "Turn-On" Fluorescent Probe for Nitroreductase Detection and Its Application in Hypoxic Tumor Cell Imaging. *Analyst* **2015**, *140*, 574–581.

Xu, W.; Kong, J. S.; Yeh, Y.-T. E.; Chen, P. Single-Molecule Nanocatalysis Reveals Heterogeneous Reaction Pathways and Catalytic Dynamics. *Nat Mater* **2008**, *7*, 992–996.

Yang, M.; Li, J.; Chen, P. R. Transition Metal-Mediated Bioorthogonal Protein Chemistry in Living Cells. *Chem. Soc. Rev.* **2014**, *43*, 6511–6526.

Yesilbag Tonga, G.; Mizuhara, T.; Saha, K.; Jiang, Z.; Hou, S.; Das, R.; Rotello, V. M. Binding Studies of Cucurbit[7]Uril with Gold Nanoparticles Bearing Different Surface Functionalities. *Tetrahedron Lett.* **2015**, *56*, 3653–3657.

You, C.-C.; De, M.; Rotello, V. M. Contrasting Effects of Exterior and Interior Hydrophobic Moieties in the Complexation of Amino Acid Functionalized Gold Clusters with α-Chymotrypsin. *Org. Lett.* **2005**, *7*, 5685–5688.

Yun, S.-W.; Leong, C.; Zhai, D.; Tan, Y. L.; Lim, L.; Bi, X.; Lee, J.-J.; Kim, H. J.; Kang, N.-Y.; Ng, S. H.; *et al.* Neural Stem Cell Specific Fluorescent Chemical Probe Binding to FABP7. *Proc. Natl. Acad. Sci.* **2012**, *109*, 10214 LP – 10217.

Yusop, R. M.; Unciti-broceta, A.; Johansson, E. M. V; Sa, R. M.; Bradley, M. Palladium-Mediated Intracellular Chemistry. **2011**, *3*, 239–243.

Zhang, X.; Huang, R.; Gopalakrishnan, S.; Cao-milán, R.; Rotello, V. M. Bioorthogonal Nanozymes : Progress towards Therapeutic Applications. **2019**, *1,* 90-98.

Zhang, X.-Q.; Xu, X.; Lam, R.; Giljohann, D.; Ho, D.; Mirkin, C. A. Strategy for Increasing Drug Solubility and Efficacy through Covalent Attachment to Polyvalent DNA–Nanoparticle Conjugates. *ACS Nano* **2011**, *5*, 6962–6970.